Noise and Stability of Actively Modelocked Fiber Lasers

by

Matthew Edward Grein

B.S., Electrical Engineering, Texas A&M University (1993)
S.M., Electrical Engineering and Computer Science, Massachusetts Institute of Technology (1997)

Submitted to the Department of Electrical Engineering and Computer Science
in partial fulfillment of the requirements for the degree of

Doctor of Philosophy

at the

MASSACHUSETTS INSTITUTE OF TECHNOLOGY

June 2002

Signature of Author . . . . . .
Department of Electrical Engineering and Computer Science
May 10, 2002

Certified by . . . . . .
Erich Ippen
Elihu Thompson Professor of Electrical Engineering
Professor of Physics
Thesis Supervisor

Certified by . . . . . .
Hermann Haus
Institute Professor
Thesis Supervisor

Accepted by . . . . . .
Arthur Smith
Chairperson, Department Committee on Graduate Students

Noise and Stability of Actively Modelocked Fiber Lasers

by

Matthew Edward Grein

Submitted to the Department of Electrical Engineering and Computer Science
on May 13, 2002, in partial fulfillment of the
requirements for the degree of
Doctor of Philosophy

Abstract

The timing jitter of a modelocked laser is fundamentally limited by the amplified spontaneous emission in the laser cavity. While one cannot, even in principle, remove this source of noise, one does have control over the pulse timing by using filtering and modulation. In this thesis, we report on the advances made in developing the understanding of timing jitter and stability in actively modelocked soliton fiber lasers. The main achievements reported here are: the development of a theory for quantum-limited timing jitter for the cases of amplitude and phase modulation (AM and PM, respectively); identification of a set of characteristic coefficients governing the physics of pulse retiming that depend on the laser parameters; construction of an apparatus–including the development of harmonically modelocked soliton fiber lasers in both a ring and a sigma configuration–to measure the predicted coefficients; and residual phase-noise measurements of the quantum-limited timing jitter using homodyne detection. The measurements of the characteristic coefficients and the timing jitter were found to be in good agreement with the theory. In addition, a theory for the case of harmonic modelocking was developed, and it is shown that the supermodes reveal pulse-to-pulse correlation statistics and must be included in measurements and calculations of the timing jitter. For the case of uncorrelated timing jitter between different pulses in the laser cavity, the supermodes are predicted to have the same timing jitter spectrum as the baseband mode, and this is confirmed by measurements. A scheme for reducing the timing jitter of a pulse train outside of the laser cavity using group-velocity dispersion and phase modulation is described, and it is shown theoretically that a reduction in the timing jitter is possible, but only at the expense of the carrier-frequency fluctuations. It is also shown that two-photon absorption in a semiconductor mirror structure prevented pulse dropouts in a short harmonically modelocked soliton fiber laser producing picosecond pulses at 2 GHz.

Thesis Supervisor: Erich Ippen
Title: Elihu Thompson Professor of Electrical Engineering
Professor of Physics

Thesis Supervisor: Hermann Haus
Title: Institute Professor

Acknowledgments

My deepest thanks and gratitude go to Professor Ippen for his steadfast guidance and support. It has been a joy to work under the guidance of such a talented experimentalist. He has been many things to me: a wonderful advisor; inspiring teacher; patient mentor; creative and thought-provoking scientist; and friend. I appreciate his giving me the freedom to explore my own ideas and develop as a scientist. Professor Haus has coadvised me throughout my graduate studies, and I am often filled with awe at his creativity and deep theoretical insights. His energy is contagious, and I am often inspired long after our many discussions. Having them both as my research advisors has been a privilege.

So many have helped me along the way, and I apologize for not being able to acknowledge them all. Shu Namiki was my first lab mentor, and I have always appreciated his thoroughness and patience. Moti Margalit provided many early discussions about noise and timing jitter. John Moores answered my endless questions about solitons and soliton theory. Katie Hall helped me get started on my masters project and provided advice, equipment, and a laugh when needed. Professor Franz Kärtner is a fountain of ideas and always willing to brainstorm about new directions. The many visiting scientists seem to provide new ideas and enthusiasm, including Masayuki Matsumoto, Yijiang Chen, and Uwe Morganer. I thank my course advisors Professor Terry Orlando and Professor Jin Kong. I thank Professor Jeff Shapiro and Franco Wong for their advice. I thank Tom Knight and the AI lab for letting me snoop around their labs for projects and ideas. I thank Masataka Shirasaki for his encouragement.

I have benefited greatly from the stream of talented and diverse students with whom I've had the pleasure of interacting with. Erik Thoen and I shared an office for a long time–his amicable demeanor and work ethic have always amazed me, and building lasers with him has been a blast. I've had the pleasure of sharing the lab with Leaf Jiang and working on a number of projects together–he is a talented experimentalist and always ready to lend a hand and a smile. Dan Ripin and I have been friends since his first joining the group and shared many discussions ranging from photonic crystals to ultrafast optics to politics and history. His selfless demeanor and focus have been an inspiration, and he is second-to-none in bringing the most interesting lunches! It has been a joy in getting to know and work with Juliet Gopinath over the years. She is a serious-yet-fun, hard-working, and relentless experimentalist. Working with Kazi

Abedin has been an incredible experience–I have known few persons as selfless and enthusiastic. I thank John Fini for answering my many questions about quantum optics. I thank Elizabeth Koontz for her friendship and growing spectacular samples. I thank Charles Yu and Pat Chou for their good-natured sense of humor. I thank Farhan Rana for his collaborative spirit and insights, and I thank Harry Lee for many equipment loans and discussions. I thank Professor Rajeev Ram for his enthusiasm and friendliness. I thank Bryan Robinson and Scott Hamilton for loans of copious amounts of equipment and encouragement. I thank Paul Juodawlkis for his enthusiasm, encouragement, and ideas (and for serving on my Thesis Committee), and Jeff Hargreaves for his helpful advice about RF measurements. I thank John Twichell for his support and encouragement. I thank Joe Donnelly for his help (and for serving on my Area Committee). I thank the many former members of the group for their support, including Steven Boppart, Luc Boivin, Xinde Li, Boris Gobulovic, Costis Petris, Siegfried Fleischer, David Doughtery, William Wong, Lynn Nelson, and David Jones. I thank Brett Bouma and Brent Little for their encouragement and advice. I thank the many current and graduating students, including Peter Rakich, Rohit Prasankumar, J. P. Laine, Jalal Khan, Milos Popovic, Aaron Aguirre, Felix Grawert, Paul Herz, Kristina Manatalou, Mike Watts, Tony Ko, Drew Kowalevicz, Poh-Boon Phua, Jason Sickler, Laura Tiefenbruck, and Juhi Chandalia and wish them luck. I thank Pei-lin Hsiung and Karl Schneider for their enthusiasm of the great outdoors and for recklessly trying telemark skiing with me.

I thank all of my family, including my twin brother Mark, Stephen, Anne Claire, her husband Mike, and especially my parents Leo and Frances for their support, love, and encouragement. I thank Athicha Muthitacharoen for her deep friendship and love. I thank Paul Callan for his friendship and support. I thank my coast-to-coast aunts Christine and Diane Conrad for providing a relaxing refuge. I thank Carrie, Ed and Nancy, Dave and Cindy, and David for their support.

I thank the MIT cycling club and the Boston Road (cycling) Club for their competitive spirit and providing me with a healthy outlet (aside from the occasional high-speed crash). I thank the MIT Graduate Student Council and other student groups who have worked to organize the many (but too few) social and outdoor activities and for trying to make life at MIT a bit less stressful. I thank the workers at Toscanini's for their eclectic spirit and ready

cup of much-needed coffee. I thank Mrs. Ippen and Mrs. Haus for their hospitality—they have always made me feel like family.

I thank the group secretaries Donna Gale, Cindy Kopf, and Mary Aldridge for their help. I thank EECS graduate office, including Marilyn Pierce, Monica Bell, and Peggy Carney, for their assistance. I thank the Department of Defense for the National Defense Science and Engineering Graduate Fellowship that supported me during the early years of my graduate studies, and I acknowledge funding from the Photonic Analog-to-Digital Technologies program under the Defense Advanced Research Projects Agency that supported much of the work appearing in this thesis. I thank the many teachers and professors who have encouraged me along the way.

Contents

List of Figures

List of Tables

Chapter 1

Introduction

1.1 Motivation

The development of actively modelocked lasers generating streams of picosecond and subpicosecond duration at repetition rates exceeding tens and hundreds of gigahertz has lead to many promising applications. One application is a high speed time-division multiplexed optical communications system in which a single wavelength channel is used at a very high line rate (upwards of 100 Gb/s)[6][7]. Such a system uses return-to-zero (RZ) pulses in time slots that are only 10 picoseconds wide at 100 Gb/s. The RZ source is required to produce transform-limited picosecond pulses to achieve a sufficient ratio of the time slot width and pulse width for good system margin. The RZ source must be synchronized to an external radio-frequency (RF) clock, thus necessitating active modelocking or some other means of synchronization such as regenerative modelocking with a phase-locked loop (PLL) referenced to the external RF clock[8][9][10]. The amplitude and timing jitter must be small enough such that the laser noise does not affect the system margin. For such a TDM system, the timing jitter is required to be on the order of the pulsewidt or less.

Another application example is photonic sampling. Soon after the invention of modelocking, it was proposed[11][12] that optical sampling could be used to augment electronic sampling in analog-to-digital converters (ADCs). The resolution of electronic ADCs is limited by a number of mechanisms, including thermal noise, sampling aperture jitter, and comparator ambiguity[1]. At high sampling rates, aperture error and comparator ambiguity tend to be the limiting factors.

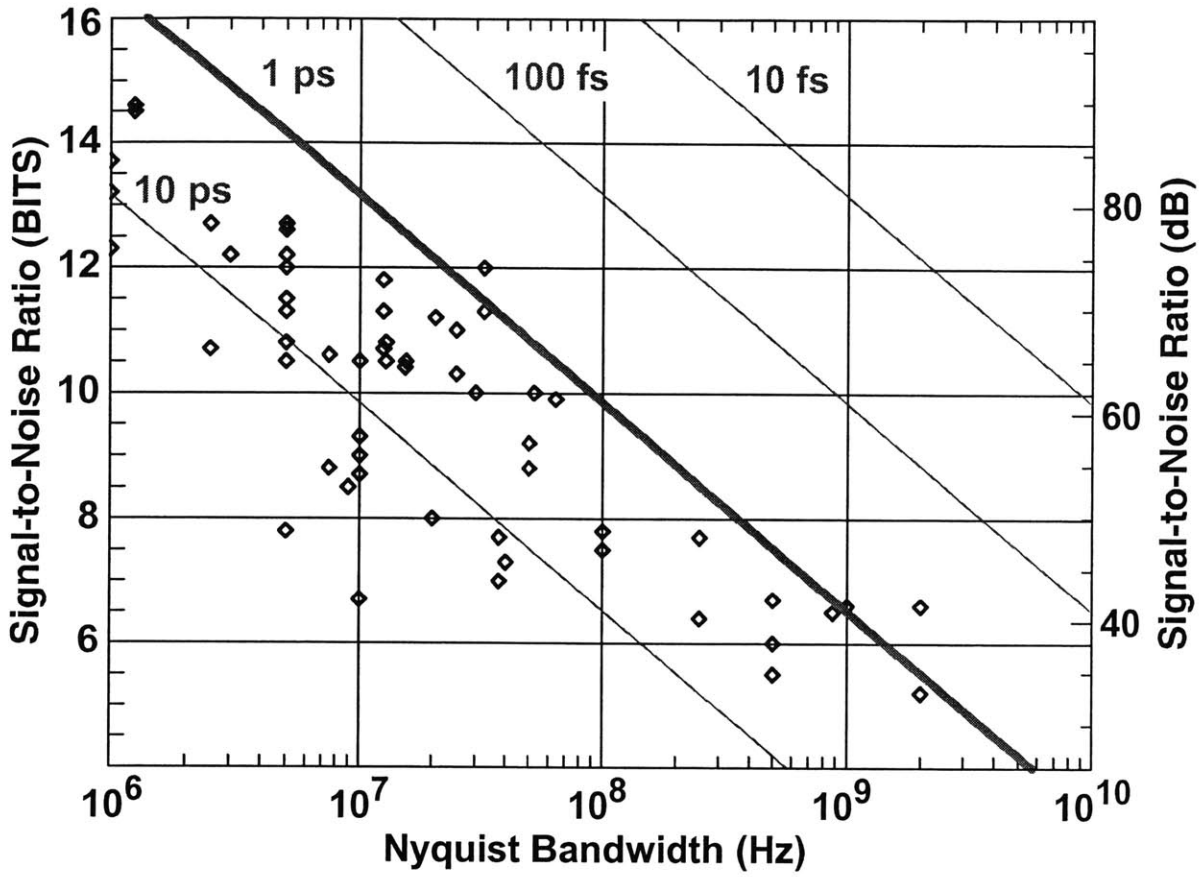

Figure 1-1: Plot of ADC performance for a variety of systems as a function of the number of resolvable bits. The diagonal lines denote limits imposed by aperature timing jitter. Figure from Ref. [1].

Figure 1-1 shows the necessary sampling jitter needed in order to achieve a given number of bits as a function of the sampling rate (Nyquist bandwidth). The 0.5-2 picosecond jitter of state-of-the-art electronic ADCs limits the number of resolvable bits at high sampling rates. In order to push high-performance ADCs beyond the apparent wall imposed by electronic sampling resolution, optical sampling can be used. A scheme[2] for an optically sampled ADC operating at 505 megasamples-per-second (MS/s) is shown in Fig. 1-2. In the front end, a modelocked laser produces a stream of modelocked pulses at a repetition rate of 505 MHz. The electronic signal to be sampled (with a maximum bandwidth of 1/2 the optical sampling rate) is input into one arm of a Mach-Zender interferometer. The interaction of the electronic signal and

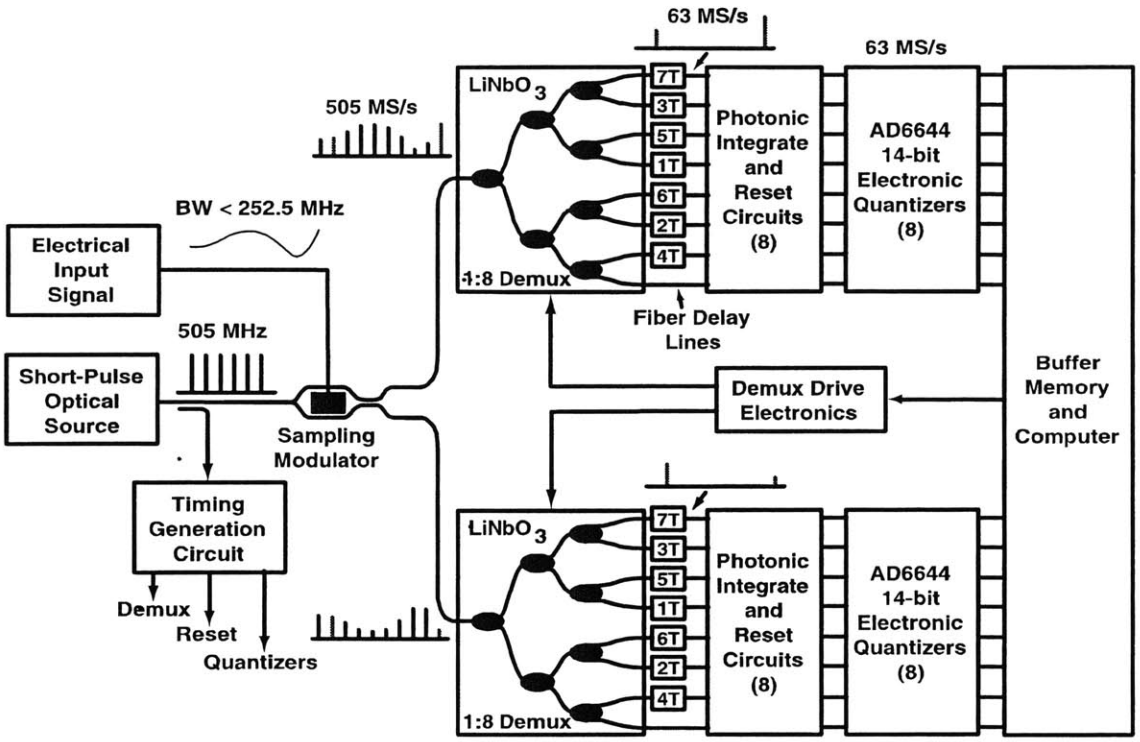

Figure 1-2: Schematic of a 505 MS/s optically sampled ADC with phase encoding and a 1:8 time interleaver. Figure from Ref. [2].

optical pulse leads to a time-dependent transmission through the interferometer, with the data now encoded onto the laser pulse amplitude. This sampling scheme was first shown in Refs. [13][14]. The encoded pulse train is passed through a time interleaver in order to time-demultiplex the data into a eight data streams the operate at one-eighth of the sampling rate of 63 MS/s–the technique of combining optical sampling and time interleaving was shown in Refs. [15][16]. Each channel can then be passed through high-performance photonic integrate-and-reset circuits and quantized electronically. By using both arms of the interferometer, it was shown that the impact of amplitude noise of the laser pulses used for optical sampling can be reduced by over 60 dB using a novel phase-encoded technique[17][18].

An estimate of the timing jitter necessary for an optically sampled ADC with time interleaving is given by[19]

$$\sigma < \frac{T}{2^N} \tag{1.1}$$

where $1/T$ is the sampling rate, N the number of resolvable bits, and σ the pulse-to-pulse timing jitter. To resolve 10 bits at 10 GS/s requires a pulse-to-pulse timing jitter that is less than 10 fs. Achieving such low pulse-to-pulse timing jitter requires a thorough understanding of the sources of laser noise and how the noise can be reduced.

1.2 Thesis Outline

The thesis is organized as follows:

Chapter 2 is an expository chapter on the master equation formalism for active modelocking with nonlinear pulse shaping. Filtering and active modulation impose stability limits on the parameters (such as pulse width and pulse energy) of the soliton-like pulses that can be maintained, and the regions of stability as a function of laser parameters (such and modulation depth, optical filter bandwidth, and group-velocity dispersion) are reviewed.

In chapter 3, a semi-classical theory of timing jitter for the case of amplitude and phase modulation (AM and PM, respectively) using soliton perturbation theory are given. In this treatment, the intracavity pulse shaping is dominated by the nonlinear soliton effects. The noise in the cavity is produced by amplified spontaneous emission (ASE) from the gain medium. The addition of modulation affects the stability of the soliton pulses and governs the retiming dynamics. We find that there is a set of characteristic time constants governing how the laser pulses respond to the ASE noise, and the constants depend on laser parameters such as modulation depth, optical filtering bandwidth, and pulse width. These time constants reflect the trapping forces that pull (or drive) the pulse to (or from) its steady-state position. Using the characteristic time constants and diffusion constants derived from the ASE noise, we derive analytical expressions for the timing jitter and compare the efficacy of AM and PM on timing jitter performance. For the case of PM, we discuss the analogy between timing jitter of a laser pulse and the position fluctuations of a classical damped harmonic oscillator and show where the analogy differs.

In chapter 4, we discuss a novel experimental setup for measuring the time constants governing timing jitter. Using the experimental setup, the retiming dynamics can be studied in real time. Over the range of accessible laser parameters for the fiber laser under test built for

these measurements, the time scale of the retiming dynamics is on the order of many tens to hundreds of round-trip times. The key accomplishment of these experiments was to show that the measured characteristic time constants agree with the theoretical predictions.

In chapter 5 we present evidence for the ASE-limited (or quantum-limited) timing jitter of an active, harmonically modelocked fiber laser. The measurement of the timing jitter is achieved using a dual-channel single-sideband phase-noise measurement apparatus. With an understanding of the characteristic time constants derived in chapter 3 (and confirmed by measurements in chapter 4), and with the analytical derivations for the timing jitter spectrum given in chapter 3, we show that measurements of timing jitter for the case of AM and PM can be completely described using the theory, both qualitatively and quantitatively. We also show how supermodes affect the timing jitter spectrum.

In chapter 6, we discuss the spectrum for harmonically modelocked lasers and present evidence confirming our theoretical picture; namely, that the supermodes of the laser cavity exhibit characteristics based on the pulse-to-pulse correlations. For the case of uncorrelated pulses (each pulse driven by ASE and independent of the other pulses), the spectra of the timing jitter for all of the supermodes are identical to that of the baseband mode. This claim is also supported by time-domain optical cross-correlation measurements. We show that all of the supermodes must be included in calculating the timing jitter over a given bandwidth.

From our study of retiming dynamics for the case of PM, we discovered that GVD and PM can be used to retime pulses inside a laser cavity. This phenomenon can also be exploited outside of a laser cavity to reduce the timing jitter, but it comes at the expense of carrier-frequency jitter. In chapter 7, we derive the conditions necessary for timing jitter reduction using GVD in a length of optical fiber and a phase modulator and show that timing jitter reduction is possible for a reasonable set of operating parameters.

One of the central challenges in building harmonically modelocked lasers is the phenomenon of pulse dropouts. Because the gain relaxation time in most rare-earth doped fibers is on the order of milliseconds, one must provide some mechanism to equalize pulse energies on a pulse-to-pulse time scale ($<$100 ps at 10 GHz). In chapter 8, we show how two photon absorption in a semiconductor mirror structure can stabilize a short, harmonically modelocked fiber laser.

Chapter 2

Review of Solitons and Active Modelocking

In this chapter, a brief review of active modelocking with solitonic nonlinear pulse shaping is given. The stability region for the soliton-like pulses for the cases of amplitude and phase modulation are given.

There exists a long history and development of modelocking using internal loss modulation– both theoretically and experimentally– since the late 1960's and early 1970's[20][21][22](also see review articles in Refs. [23][24][25][26]). The master equation describing the action of the cavity elements per roundtrip, T_R, on the amplitude of the electric-field amplitude, a, is given by

$$T_R\frac{\partial}{\partial T}a(T,t) = (g-l)a+\frac{\partial^2}{\partial t^2}(\Omega_f+jD)a-j\delta\left|a\right|^2 a+(M_{AM}+jM_{PM})(1-\cos\omega_m t)a+S(T,t) \quad (2.1)$$

where g is the small-signal gain, l the linear loss, Ω_f the optical filtering bandwidth (or gain bandwidth), D the group-velocity dispersion (GVD), δ is the self-phase modulation coefficient due to the instantaneous Kerr effect, M_{AM} and M_{PM} the depth of modulation for amplitude (AM) and phase (PM) modulation, ω_m the modulation frequency, and S a generalized noise term. The equation has been written on two time scales: one on the scale of the pulse width, t, and one on the scale of the roundtrip time, T. This also allows us to write power spectra of laser parameters (such as timing and amplitude jitter) that can evolve in time, something that

can not be done if the spectra and time variables are Fourier transform pairs. The equation has been normalized such that the pulse energy is given by

$$w = \int |a(T,t)|^2 \, dt \tag{2.2}$$

so that a has units of $\sqrt{J/s} = \sqrt{W}$. The gain is assumed to have a long relaxation time ($\sim$2 ms), and we can ignore the changes of the gain per pass. The gain only saturates on a succession of pulses. We can write

$$g = \frac{g_0}{1 + \frac{1}{P_{sat}T_R} \int |a|^2 dt} \tag{2.3}$$

where g_0 is the small signal gain and P_{sat} is the saturated power (or $P_{sat}T_R = w_{sat}$ is the saturated energy).

2.1 Active Modelocking

The case of active modelocking without intracavity nonlinear pulse shaping and for the case of zero GVD was studied by Kuizenga and Siegman[20] using a circulating Gaussian pulse analysis and by Haus[27](where it was also shown that the description of active modelocking can be manipulated in both the frequency and time domain, each bearing its own particular advantages). From the master equation from (2.1), we ignore the self-phase modulation term $\delta \left|a^2\right| a$ and set the GVD to zero. To find steady-state solutions to the master equation, we will also set the noise S equal to zero. We will first consider the case of AM. The pulse will form in the position where the loss is minimized, which is the time when the sinusoidal modulation is lowest. The sinusoidal modulation can be approximated as a parabola. We find that the resulting equation is a linear partial differential equation resembling that of a particle trapped in a parabolic potential well. The solution of eigenmodes for the cavity is the family of Hermite-Gaussians:

$$a_n(T,t) = a_n(t) \exp\left(\lambda_n \frac{T}{T_R}\right) \tag{2.4}$$

$$a_n(t) = \sqrt{\frac{w_n}{2^n \sqrt{\pi} n! \tau_a}} H_n(t/\tau_a) \exp\left(-\frac{t^2}{2\tau_a^2}\right) \tag{2.5}$$

where w_n is the pulse energy of the nth eigenmode, $H_n(t/\tau_a)$ is a Hermite polynomial of order n, τ_a is the $1/e$ pulse width of the Gaussian where

$$\tau_a = \sqrt[4]{\frac{1/\Omega_f^2}{M_{AM}\omega_m^2/2}} \tag{2.6}$$

and λ_n is the roundtrip gain of the nth eigenmode of the cavity where

$$\lambda_n = g_n - l - 2M_{AM}\tau_a^2(n + 1/2) \tag{2.7}$$

and $g_n = 1/(1 + w_n/w_{sat})$. It turns out that the $n = 0$ mode is the most stable of the eigenmodes as it requires the least amount of roundtrip gain[27], in which case

$$a_0(t) = \sqrt{\frac{w_n}{\sqrt{\pi}\tau_a}} \exp\left(-\frac{t^2}{2\tau_a^2}\right) \tag{2.8}$$

Upon every pass of the pulse through the cavity, the active modulator broadens the spectrum of the pulse (similar to injection locking) and shortens the pulse width, whereas the filter (or limited gain bandwidth) narrows the spectrum and broadens the pulse width. The resulting pulse width is a balance of these forces, as expressed in (2.6).

The pulse width is weakly dependent on the modulation depth $\left(\propto 1/\sqrt[4]{M_{AM}}\right)$ and modulation frequency $\left(\propto 1/\sqrt{\omega_m}\right)$. This is due to the fact that the pulse near the peak of the transmission is only weakly affected by the modulator curvature. It takes an increase by a factor of sixteen in modulation voltage or a factor of four in modulation frequency to halve the pulse width. Also, for case considered here where there is no nonlinear pulse shaping due to self-phase modulation and GVD, the pulse width is not dependent on the pulse energy–only the balance of spectral narrowing by the filter and spectral broadening by the modulator counts. It turns out that the case for PM is similar to that of AM, but the pulses are somewhat longer than for the case of AM and are not as robust in terms of the allowable detuning range[28].

2.2 Solitons

Since Hasegawa's prediction of the existence of solitons in optical fibers in the infrared[29], the study of optical soliton formation in optical fibers has received considerable attention–at the time of this writing, a search using the INSPEC database using the headings "optical solitons" revealed 7076 hits. In this section, only a very brief review of some of the interesting properties of solitons in modelocked lasers is given.

Using the same formalism as introduced above, we will ignore the effects of modulation, noise, and loss, leaving the following master equation

$$T_R \frac{\partial}{\partial T} a(T,t) = jD \frac{\partial^2}{\partial t^2} a - j\delta |a|^2 a \tag{2.9}$$

The solution to the equation[30][31] is given by

$$a(T,t) = a_0 \operatorname{sech}\left[\frac{t}{\tau}\right]^{(1+j\beta)} \exp\left(j\psi \frac{T}{T_R} + j\theta\right) \tag{2.10}$$

where a_0 is the amplitude of the field, β is the chirp parameter, τ the soliton pulse width, ψ the phase shift per pass, and θ the phase of the pulse. Notice that a_0^2 is the peak power of the pulse (in units of Watts). The gain, loss, and filtering come into play in the calculation of the soliton chirp, energy, and pulse width. The solution of (2.10) is self consistent only for the case where the coefficients are balanced:

$$-j\psi + g - l + \frac{(1+j\beta)^2}{\tau^2}\left(\frac{1}{\Omega_f^2} + jD\right) = 0 \tag{2.11}$$

$$\frac{1}{\tau^2}\left(\frac{1}{\Omega_f^2} + jD\right)(2 + 3j\beta - \beta^2) - j\delta a_0^2 = 0 \tag{2.12}$$

In this case, the spectral broadening induced by self-phase modulation (SPM) upchirps the pulse. This nonlinear upchirp is balanced by the linear chirp of anomalous GVD ($D < 0$). For the case for $\beta = 0$, then we find that the balance is obtained for

$$\psi = \frac{D}{\tau^2} \tag{2.13}$$

From (2.12), we find that the pulse width and pulse energy product are fixed by the parameters of the system

$$a_0^2\tau^2 = \frac{2D}{\delta} \tag{2.14}$$

This is the area theorem for solitons. We can express the area theorem in terms of average power: since the pulse energy is given by

$$w = 2a_0^2\tau \tag{2.15}$$

then the area theorem becomes

$$w\tau = \frac{4D}{\delta} \tag{2.16}$$

For fixed GVD and fixed SPM coefficient, increasing the pulse energy decreases the pulse width. However, because the nonlinear phase shift from (2.13) is limited, a short soliton pulse must generally be achieved by reduced GVD.

2.3 Actively Modelocked Solitons

Including the effects of SPM and GVD along with active modulation, the master equation does not have exact solutions. However, it has been demonstrated experimentally that soliton-like pulses can be generated from actively modelocked fiber lasers: the pulses have a hyperbolic secant shape (beyond 30 dB as revealed in autocorrelations), and the pulses obey the area theorem from (2.14). The active modelocker for a soliton system plays a major role in stabilizing the soliton and controlling the timing and amplitude jitter[32]. It turns out that the soliton effects can shorten the pulse compared that achievable with active modelocking alone, but only by a limited amount. Haus and Silberberg[33] showed that the soliton-like pulses can only be shorter than that of the actively modelocked pulse (in equation (2.6)) by up to a factor of 2.5, and it was later shown[34][35] that using excessive GVD, the limit can be extended to 4.4.

The stability of solitons in actively modelocked lasers is determined by the competition between the continuum (shed by the soliton on every round trip in response to perturbations) and the soliton itself. One can treat the continuum as a weak background pulse, $a_c(T,t)$, that does not have enough peak power to experience significant SPM. Stability requires that the

continuum experiences a net round-trip loss and is damped out. We can solve for this case by using the master equation while neglecting SPM:

$$T_R \frac{\partial}{\partial T} a_c(T,t) = (g-l)a_c + \frac{\partial^2}{\partial t^2}(\Omega_f + jD)a_c + (M_{AM} + jM_{PM})(1-\cos\omega_m t)a_c \qquad (2.17)$$

This is the same equation as that governing active modelocking,with solutions and eigenvalues given in (2.4) and (2.5). In this case, however, we require that the continuum be damped out. Since the lowest-order mode, $n = 0$, requires the least amount of round-trip gain, then all of the continuum modes will be damped if the lowest order one is damped:

$$g - l - \mathrm{Re}\sqrt{\left(\frac{1}{2}M_{AM}\omega_m^2 - j\frac{1}{2}M_{PM}\omega_m^2\right)\left(\frac{1}{2\Omega_f^2\tau^2} - jD\right)} < 0 \qquad (2.18)$$

While the round-trip gain of the continuum must be less than zero, the round-trip gain of the soliton must be greater than zero. Using soliton perturbation theory (as done in more detail in chapter 3), the expression for the round-trip gain of the soliton with pulse width τ can be written as

$$\frac{\partial}{\partial T} w_0 = 2\left(g - l - \frac{\pi^2}{24}M_{AM}\omega_m^2\tau^2 - \frac{1}{3\Omega_f^2\tau^2}\right)w \qquad (2.19)$$

Clearly, the soliton must have enough gain to overcome the linear losses l. Losses from the modulator are proportional to τ^2 and decrease rapidly as the pulses get shorter. The filtering losses are proportional to τ^{-2} and increase rapidly as the pulse gets shorter. As an example, for a 1.0 ps pulse at 10 GHz modulation with 100% modulation depth and a 10 nm filter, the losses from the filter are $\sim$ 3 times larger than losses from modulation. For a 500 fs pulse, the relative filter losses are $\sim$ 50 times larger than modulation. The criterion for stability is expressed as

$$\frac{\pi^2}{24}M_{AM}\omega_m^2\tau^2 - \frac{1}{3\Omega_f^2\tau^2} < \mathrm{Re}\sqrt{\left(\frac{1}{2}M_{AM}\omega_m^2 - j\frac{1}{2}M_{PM}\omega_m^2\right)\left(\frac{1}{2\Omega_f^2\tau^2} - jD\right)} \qquad (2.20)$$

We can see from the expression in (2.18) that the effects of amplitude and phase modulation (AM and PM, respectively) affect both parts of the stability equation. For AM, the soliton losses are greater than for the case of PM. For PM, the GVD can be used to increase the losses

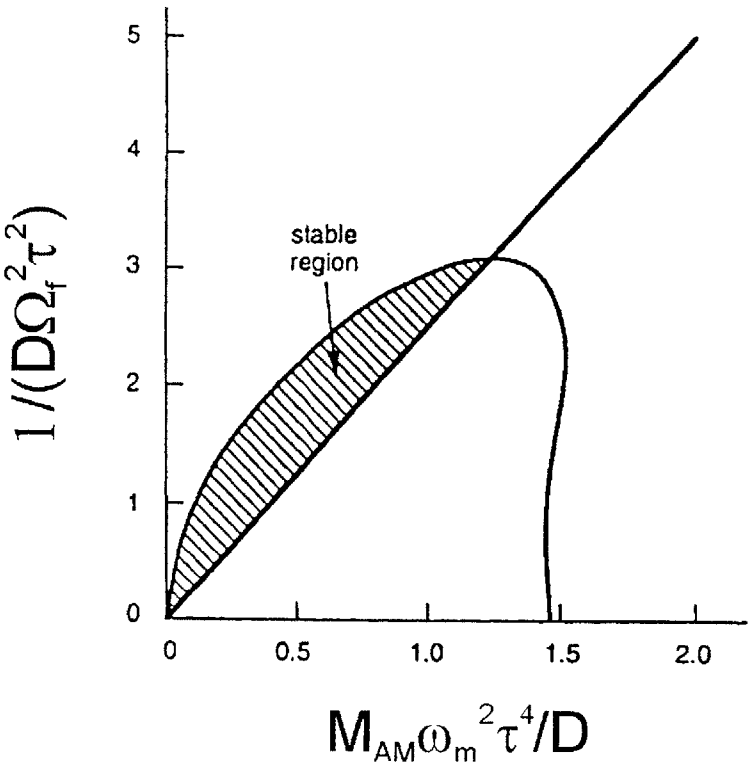

Figure 2-1: Stability plot for the case of amplitude modulation as a function of filtering strength and modulation strength (scaled by group-velocity dispersion). The region of stability is finite. Figure reproduced from Ref. [3].

of the continuum, resulting in the case that the region of stability for PM is greater than that for AM. Figs. 2-1 and 2-2 show the regions of stability as a function of filtering strength and modulation strength (scaled by D) for the case of amplitude and phase modulation, respectively. The region of stability for PM is much larger than that for AM.

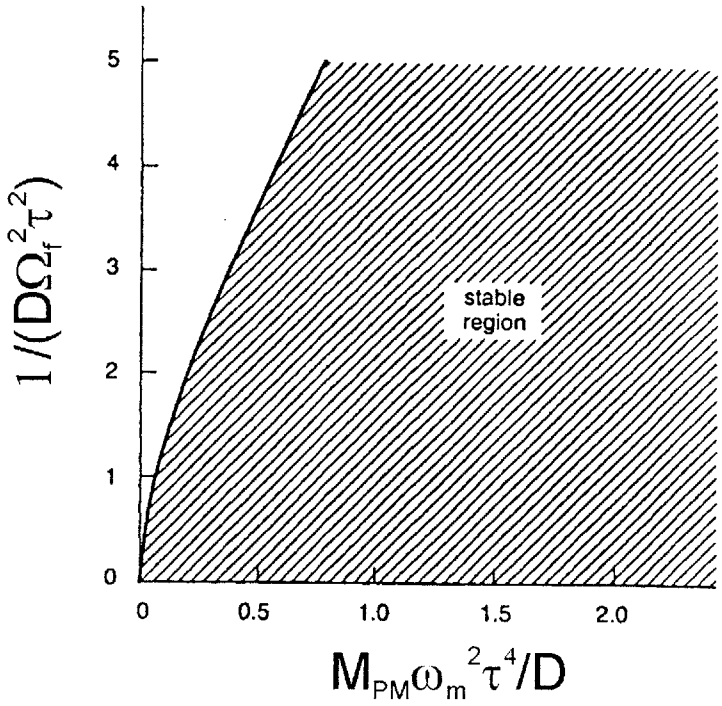

Figure 2-2: Stability plot for the case of phase modulation as a function of filtering strength and modulation strength (scaled by group-velocity dispersion). The region of stability is much larger than that for amplitude modulation. Figure reproduced from Ref. [3].

Chapter 3

Semiclassical Theory of Timing Jitter in Actively Modelocked Soliton Lasers

3.1 Introduction

[1]There have been a number of theoretical studies of timing jitter in actively modelocked lasers[38][39][40][41][42]. A comprehensive analysis of timing jitter in modelocked solid-state and fiber lasers for passive and active modelocking was given in a paper by Haus and Mecozzi[43]. In that paper, the noise was handled with soliton perturbation theory (SPT). In this chapter, we extend the analysis to actively modelocked fiber lasers and analyze the achievable timing jitter performance for the cases of amplitude and phase modulation. The SPT is useful in analyzing the noise of actively modelocked fiber lasers where solitonic effects play a role in the formation of pulses much shorter than that given by active modelocking alone[33][34][35][44][45][46]. Even in cases where the shortest pulses are not required, there is another reason why solitonic or some other kind of nonlinear effects are important in real fiber laser systems. High repetition rates (multi-GHz) call for harmonic modelocking where the repetition rate is set at a harmonic of the fundamental cavity frequency, resulting in the formation of supermodes that

[1]Many of the results from this section were obtained with helpful discussions and insights from John Moores, Moti Margalit, and Yijiang Chen. Results from this section also appear in Refs. [36][37].

individually compete for gain, resulting in amplitude fluctuations in the laser output. It has been shown that nonlinear effects, including additive-pulse limiting[47], self-phase modulation combined with filtering[48], and two-photon absorption[49] can be exploited to suppress the supermode noise.

At present, there are two basic types of modulation employed in the active modelocking of fiber lasers: amplitude (AM) and phase (PM) modulation[23]. The laser pulse characteristics using either modulator (i.e., pulse shape, pulse duration) are similar[44][46][50]. However, the characteristics of pulse retiming are qualitatively different for AM and PM[46]. For AM, mistimed pulses experience loss, leading to a timing restoration dependent on the slope of the transmission window and the square of the pulse width. For PM, mistimed pulses are initially frequency-shifted. The frequency shift is converted to a timing shift via GVD, leading to a timing restoration dependent on depth of modulation, GVD, and filtering. We should expect, then, that the resulting timing jitter for AM and PM are quite different, and we show in this paper that they are.

Previous work on passively modelocked soliton[51] and stretched-pulse[52][53] fiber lasers have shown that the timing jitter is quantum-limited in the sense that the amplified spontaneous emission (ASE) of the gain dominates the timing jitter. While other quantum effects–including fluctuations due to dissipation[54]–also contribute, they are much smaller than ASE contributions. Many experiments on actively modelocked soliton fiber lasers (AMFL)–in which the laser is modelocked using an external microwave oscillator–have demonstrated that, at present, the timing jitter is limited by the phase noise of the driving oscillator[9][55][56][57]. This is a technical limitation of the laser timing jitter which can be overcome using a lower-noise oscillator. Just as for the case of the passively modelocked laser, the fundamental limitation of the laser timing jitter is given by the ASE. In this chapter, we derive the ASE-limited timing jitter of actively modelocked soliton lasers. One could ask for the amount of timing jitter reduction possible using either squeezed light or some other scheme in which the timing jitter (or pulse position) is reduced at the expense of the pulse momentum (or carrier frequency), but that is considered in Refs. [58][59] and in chapter 7. We derive analytical expressions for the timing jitter and find that there is a set of characteristic time constants determined by the laser parameters that define the timing jitter spectrum. We show that the use of AM and PM

affect the pulse retiming is qualitatively different ways.

The rest of the chapter is organized as follows: in sections 3.2 and 3.3, we derive the spectrum of the timing jitter for AM and PM, respectively. We derive the eigenvalues that determine the pulse retiming constants and describe the characteristic differences in the restoration of pulse timing for AM and PM. We derive analytical expressions for the timing jitter as a function of characteristic time constants and diffusion constants that characterize the noise sources. In sections 3.4 and 3.5, we consider the quantum-limited jitter for AM and PM where the only noise source is the amplified spontaneous emission from the gain and consider how the jitter depends on GVD. In section 3.6, we compare the relative minimum jitter between AM and PM.

3.2 Active Modelocking with Amplitude Modulation (AM) and Filtering

Our starting point will be the master equation for modelocking describing the evolution of a pulse in an actively modelocked laser with SPM and GVD[27][33][60]:

$$T_R\frac{\partial}{\partial T}a - iD\frac{\partial^2}{\partial t^2}a - i\delta|a|^2a = \left[g - l + \frac{1}{\Omega_f^2}\frac{\partial^2}{\partial t^2} - \frac{M_{AM}}{2}\left(1-\cos(\omega_m t)\right)\right]a + T_R S(t,T) \tag{3.1}$$

The master equation is written as a function of two time scales: a short time scale, t, on the order of the pulse width, and a long time scale, T, on the order of the roundtrip time. a is the amplitude of the electric field envelope, T_R the cavity round-trip time for a cavity of length L, D the net group-velocity dispersion (GVD) where $D > 0$ is anomalous, δ the self-phase modulation (SPM) coefficient, l the linear loss, Ω_f the bandwidth of an intracavity optical filter, and M_{AM} the depth of modulation and varies from zero to one. For solid state and fiber lasers, the gain relaxation time is on the order of milliseconds, and the saturation energy is large, thus we can ignore changes in the gain on the time scale of the pulse, and the gain saturates only after a succession of pulses. The pulse energy w_0 is given by $w_0 = \int_{-T_R/2}^{T_R/2}|a(T,t)|^2 dt$. $S(t,T)$ is a generalized noise source and can be of classical and/or quantum-mechanical origin.

For simplicity, we ignore detuning effects by assuming that the frequency of an external local oscillator driving the modulator and the natural laser cavity frequency (or some harmonic of it) are synchronized. In writing (3.1) we have also ignored the fact that the lasing wavelength and the gain peak do not usually coincide. In the harmonically modelocked laser, the pulses are generally very long and have spectra much narrower than the available gain spectra, so the approximation that the gain is flat over the extent of the pulse spectrum is a reasonable one.

Complete analytical solutions to the master equation (3.1) have not been found. However, it is known that the pulses resulting from the actively modelocked soliton laser are solitary waves whose behavior is dominated by the nonlinear Schrödinger equation (NLSE), comprising the left-hand side of (3.1). Without the dissipative terms of the right-hand side, complete analytical solutions have been found[61], and they are solitons. The terms on the right hand side are perturbations to the NLSE that govern the stability of the solitons[3][32] in the presence of the dissipative terms, including the noise. We make the transition from the purely soliton solutions to the stabilized soliton-like solutions via the soliton perturbation theory (SPT). SPT is applied by asserting that the solution to the master equation, a, consists of the soliton solution to the unperturbed NLSE, a_s, plus perturbations Δa linearized about the soliton solution[34][60][62][63]:

$$a(t,T) = a_s(t,T) + \Delta a(t,T) \exp\left(-j\frac{\delta}{2}A_0^2\frac{T}{T_R}\right) \tag{3.2}$$

where the unperturbed soliton solution is

$$a_s(t,T) = A_0 \mathrm{sech}\left(\frac{t}{\tau}\right) \exp\left(-j\frac{\delta}{2}A_0^2\frac{T}{T_R}\right) \tag{3.3}$$

The soliton solution obeys the area theorem, relating the pulse energy, pulse width, and GVD:

$$w_0\tau = \frac{4D}{\delta} \tag{3.4}$$

The perturbations are expanded in the four pulse parameters: Δw, photon number; $\Delta\theta$, phase; Δp, momentum (carrier frequency); and ΔT, timing, plus a continuum, Δa_c, which is not part

of the pulse:

$$\Delta a(t,T) = f_w(t)\Delta w(T) + f_\theta(t)\Delta\theta(T) + f_p(t)\Delta p(T) + \tag{3.5}$$

$$f_T(t)\Delta T(T) + \Delta a_c(t,T) \tag{3.6}$$

where the f_i terms (for $i = w,\ \theta,\ p,\ T$) are projection functions[64] for each of the pulse parameters given by the derivatives of the steady-state solution

$$f_w(t) = \frac{\partial}{\partial w}a_s = \frac{1}{w_0}\left[1 - \frac{t}{\tau}\tanh\left(\frac{t}{\tau}\right)\right]a_s(t,T) \tag{3.7}$$

$$f_\theta(t) = \frac{\partial}{\partial\theta}a_\theta = ja_s(t,T) \tag{3.8}$$

$$f_p(t) \equiv j\frac{2}{w_0}ta_s(t,T) \tag{3.9}$$

$$f_t(t) = \frac{\partial}{\partial t}a_t = \frac{1}{\tau}\tanh\left(\frac{t}{\tau}\right)a_s(t,T) \tag{3.10}$$

Soliton perturbation theory assigns an orthogonal set of adjoint functions such that the products integrate to a Kroneker delta function, given by

$$\mathrm{Re}\int dt' f^*_{\_i}(t')f_j(t') = \delta_{ij} \tag{3.11}$$

Then our choices for the adjoint functions become

$$f_{\_w}(t) = 2a_s(t) \tag{3.12}$$

$$f_{\_\theta}(t) = 2j\frac{1}{w_0}\left[1 - \frac{t}{\tau}\tanh\left(\frac{t}{\tau}\right)\right]a_s(t) \tag{3.13}$$

$$f_{\_p}(t) = j\frac{2}{w_0\tau}\tanh\left(\frac{t}{\tau}\right)a_s(t) \tag{3.14}$$

$$f_{\_t}(t) = \frac{2}{w_0}ta_s(t) \tag{3.15}$$

and the coefficients of the perturbation expansion from equation (3.6) are given by

$$\Delta i(T) = \frac{1}{2}\int dt\left[f^*_{\_i}(t)\Delta a(t) + f_{\_i}(t)\Delta a^*(t)\right] \tag{3.16}$$

where $i = [w, \theta, p, T]$. Substituting (3.6) into the master equation in (3.1), the equations of motion for the four pulse parameters are given as[3][60][64]

$$T_R \frac{\partial}{\partial T} \Delta w = -2 g_{sat} \Delta w + T_R S_n(T) \tag{3.17}$$

$$T_R \frac{\partial}{\partial T} \Delta \theta = -\delta \frac{A_0^2}{w_0} \Delta w + T_R S_\theta(T) \tag{3.18}$$

$$T_R \frac{\partial}{\partial T} \Delta p = -\frac{4}{3\Omega_f^2 \tau^2} \Delta p + T_R S_p(T) \tag{3.19}$$

$$T_R \frac{\partial}{\partial T} \Delta T = -2D\Delta p - \frac{\pi^2}{3} \frac{M_{AM}}{2} \omega_m^2 \tau^2 \Delta T + T_R S_T(T) \tag{3.20}$$

where the saturated gain, g_{sat}, is given by

$$g_{sat} \equiv \frac{g_0}{1 + w_0/w_{sat}} \frac{w_0}{w_{sat}} \tag{3.21}$$

and determined by the losses per round trip, given by

$$g_{sat} = \frac{\pi^2}{6} M_{AM} \omega_m^2 \tau^2 + \frac{4}{3\Omega_f^2 \tau^2} \tag{3.22}$$

The first term is due to the losses by the modulator, showing that the losses increase with the square of the pulse width. The second term is due to the losses by the filter and inversely proportional to the square of the pulse width. The S_i terms (for $i = w, p, \theta, T$) are the projections of the noise S onto each of the pulse parameters. We will explicitly consider the quantum noise starting in later sections, but for now its specification is unnecessary.

The terms governing the equations of motion have simple interpretations:

- Amplitude fluctuations are damped out by gain saturation. The relevant time scale for saturation of the gain in solid-state and fiber lasers is on the order of milliseconds. Amplitude changes are reflected in pulse width–and thus spectral–changes, and filtering helps to damp them out on the laser roundtrip time scale, typically tens to hundreds of nanoseconds.

- Optical phase fluctuations are driven by amplitude fluctuations through Kerr SPM. Changes

in phase are not, however, coupled to the other pulse parameters, as changes in amplitude, timing, and carrier frequency are not sensitive to the optical phase.

- Filtering damps carrier frequency fluctuations.
- Frequency fluctuations perturb the laser timing. GVD converts frequency fluctuations into timing changes.
- Timing fluctuations are damped out by the restoring action of the amplitude modulator.

In general, changes in the pulse energy can lead to changes in the pulse timing through the Kramers-Kronig relation associating changes in the gain with changes in the index of refraction. However, this effect is very small in a fiber laser and ignored here.

The equations of motion are easily solved in the frequency domain. We define the Fourier transform as:

$$f(\Omega) = \frac{1}{\sqrt{T_0}} \int f(T)\, e^{-j\Omega T}\, d\Omega\,, \tag{3.23}$$

$$f(T) = \frac{\sqrt{T_0}}{2\pi} \int f(\Omega)\, e^{j\Omega T}\, dT \tag{3.24}$$

with a normalization time T_0 that has been introduced to avoid the divergence of the frequency spectra. This also conveniently puts the units of $f(\Omega)$ in terms of $f(T)/\sqrt{Hz}$. The spectra for the mean-square pulse parameters are given as

$$\left\langle |\Delta w(\Omega)|^2 \right\rangle_{AM} = \frac{\left\langle |S_w(\Omega)|^2 \right\rangle}{\frac{1}{\tau_w^2} + \Omega^2} \tag{3.25}$$

$$\left\langle |\Delta \theta(\Omega)|^2 \right\rangle_{AM} = \frac{\left\langle |S_\theta(\Omega)|^2 \right\rangle}{\frac{1}{\tau_\theta^2} + \Omega^2} \tag{3.26}$$

$$\left\langle |\Delta p(\Omega)|^2 \right\rangle_{AM} = \frac{\left\langle |S_p(\Omega)|^2 \right\rangle}{\frac{1}{\tau_p^2} + \Omega^2} \tag{3.27}$$

$$\left\langle |\Delta T(\Omega)|^2 \right\rangle_{AM} = \frac{1}{\frac{1}{\tau_{AM}^2} + \Omega^2} \left\{ \left(2|D| \frac{1}{T_R} \right)^2 \frac{\left\langle |S_p(\Omega)|^2 \right\rangle}{\left(\frac{1}{\tau_p^2} + \Omega^2 \right)} + \left\langle |S_T(\Omega)|^2 \right\rangle \right\} \tag{3.28}$$

where time constants have been defined as

$$\frac{1}{\tau_w} \equiv 2\left(\frac{1}{3\Omega_f^2\tau^2} + \frac{M_{AM}\pi^2}{12}\omega_m^2\tau^2\right)\frac{1}{T_R} \tag{3.29}$$

$$\frac{1}{\tau_\theta} \equiv \delta\frac{A_0^2}{w_0} \tag{3.30}$$

$$\frac{1}{\tau_p} \equiv \frac{4}{3\Omega_f^2\tau^2}\frac{1}{T_R} \tag{3.31}$$

$$\frac{1}{\tau_{AM}} \equiv \frac{\pi^2}{3}\frac{M_{AM}}{2}\omega_m^2\tau^2\frac{1}{T_R} \tag{3.32}$$

In writing (3.28), we have ignored the cross correlation terms between the noise projections. For completeness, they are given in the appendix. The units of $\left\langle|\Delta T|^2\right\rangle$ are in s^2/Hz.

Our interest here is to quantify the mean square fluctuations, assuming white noise spectra for the frequency and timing noise sources. The first two terms of equation (3.28) contribute components that have spectra of the form

$$\frac{1}{\left(\frac{1}{\tau_{AM}^2}+\Omega^2\right)\left(\frac{1}{\tau_{w,p}^2}+\Omega^2\right)} \tag{3.33}$$

while the last term contributes as

$$\frac{1}{\left(\frac{1}{\tau_{AM}^2}+\Omega^2\right)} \tag{3.34}$$

where the τ_{AM} term is attributed to—and inversely proportional to–the modulator strength. The presence of the retiming term τ_{AM} prevents the timing jitter spectrum from diverging at low frequencies. This is in contrast with the timing jitter spectrum of a passively modelocked laser that is proportional to $1/\Omega^2$ at low frequencies and indicative of the fact that without a retiming element (such as a modulator), the pulse timing undergoes a random walk[43]. Noise projected out onto the carrier frequency change, $S_p(\Omega)$, fall off at 40 dB/decade due to the two-terms in the denominator, while the noise projected out directly onto the pulse timing, $S_T(\Omega)$, falls off at 20 dB/decade. The effect of AM on the jitter is governed by the decay rate, τ_{AM}. From (3.32), the decay rate is proportional to the curvature of the modulation times the pulse width squared.

In the limit of weak soliton shaping, the pulse width dependence on modulation strength

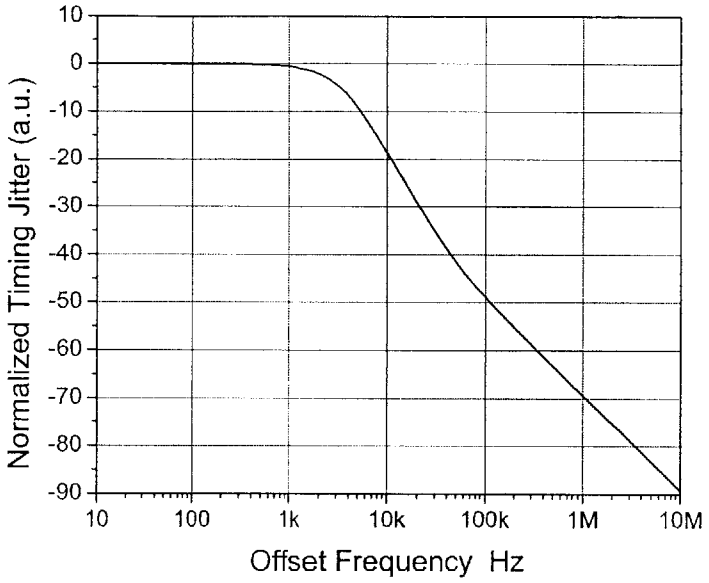

Figure 3-1: Spectrum of the timing jitter for the case of amplitude modulation driven by white noise that perturbs both the position and carrier frequency of the pulse.

is given by the Siegman-Kuizenga formula[20]: $\tau \propto \sqrt[-4]{M_{AM}\omega_m^2}$, thus $(1/\tau_{AM}) \propto \sqrt{M_{AM}\omega_m^2}$, suggesting that the damping rate is independent of pulse width. In the limit of strong soliton shaping[33][34], the pulse shaping mechanisms are much less dependent on the modulation depth as given by Siegman-Kuizenga–at least the dependence will be even weaker than the inverse-fourth root dependency (see Fig. 4-11). In that limit, the decay rate *decreases*–that is, τ_{AM} gets bigger–as the pulses get shorter due to soliton effects. In both cases, however, the decay rate is enhanced by using as large a modulation depth as possible.

Fig. $3-1$ shows the jitter spectrum for some typical parameters with white noise sources given in equations (3.39) and (3.58) – (3.61). The spectrum is flat until the first turning point where $f = 1/(2\pi\tau_{AM})$, after which the spectrum falls off at 20 dB/dec. For $f \geq 1/(2\pi\tau_p)$, the

spectrum falls off at 40 dB/dec until the frequency $f = f_{pull}$ given by

$$f_{pull} = \frac{1}{2\pi}\sqrt{\frac{1}{\tau_p^2} + \left(\frac{2D}{T_R}\right)^2 \frac{\langle|S_p(\Omega)|\rangle}{\langle|S_T(\Omega)|\rangle}} \tag{3.35}$$

$$= \frac{1}{2\pi}\sqrt{\frac{1}{\tau_p^2} + \left(\frac{2D}{T_R}\right)^2 \frac{D_p}{D_T}} \tag{3.36}$$

Eqution (3.35) shows that f_{pull} will always equal to or larger than $1/(2\pi\tau_p)$, thus the timing jitter spectrum will always first drop off by 40 dB/dec before being pulled up to 20 dB/dec.

The mean-squared timing jitter is given by the integrated spectrum of the timing fluctuations, expressed as

$$\sigma^2[f_{low}, f_{high}] = \int_{f_{low}}^{f_{high}} \frac{2}{\pi} \left\langle |\Delta T(\Omega)|^2 \right\rangle \, d\Omega \tag{3.37}$$

where f_{low} and f_{high} bound the frequency range of interest, and the units of σ are in seconds. To add up the contributions for all frequencies, one sets f_{low} and f_{high} to 0 and $+\infty$, respectively. In many cases, one is only interested in timing jitter fluctuations that occur at rates faster than kilohertz. Then one can ignore the contributions from amplitude fluctuations, since they are negligible due to the long upper-state lifetime of the gain in fiber lasers (on the order of a few milliseconds). Carrying out the integral in (3.37), the timing jitter for AM becomes

$$\sigma^2_{AM}[0, +\infty] \equiv \sigma^2_{AM} = \left(2\,|D|\,\frac{1}{T_R}\right)^2 \frac{\tau^2_{AM}\tau^2_p}{\tau_p + \tau_{AM}} D_{pp} + \tau_{AM} D_{TT} \tag{3.38}$$

where we have assumed that the noise sources are white and described by diffusion constants D_{ij} from the correlation

$$\left\langle S_i(T,t) S_j^*(T',t') \right\rangle = D_{ij}\delta_{i,j}\delta(T-T')\delta(t-t') \tag{3.39}$$

Our assumption of white noise sources simplifies the analytical treatment, but it should be noted that while the quantum noise sources are white, the classical sources in general are not[43]. Our use of diffusion coefficients for the case of classical noise, then, can be considered to be valid within the bandwidth of the actual noise source. Also, since the pulses from the

actively modelocked laser are rather long, the corresponding spectrum is narrow. A filter is used to stabilize the pulses in the harmonically modelocked laser, thus only a portion of the gain bandwidth is accessible. The noise is generally white within the spectrum of the pulse. In a later section, we will consider the quantum-limited diffusion constants given by amplified spontaneous emission.

We now consider the case where the damping due to filtering is stronger than that of the modulator such that $\tau_p << \tau_{AM}$. Then (3.38) reduces to

$$\sigma_{AM}^2 = \left(2\left|D\right|\frac{1}{T_R}\right)^2 \tau_{AM}\tau_p^2 D_{pp} + \tau_{AM} D_{TT} \tag{3.40}$$

We can make a few observations from equation (3.40). The timing jitter due to noise that drives carrier frequency fluctuations, D_{pp}, is reduced by strong filtering and small dispersion. Of course, a soliton laser can not operate with zero net GVD, for such a pulse would necessarily have zero energy. However, one can extend the idea to the case of dispersion-managed solitons (DMS) in which the average dispersion is near zero, but the local dispersion is allowed to swing between normal and anomalous. This stretching allows for an enhancement of the pulse energy compared to that of the soliton, even where the average GVD is zero[65]. From (3.32), τ_{AM} is inversely proportional to the product of modulation depth, the square of the driving frequency, and the square of the pulse width. Thus, one should employ as large a modulation depth as possible. Using longer pulses will also minimize fluctuations from both D_{pp} and D_{TT} insofar as the noise terms do not depend on pulse width (for the case of ASE-limited noise, however, D_{pp} and D_{TT} do depend on pulse width and discused in section 3.4). The $M_{AM}\omega_m^2$ term gives the curvature of the modulation "well"–here, it is determined by the frequency of the modulation cycle so that higher modulation frequencies yield narrower wells, thus steeper slopes. Ideally, one would use strongly-curved wells that yield a strong restoring force, but not so steep as to introduce excessive losses to the pulses. In practice, high bit-rate modulators have electrical bandwidths on the order of 100 GHz for $LiNbO_3$ and polymer waveguides and similar bandwidths for electro-absorption modulators, thus limiting the steepness of the modulator well.

3.3 Active Modelocking with Phase Modulation (PM) and Filtering

For modelocking with a phase modulator, we replace the M_{AM} term with jM_{PM} in the master equation given in (3.1). The equations of motion are then given by

$$T_R \frac{\partial}{\partial T}\Delta w = -2g_{sat}\Delta w + T_R S_w(T) \tag{3.41}$$

$$T_R \frac{\partial}{\partial T}\Delta \theta = -\delta \frac{A_0^2}{w_0}\Delta w + T_R S_\theta(T) \tag{3.42}$$

$$T_R \frac{\partial}{\partial T}\Delta p = -\frac{4}{3\Omega_f^2 \tau^2}\Delta p + M_{PM}\omega_m^2 \Delta T + T_R S_p(T) \tag{3.43}$$

$$T_R \frac{\partial}{\partial T}\Delta T = -2D\Delta p + T_R S_T(T) \tag{3.44}$$

and the round-trip gain needed to compensate for the loss is given by

$$2g_{sat} = \frac{1}{3\Omega_f^2 \tau^2} \tag{3.45}$$

In comparison with the equations of motion for AM, we can distinguish the key differences for PM:

- Timing fluctuations are not directly damped out. Mistimed pulses are first frequency shifted by the phase modulator. The frequency shifts are then converted to timing shifts via GVD, and the timing restoration will depend on the product of the frequency shift exerted by the modulator and GVD.
- While M_{AM} is limited to 1.0, M_{PM} can be much larger ($\gg \pi$)

Just as the case for AM, we can write the spectra for the perturbed pulse parameters driven by the noise sources. We show only the spectrum of the timing fluctuations here, again ignoring

the cross-correlation terms:

$$\left\langle |\Delta T(\Omega)|^2 \right\rangle_{PM} = \frac{\left(\frac{1}{\tau_p^2} + \Omega^2\right)}{\left[\Omega^4 + \left(\frac{1}{\tau_p^2} - 2\Omega_{PM}^2\right)\Omega^2 + \Omega_{PM}^4\right]} * \left\{ \left(2|D|\frac{1}{T_R}\right)^2 \frac{\left\langle |S_p(\Omega)|^2 \right\rangle}{\left(\frac{1}{\tau_p^2} + \Omega^2\right)} + \left\langle |S_T(\Omega)|^2 \right\rangle \right\} \tag{3.46}$$

where

$$\begin{aligned} \Omega_{PM} &\equiv \sqrt{2|D|M_{PM}\omega_m^2}\frac{1}{T_R} \\ \frac{1}{\tau_p} &= \frac{4}{3\Omega_f^2\tau^2}\frac{1}{T_R} \end{aligned} \tag{3.47}$$

Comparing the spectrum of the rms timing jitter for PM to that of the AM case, we see that the effect of the phase modulator is to add terms in both the numerator and denominator to the leading term of (3.46). This point can be seen more clearly by analyzing the features of $\langle \Delta T(\Omega) \rangle_{PM}$ rather than the mean-square value $\left\langle |\Delta T(\Omega)|^2 \right\rangle_{PM}$ and solving for the poles and zeros:

$$\langle \Delta T(\Omega) \rangle_{PM} = \frac{-j\Omega + \frac{1}{\tau_p} \quad \cdot \quad \cdot}{(-j\Omega + r_1)(-j\Omega + r_2)} \left\{ -\left(2|D|\frac{1}{T_R}\right) \frac{\langle S_p(\Omega) \rangle}{\left(-j\Omega + \frac{1}{\tau_p}\right)} + \langle S_T(\Omega) \rangle \right\} \tag{3.48}$$

The first term of (3.48) has the form

$$\frac{1}{(-j\Omega + r_1)(-j\Omega + r_2)} \tag{3.49}$$

where the poles r_1 and r_2 are given by

$$r_{1,2} = -\frac{1}{2\tau_p}\left[1 \pm \sqrt{1 - 4\left(\tau_p\Omega_{PM}\right)^2}\right] \tag{3.50}$$

These poles can, in general, be complex, depending on the relative values of filtering, τ_p, and effective phase modulation, Ω_{PM}. This is a natural consequence of the retiming action of phase modulation. The form of the spectrum from equation (3.49) is that of a driven, damped

harmonic oscillator, with damping $1/\tau_p$ and restoring force Ω_{PM}. From (3.31), the damping is provided by filtering. From (3.47) the restoring force is provided by the frequency shift due to the product of phase modulation and GVD. The character of the solution for the pulse retiming, $\Delta T(T)$, can be overdamped, underdamped, or critically damped, depending on the value of the determinant in equation (3.50). Where $4\left(\tau_p\Omega_{PM}\right)^2 < 1$, the damping term is stronger than the restoring force, the poles $r_{1,2}$ are real, and the pulse retiming is a decaying exponential, characteristic of overdamping. Where $4\left(\tau_p\Omega_{PM}\right)^2 > 1$, the restoring force is stronger than the damping term, the poles $r_{1,2}$ are complex, and the pulse retiming is that of an exponentially decaying sinusoid, characteristic of underdamping. For $4\left(\tau_p\Omega_{PM}\right)^2 = 1$, the damping and restoring force balance each other, the poles are degenerate, leading to a pulse retiming that is given by an exponential and the product of a linear function of t and an exponential, characteristic of critical damping. These regimes governing pulse retiming for PM have been verified and will be covered in more detail in the chapter 4.

The second term has the form

$$\frac{-j\Omega + \frac{1}{\tau_p}}{\left(-j\Omega + r_1\right)\left(-j\Omega + r_2\right)} \tag{3.51}$$

which is similar to that of the first term, but the filtering in the numerator adds a zero to the spectrum. Depending on the relative values of τ_p and Ω_{PM}, the timing jitter spectrum for PM in equation 3.46 can fall off more or less quickly than for AM. What matters in the evaluation of timing jitter is the *integral* of the spectrum in the frequency range of interest.

Figs. 3-2 is the spectrum of the jitter as expressed in equation (3.46) for the case where $4(\tau_p\Omega_{PM})^2 < 1$, corresponding to overdamping. Fig. 3-3 is the spectrum for the underdamped case, where $4(\tau_p\Omega_{PM})^2 > 1$. The peak in the spectrum is indicative of a strong oscillation in the pulse retiming from the complex poles.

The jitter is given by

$$\sigma_{PM}^2 = \left(2D\frac{1}{T_R}\right)^2 \frac{\tau_p}{\Omega_{PM}^2} D_{pp} + \tau_p \left(1 + \frac{1}{\left(\tau_p\Omega_{PM}\right)^2}\right) D_{TT} \tag{3.52}$$

where we have assumed that the noise sources S_p and S_T are white and assigned diffusion coefficients from (3.39). Before analyzing the expression for the jitter from equation (3.52),

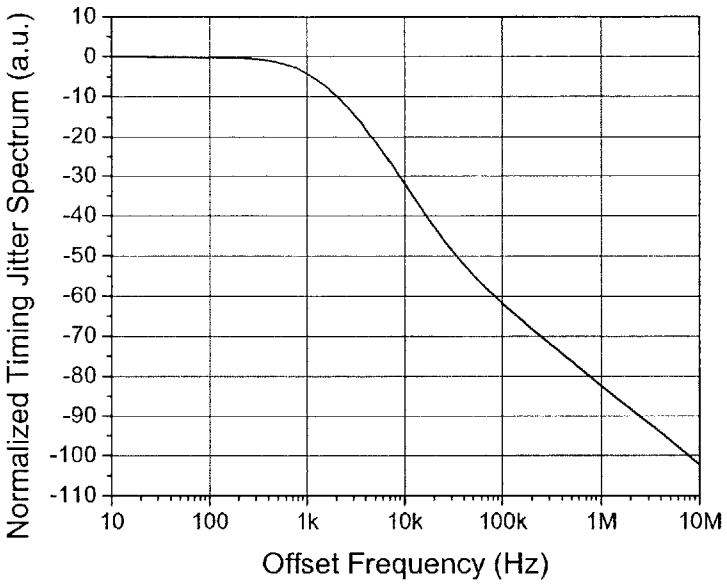

Figure 3-2: Normalized timing jitter spectrum for the case of PM for the case where $f_p = 24$ krad/s and $\Omega_{PM} = 10$ krad/s, corresponding to the case of overdamping.

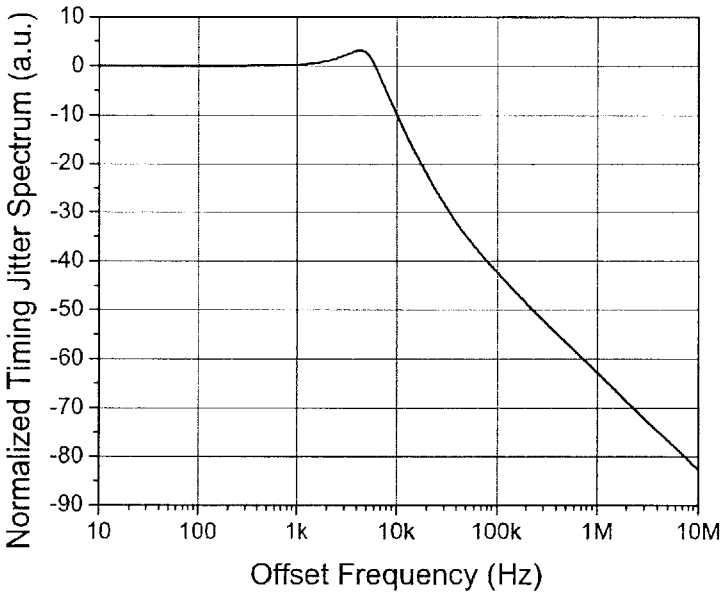

Figure 3-3: Normalized timing jitter spectrum for the case of PM for the case where $f_p = 24$ krad/s and $\Omega_{PM} = 32$ krad/s, corresponding to the case of underdamping.

we should first consider the position fluctuations of a particle (with unity mass) trapped in a 1-D parabolic potential well with restoring force $F = -\Omega_{ho}\Delta T$ and damping rate $1/\tau_{ho}$ driven by white noise, S_{ho} (where we have transformed the spatial coordinate of x into the temporal coordinate of t). The solution for the position of the particle is given by

$$\langle \Delta T(\Omega) \rangle_{ho} = \frac{1}{(-j\Omega + r_1)(-j\Omega + r_2)} \langle S_{ho}(\Omega) \rangle \tag{3.53}$$

where S_{ho} is a white noise source with a delta-function correlation given by

$$\left\langle S^*_{ho}(x) S_{ho}(x') \right\rangle = D_{ho}\delta(x - x') \tag{3.54}$$

and where the poles $r_{1,2}$ are the same as those in equation (3.50) but replacing Ω_{PM} and τ_p with Ω_{ho} and τ_{ho}, respectively. The spectrum of the rms position jitter of the particle is then given by

$$\left\langle |\Delta T(\Omega)|^2 \right\rangle_{ho} = \frac{D_{ho}}{\Omega^4 + \Omega^2\left(\frac{1}{\tau^2_{ho}} - 2\Omega^2_{ho}\right) + \Omega^4_{PM}} \tag{3.55}$$

The jitter of the damped harmonic oscillator over all frequencies, from equation (3.37), is given by

$$\sigma^2_{ho} = \frac{\tau_{ho}}{\Omega^2_{ho}} D_{ho} \tag{3.56}$$

The notable feature of equation (3.56) is that the jitter of the harmonic oscillator approaches zero with strong filtering ($\tau_{ho} \rightarrow 0$) as long as there exists a finite restoring force Ω_{ho}. Comparing the position jitter spectrum of the damped harmonic oscillator [equation (3.55)] with the timing jitter spectrum for the pulses in a phase-modulated laser [equation (3.46)], we see that the timing jitter spectrum is driven by an additional noise term. This results in an expression for the jitter that has two components: The first component is due to noise driving a change in the carrier frequency. The changes in carrier frequency are converted to timing changes via GVD–this is the well-known Gordon-Haus effect[66]. Unlike the damped harmonic oscillator, we can not reduce the contributions of this term to zero by arbitrarily increasing the restoring force, Ω_{PM}. Increasing the restoring force requires increasing the amount of phase modulation and/or increasing GVD. The amount of phase modulation is limited to values up to 2π, and the

modulation frequency is limited by the repetition rate of the laser and the available bandwidth of the electro-optic modulator, typically under 100 GHz. Increasing the restoring force further requires increasing GVD. However, GVD also appears in the numerator of the first term of (3.52) as D^2, and D^2/Ω_{PM}^2 is linearly proportional to D. So the jitter due to frequency fluctuations increases linearly with GVD. This is true, however, only for the case where the noise contributing to frequency fluctuations, D_{pp}, does not depend on GVD. We will see when we introduce the quantum noise sources that D_{pp} does, in fact, depend on the GVD due to the fact that the pulse width depends on GVD via the area theorem given in (3.4). Filtering helps to control this source of jitter; however, the impact of filtering is limited. Recall from (3.31) that the damping strength, $1/\tau_p$, is proportional to the square of the product of the filter bandwidth and pulse width, $\Omega_f^2\tau^2$. Increasing the damping (reducing τ_p) can be achieved by reducing the filter bandwidth, Ω_f; however, reducing the filter bandwidth increases the spectral losses for the pulse, leading to spectral narrowing of the pulse and a longer pulse in the time domain. Thus the product $\Omega_f^2\tau^2$will not vary much as the laser parameters are changed.

The second component of the timing jitter from (3.52) can be reduced to a minimum level with large restoring force (large Ω_{PM}) and strong damping (small τ_p) such that $\tau_p\Omega_{PM} >> 1$ where the minimum contribution is $\tau_p D_{TT}$. Further reducing the jitter requires increasing the damping further, but as discussed previously, the amount of reduction is limited.

3.4 Quantum-Limited Timing Jitter, AM

In this section, we compute the quantum-limited timing jitter for the case of amplitude modulation by including the explicit contributions from the dominant quantum noise source in the laser, amplified spontaneous emission (ASE) from the gain. The spontaneous emission noise can be modeled as a white-noise source with correlation[43][66][67]:

$$\left\langle S_{qn}(T,t)S_{qn}^*(T',t')\right\rangle = D_{ij}\delta_{i,j}\delta(T-T')\delta(t-t') \tag{3.57}$$

and the corresponding diffusion coefficients become

$$D_{ww,qn} = 4w_0 \frac{2g}{T_R} n_{sp} h\nu \tag{3.58}$$

$$D_{\theta\theta,qn} = \frac{4}{3w_0}\left(1 + \frac{\pi^2}{12}\right)\frac{2g}{T_R} n_{sp} h\nu \tag{3.59}$$

$$D_{pp,qn} = \frac{2}{3w_0\tau^2}\frac{2g}{T_R} n_{sp} h\nu \tag{3.60}$$

$$D_{TT,qn} = \frac{\pi^2\tau^2}{3w_0}\frac{2g}{T_R} n_{sp} h\nu \tag{3.61}$$

where n_{sp} is the enhancement factor due to incomplete inversion of the gain. The diffusion coefficient corresponding to frequency fluctuations, D_{pp}, is inversely proportional to the square of the pulse width: shorter pulses have a larger bandwidth, thus increasing the spectrum in which amplifier noise can couple into. The D_{TT} coefficient due to pulse displacement is reduced for shorter pulses. The total noise power is only a small fluctuation about the steady-state pulse energy, thus the diffusion coefficients are inversely proportional to pulse energy.

Explicitly including the dependencies of the pulse width into the damping terms τ_p and τ_{AM} from (3.31) and (3.32) and the diffusion constants from (3.60) and (3.61) into the expression for the timing jitter for AM in (3.40), we find that the contribution from the first term is proportional to $\Omega_f^4 D^2/w_0$, and the second term is proportional to $1/w_0$, and both of them inversely proportional to the modulation depth:

$$\sigma_{AM}^2 = \frac{4}{M_{AM}\omega_m^2}\frac{g n_{sp} h\nu}{w_0}\left(\frac{9}{2\pi^2}\Omega_f^4 D^2 + 1\right) \tag{3.62}$$

We can make a few statements about (3.62).

- The timing jitter is inversely proportional to the pulse energy. As discussed previously, this is a signal-to-noise term that has come from the diffusion constants and represents noise power compared to signal power.

- The jitter is reduced for high-Q laser cavities (small g). Lower loss implies that fewer photons need to be regenerated per round trip, thus minimizing the ASE contributions.

- The pulse width dependence of the retiming force τ_{AM} and the diffusion constants D_{pp} and D_{TT} has cancelled out–there is no explicit dependence on the pulse width. However,

Parameter	Value
δ	$2\ W^{-1}km^{-1} \cdot L_{eff}$
g_{sat}	0.8
n_{sp}	2
L_{eff}	$150\ m$
M_{PM}	π
M_{AM}	1.0
ω_m	$2\pi \cdot 10\ GHz$
Ω_f	$2\pi \cdot 750\ GHz\ (5.5nm)$
w_0	$2\ pJ$

Table 3.1: Parameters used for timing jitter computations.

there is an implicit pulse width dependence because the pulse width depends on the optical filter bandwidth, pulse energy, and GVD.

- The first term is the contribution from frequency shifts manifested in the amplifier that translate to timing shifts via GVD by the Gordon-Haus effect. The jitter is bound by the restoring force of the modulator and filtering, and the Gordon-Haus noise is proportional to the square of GVD.

- The second term is the contribution from displacement of the soliton pulse by the amplifier– it is independent of GVD and is minimized for large pulse energy and large modulation depth.

For small GVD such that

$$\frac{9}{2\pi^2}\Omega_f^4 D^2 << 1 \tag{3.63}$$

the minimum jitter is independent of GVD and given by

$$\begin{aligned} \left(\sigma_{AM}^2\right)_{\min,ql} &= \tau_{AM} D_{TT} \\ &= \frac{4}{M_{AM}\omega_m^2}\frac{g n_{sp} h\nu}{w_0} \end{aligned} \tag{3.64}$$

The minimum jitter requires the largest possible modulation depth (and, consequently, the deepest modulation well) and large pulse energy. Using typical laser parameters given in Table (3.1), the minimum timing jitter is 78.4 fs^2.

While the minimum jitter approaches zero asymptotically with pulse energy, the pulse energy

is limited by the maximum nonlinear phase shift experienced by the soliton before the onset of instabilities[33][34] where

$$\Phi_{nl} = \frac{D}{\tau^2} = \left(\frac{\delta w_0}{2}\right)^2 \frac{1}{D} \tag{3.65}$$

Excessive phase shifts on the order of π lead to pulse instability. For fixed GVD, the nonlinear phase shift increases with the square of the pulse energy. One can reduce the nonlinear phase shift by employing a dispersion-managed (or stretched-pulse) laser design[68] in which the average GVD is zero while the dispersion is allowed to swing between alternating sections of positive and negative GVD, resulting in a breathing solitary pulse that exhibits less nonlinear phase shift while maintaining a large pulse energy (compared to a path-averaged soliton). Additionally, one could use a large core fiber to allow for the increase of pulse energy without increasing the nonlinearity.

3.5 Quantum-Limited Timing Jitter, PM

The quantum-limited jitter for PM is given by the expression for the jitter in (3.52) with the diffusion coefficients given by (3.60) and (3.61) from the ASE noise source:

$$\sigma^2_{PM} = \left[\frac{D\Omega_f^2}{w_0 M_{PM}\omega_m^2} + \frac{\pi^2\Omega_f^2\tau^4}{4w_0}\left(1 + \frac{8}{9\Omega_f^4\tau^4 D M_{PM}\omega_m^2}\right)\right] 2n_{sp}gh\nu \tag{3.66}$$

We can simplify equation (3.66) considerably for two cases

Case 1 *Overdamped Case:* $8/\left(9\Omega_f^4\tau^4 D M_{PM}\omega_m^2\right) \gg 1$.

Then equation (3.66) simplifies to

$$\sigma^2_{PM} = \left[D\Omega_f^2 + \frac{2\pi^2}{9D\Omega_f^2}\right] \frac{1}{M_{PM}\omega_m^2} \frac{2gn_{sp}h\nu}{w_0} \tag{3.67}$$

Given the operating parameters of Table 3.1, the approximation holds for $D \leq 0.1\ ps^2$. Just as for the case with AM, the explicit dependence on the pulse width has dropped out of the expression. We can make a few observations from equation (3.67):

- The timing jitter is inversely proportional to the pulse energy. This is a signal-to-noise

term that has come from the diffusion constants and represents noise power compared to signal power.

- The jitter is reduced for high-Q laser cavities (small g). Lower loss implies that fewer photons need to be regenerated per round trip, thus minimizing the ASE contributions.
- The Gordon-Haus noise dominates for large GVD and is linearly proportional to GVD.
- For small GVD, the noise due to pulse displacements dominates.
- There exists an optimum dispersion that minimizes the overall timing jitter due to the contributions of both noise terms.

We can also make the following observation in comparing the jitter between AM and PM: for cases where the GVD is large (and the diffusion coefficients are independent of GVD), the increase in jitter with GVD from carrier frequency fluctuations goes as D^2 for AM, but only as D for PM. The explanation is that GVD can assist pulse retiming for PM by converting frequency shifts into timing shifts (provided that one uses adequate filtering to damp out excessive frequency shifts), whereas for AM, GVD does not assist pulse retiming and only increases the jitter via the Gordon-Haus effect. Thus for cases where the GVD is large, using PM is more effective than AM in reducing the jitter. We can solve for the GVD that minimizes the jitter due to the contributions from both noise components

$$D_{opt,ql} = \frac{\pi}{\Omega_f^2}\sqrt{\frac{2}{9}} \tag{3.68}$$

and the minimum jitter is given by

$$\left(\sigma_{PM}^2\right)_{\min,ql} = 2\pi\sqrt{\frac{2}{9}}\frac{1}{M_{PM}\omega_m^2}\frac{2gn_{sp}h\nu}{w_0} \tag{3.69}$$

The optimum dispersion that achieves the minimum timing jitter for PM depends solely on the filter strength. The minimum jitter is inversely proportional to the pulse energy, as we might expect based on noise-to-signal power ratio, and inversely proportional to the phase shift per round trip exacted by the phase modulator. Filtering and GVD do not appear explicitly in the expression for the minimum jitter.

Case 2 *Underdamped Case:* $8/\left(9\Omega_f^4\tau^4 D M_{PM}\omega_m^2\right) \ll 1$

Then equation (3.66) simplifies to

$$\sigma_{PM}^2 \sim \left[\frac{D}{\tau^2} + \pi^2\tau^2 M_{PM}\omega_m^2\right] \frac{\Omega_f^2\tau^2}{M_{PM}\omega_m^2} \frac{2gn_{sp}h\nu}{w_0} \tag{3.70}$$

For the parameters from Table 3.1, we find that $\pi^2\tau^2 M_{PM}\omega_m^2 \ll D/\tau^2$, so we can further simplify (3.70) to

$$\sigma_{PM}^2 \sim \frac{D\Omega_f^2}{M_{PM}\omega_m^2} \frac{2gn_{sp}h\nu}{w_0} \tag{3.71}$$

Equation (3.71) indicates that the jitter increases linearly with GVD. For typical laser parameters given in Table 3.1, the minimum jitter is 37.2 fs^2, and the optimum GVD is $D = 0.0064$ ps^2. Again, the minimum jitter asymtotically approaches zero as the pulse energy increases, with the limit on allowable pulse energy set by the onset of pulse instabilities. For small GVD, the jitter grows quickly, indicative of the fact that phase modulation requires some GVD for pulse retiming, and for large GVD, the jitter is linearly proportional to D.

3.6 Comparison Between AM and PM for Quantum-Limited Noise

In general, we want to compare the minimum quantum-limited timing jitter between AM and PM. We define R as the ratio of AM to PM jitter. Where this ratio is below unity, AM yields lower timing jitter, and above unity, PM yields lower timing jitter. We can evaluate the minimum ratio where we have independently adjusted the GVD for AM and PM. For AM, we adjust GVD such that $9D^2\Omega_f^4/2\pi^2 << 1$, and for PM, we use the optimum GVD from equation (3.68). From equations (3.64) and (3.69), the ratio is

$$\frac{\left(\sigma_{AM}^2\right)_{\min,ql}}{\left(\sigma_{PM}^2\right)_{\min,ql}} = \frac{1}{\pi}\sqrt{\frac{9}{2}}\frac{M_{PM}}{M_{AM}} \tag{3.72}$$

It is a remarkable fact that although the physics of timing restoration between AM and PM is quite different, we find that the ratio of the minimum timing jitter between the two configurations depends solely on the ratio of the modulation depths.

It makes sense to talk about M_{AM} as an extinction ratio proportional to the drive power of the amplitude modulator: the action of amplitude modulation is interferometric, thus the maximum extinction between the "off" and "on" states is unity. For PM, this is not the case, as the "modulation well" is formed with the combined action of phase modulation plus filtering. M_{AM} is limited to a value of one for complete extinction, whereas M_{PM} can take on values up to π and greater, thus the M_{AM}/M_{PM} term can be as small as $1/\pi$ for the same drive power. This makes intuitive sense when we consider the action of the phase modulator on the pulse spectrum: ignoring for the moment the action of gain, loss, and nonlinearity, the phase modulator puts a linear chirp on the pulse, as

$$\begin{aligned} \frac{\partial}{\partial T}a &= -j\frac{1}{T_R}\frac{M_{PM}}{2}\left[1-\cos(\omega_m \Delta T)\right]\, a \\ &\sim j\frac{1}{T_R}\frac{M_{PM}}{2}\left(\omega_m \Delta T\right)^2 a \end{aligned} \tag{3.73}$$

So, placing the reference frame at $z = 0$,

$$a(z, \Delta T) \sim \exp\left[j\frac{1}{T_R}\frac{M_{PM}}{2}\left(\omega_m \Delta T\right)^2 z\right] \tag{3.74}$$

and the chirp becomes $\delta\omega \equiv -\dfrac{d}{dt}\phi = \dfrac{1}{T_R}M_{PM}\omega_m^2 \Delta T\ z$. The additional effect of dispersion is to increase the spectral width with propagation distance, much like the temporal expansion of a beam in a highly dispersive medium. The spread spectrum experiences loss in the filter via gain dispersion.

Taking the values for the same power driving each modulator from Table 3.1, $M_{AM} = 1$ (full extinction, requiring a differential phase shift of π in a Mach-Zender type interferometer) and $M_{PM} = \pi$ (requiring an additive phase shift of π in the same interferometer), we find that $\left(\sigma_{AM}^2\right)_{\min} / \left(\sigma_{PM}^2\right)_{\min} = 2.1$, indicating that the timing jitter for PM can be twice as small as that for AM.

3.7 Conclusions

Using the soliton perturbation theory, we derived the equations of motion for the pulse parameters and derived analytical expressions of the timing jitter for both AM and PM. For AM,

the quantum-limited jitter increases with the square of GVD, D^2, due to the Gordon-Haus noise, and the minimum jitter is proportional to the pulse energy and the modulator curvature. For PM, we derived an equation of motion for the pulse timing and identified it as that of a damped harmonic oscillator in which the damping is provided by filtering and the restoring forces provided by the phase modulator and GVD. For mistimed pulses, the phase modulator imparts a frequency shift that is converted to a timing shift via GVD. While an increase in the GVD increases the effect of Gordon-Haus noise, the GVD also assists the retiming force, thus for large GVD, the jitter increases only linearly with D. Thus, in a laser where the GVD is large, PM can be much more effective in reducing the jitter than AM. For small GVD, the noise that imparts pulse displacements dominates over the Gordon-Haus effect, but the phase modulator can not restore timing effectively without GVD, thus the quantum-limited jitter for small GVD in inversely proportional to D. We derived the optimum GVD that minimizes the jitter for PM. For both AM and PM, filtering helps to control the jitter. The ratio of the minimum quantum-limited jitter between AM and PM is proportional to the relative strengths of modulation depth. While the modulation depth for AM is limited to unity, the modulation depth for PM can be as large as π. The quantum-limited jitter for PM can be less than the jitter for AM by as much as a factor of two. For both AM and PM, the quantum-limited jitter is inversely proportional to the pulse energy.

3.8 Ideas for Future Work

Using dispersion-management in the laser cavity should allow the laser to be operated with low average GVD while maintaining large pulse energies. However, achieving large stretching ratios in short lengths is a challenge when operating with picosecond pulses and may require the use of fiber-Bragg gratings or other dispersive elements.

It has been argued[69] that for the case of phase modulation and GVD, the perturbation theory yields non-orthogonal expansion functions that may give rise to additional noise terms under certain conditions (similar to the case of continuum generation by a soliton). This should be a topic explored further.

Chapter 4

Retiming Dynamics

4.1 Introduction

[1]In chapter 3, an analytical expression for the timing jitter in actively modelocked lasers for the cases of amplitude (AM) and phase (PM) modulation were derived from soliton perturbation theory (SPT), and the resulting spectra of the timing jitter were described in terms of characteristic time constants determined by the laser parameters and noise sources[37][36]. The characteristic time constants govern the laser response to noise that leads to timing jitter and thus are crucial for an understanding of the physics of timing jitter. In this chapter, we demonstrate an experimental apparatus that enables the measures of the characteristic time constants for both amplitude (AM) and phase (PM) modulation, and we compare the results to those derived from theory. In addition, the measurement technique allows us to directly observe the pulse retiming dynamics in real time.

[1]The work appearing in this section benefitted greatly from useful discussions with Moti Margalit, Paul Juodawlkis, and John Twichell. Results from this section can also be found in Refs. [46][70].

4.2 Theory

In chapter 3, we derived the equations of motion from the master equation for modelocking describing the evolution of a pulse in an actively modelocked laser with SPM and GVD:

$$T_R\frac{\partial}{\partial T}a = +iD\frac{\partial^2}{\partial t^2}a + i\delta|a|^2a + \left[g - l + \frac{1}{\Omega_f^2}\frac{\partial^2}{\partial t^2} - \frac{1}{2}\left(M_{AM} + jM_{PM}\right)\left(1 - \cos(\omega_m t)\right)\right]a + T_R S(t,T)$$

M_{AM} and M_{PM} were defined as the depths of amplitude and phase modulation, respectively. M_{AM} is a loss parameter proportional to the drive power of the amplitude modulator. The modulator is typically an electro-optic device with patterned single-mode interferometric waveguides. In lithium niobate, the achievable extinction rates are on the order of 20-25 dB between the "on" and "off" state when operated in transmission. The largest modulation depth for the AM modulator is 1.0. For PM, this is not the case (as discussed in chapter 3)–M_{PM} can take on values exceeding π.

Using SPT, we found equations of motion for the pulse timing, ΔT, and the carrier frequency (or momentum), Δp:

$$\frac{\partial}{\partial T}\Delta p = -\frac{1}{\tau_p}\Delta p + \frac{M_{PM}\omega_m^2}{T_R}\Delta T + T_R S_p(T) \tag{4.1}$$

$$\frac{\partial}{\partial T}\Delta T = -\frac{2D}{T_R}\Delta p - \frac{1}{\tau_{AM}}\Delta T + T_R S_T(T) \tag{4.2}$$

where

$$\frac{1}{\tau_{AM}} = \frac{\pi^2}{6}M_{AM}\omega_m^2\tau^2\frac{1}{T_R} \tag{4.3}$$

$$\frac{1}{\tau_p} = \frac{4}{3\Omega_f^2\tau^2} \tag{4.4}$$

$$\Omega_{PM} = \sqrt{2DM_{PM}\omega_m^2}\frac{1}{T_R} \tag{4.5}$$

The S_i terms (for $i = w, p, \theta, T$) are the projections of the noise S onto each of the pulse

parameters. The perturbation theory produced a set of coupled ordinary differential equations of motion that govern how the pulse carrier frequency (p) and pulse timing (T, measured with respect to the phase of the external microwave frequency source) evolve in the presence of noise. That evolution depends on the set of constant coefficients–given in equations (4.3) – (4.5)–and noise terms, and the coefficients depend only on the laser parameters. In this chapter, it is our goal to verify the laser-parameter dependencies for the characteristic constants. We will study the retiming dynamics separately for the two cases of amplitude and phase modulation.

4.3 Actively Modelocked Fiber Ring Laser

The modelocked fiber laser used for the experiment is shown in Fig. 4-1. The fiber laser is 167 m long–corresponding to a 1.2 MHz free spectral range (833 ns round-trip time)–and is constructed with polarization-maintaining fibers (and devices with polarization-maintaining pigtails). An isolator ensures unidirectional operation. Reduced dispersion (achieved by use of a 100 m of dispersion-shifted fiber) in combination with spectral filtering (achieved by insertion of a 5.5-nm bandwidth angle-tuned interference dielectric filter) permits effective supermode suppression[48]. The modulator is a Lucent m2122a Mach-Zender type and can be configured for either AM or PM action, as described in a below subsection. The laser is optically pumped at 980 nm with approximately 300 mW from a semiconductor master oscillator power amplifier. The output power is $\sim$4 mW extracted from a 10 % output coupler.

The pulse characteristics could be varied by adjusting the pump power, optical filtering bandwidth, modulation depth, and average GVD. Typical characteristics for the pulse width, optical spectrum, and RF spectrum are given in Figs. 4-2, 4-3, and 4-4, respectively. The autocorrelations were obtained via second-harmonic generation with a 2 mm POM crystal in a noncollinear geometry and double chopping (to eliminate the background). The pulse width given is the full width at half maximum (FWHM) for a best fit line assuming a hyperbolic secant pulse shape, as given by the dotted curve. The dynamic range between the signal and background was greater than 23 dB and limited only by the A/D converter of the lock-in detector (8 bits of resolution $\simeq$24 dB dynamic range). From the curve in Fig. 4-2, the agreement is good over the extent of the pulse shape. The optical spectrum is shown in Fig. 4-

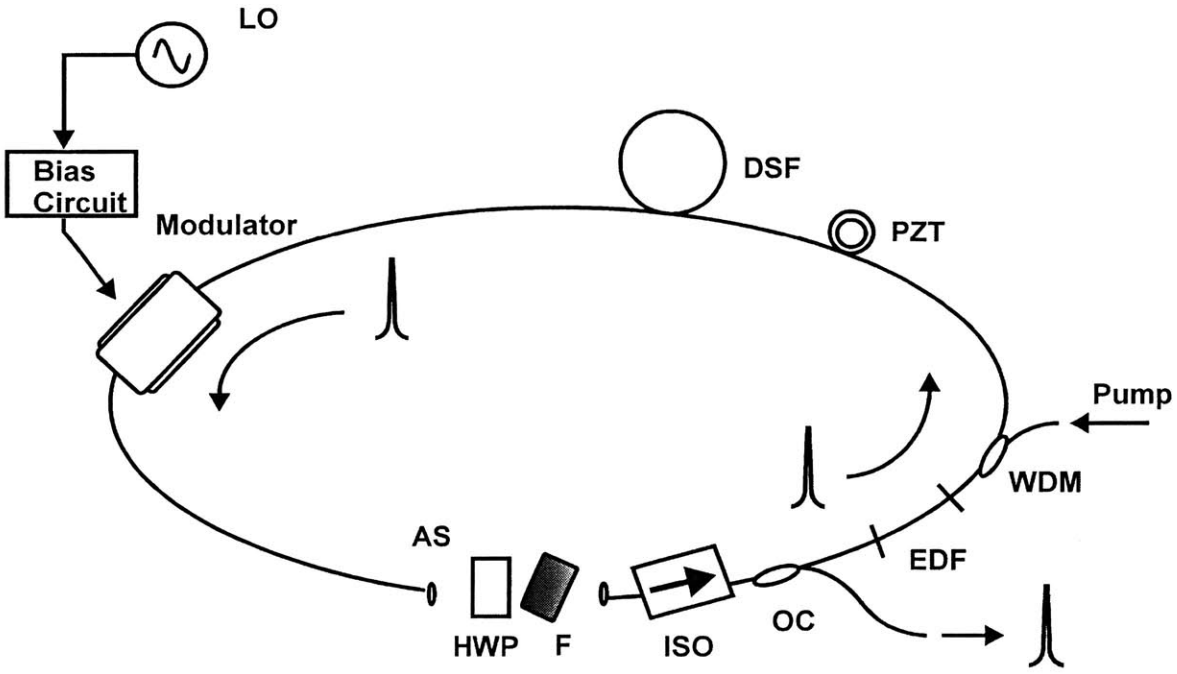

Figure 4-1: Fiber ring laser schematic for retiming measurements. All fibers and fiber pigtails constructed with polarization-maintaining fiber. ISO is a two-stage isolator, EDF erbium-doped fiber, WDM wavelength division multiplexer for the 980 nm pump, PZT fiber-wound piezo-electric cylinder, DSF dispersion-shifted fiber, LO local oscillator, AS aspheric lens, HWP half-wave plate, F interferometric tunable filter, and OC a 10% output coupler.

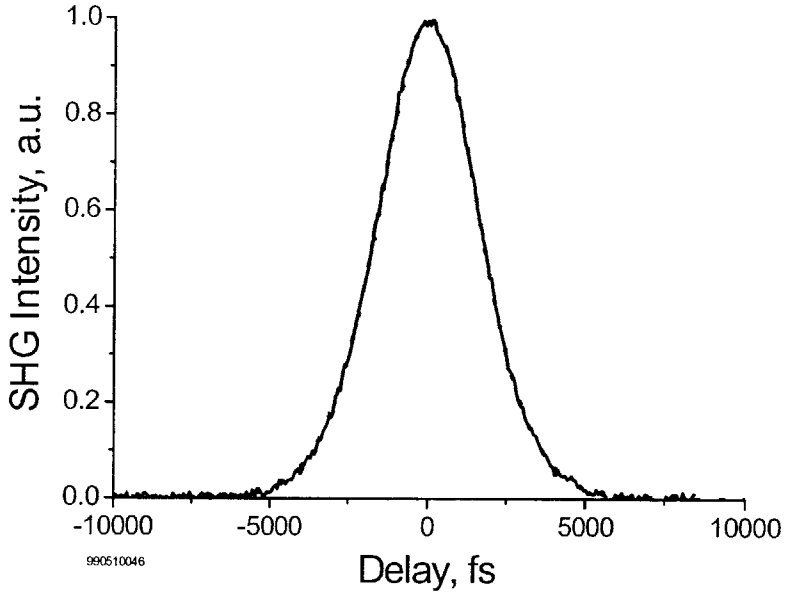

Figure 4-2: Typical trace of the intensity of the second-harmonic in a non-colinear, background-free autocorrelation as a function of delay. Dotted curve assumes a hyperbolic secant pulse shape with a full-width-at-half-maximum pulse width of 2.39 ps.

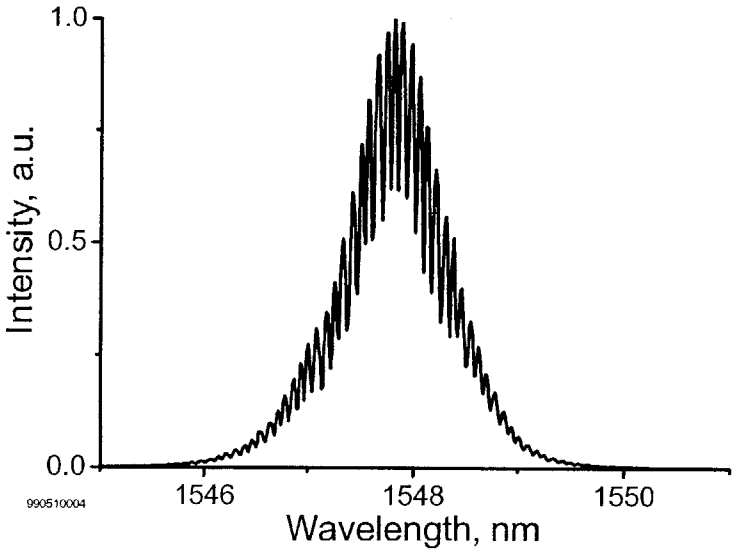

Figure 4-3: Intensity of the optical spectrum (linear scale) as a function of wavelength. The 10 GHz fringes are resolved with a ~0.08 nm instrument resolution bandwidth.

3. The maximum resolving power of the optical spectrum analyzer is ~0.08 nm, corresponding to ~10 GHz resolution, and the 10.0012 GHz modes can be resolved. The RF spectrum of the photogenerated current after direct detection is shown in Fig. 4-4 with supermode suppression > 70 dB, indicative of very stable laser operation.

4.4 Experimental Setup for Retiming Measurements

The experimental setup is shown in Fig. 4-5. Just a simplified schematic of the fiber laser (previously described) is shown in the figure. The bias circuit allows the modulator to be operated with any combination of amplitude and phase modulation (see Appendix B). The phase shifter imparts a discrete change in the phase of the LO whenever the control signal CLK goes high or low (see Appendix C).

The RF phase detection circuit is shown in Fig. 4-5. The input optical pulses are photodetected, lowpass filtered such that the higher harmonics of the repetition rate are filtered out, and amplified before entering the RF port of a double-balanced mixer—the signal is sinusoidal

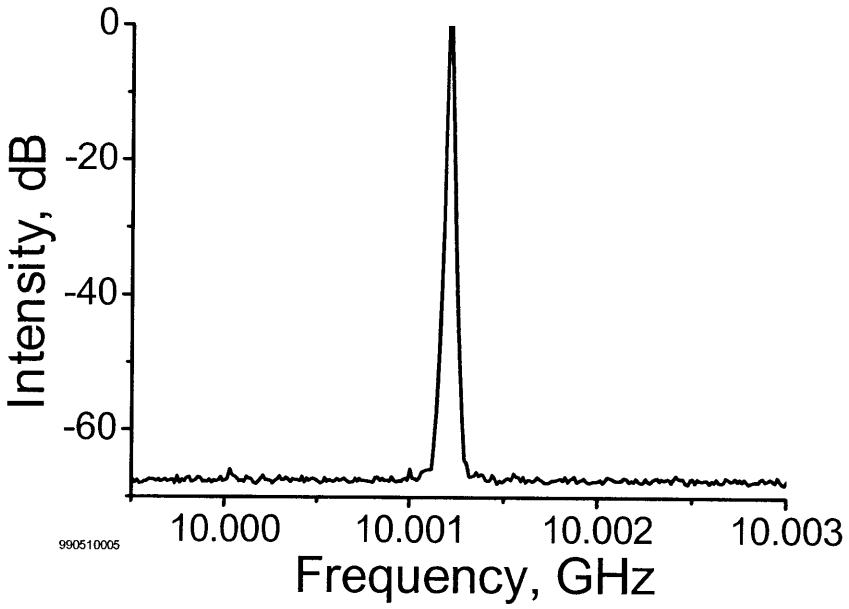

Figure 4-4: Intensity of the radio-frequency spectrum (log scale) near 10.0 GHz. The supermodes are suppressed by over 70 dB.

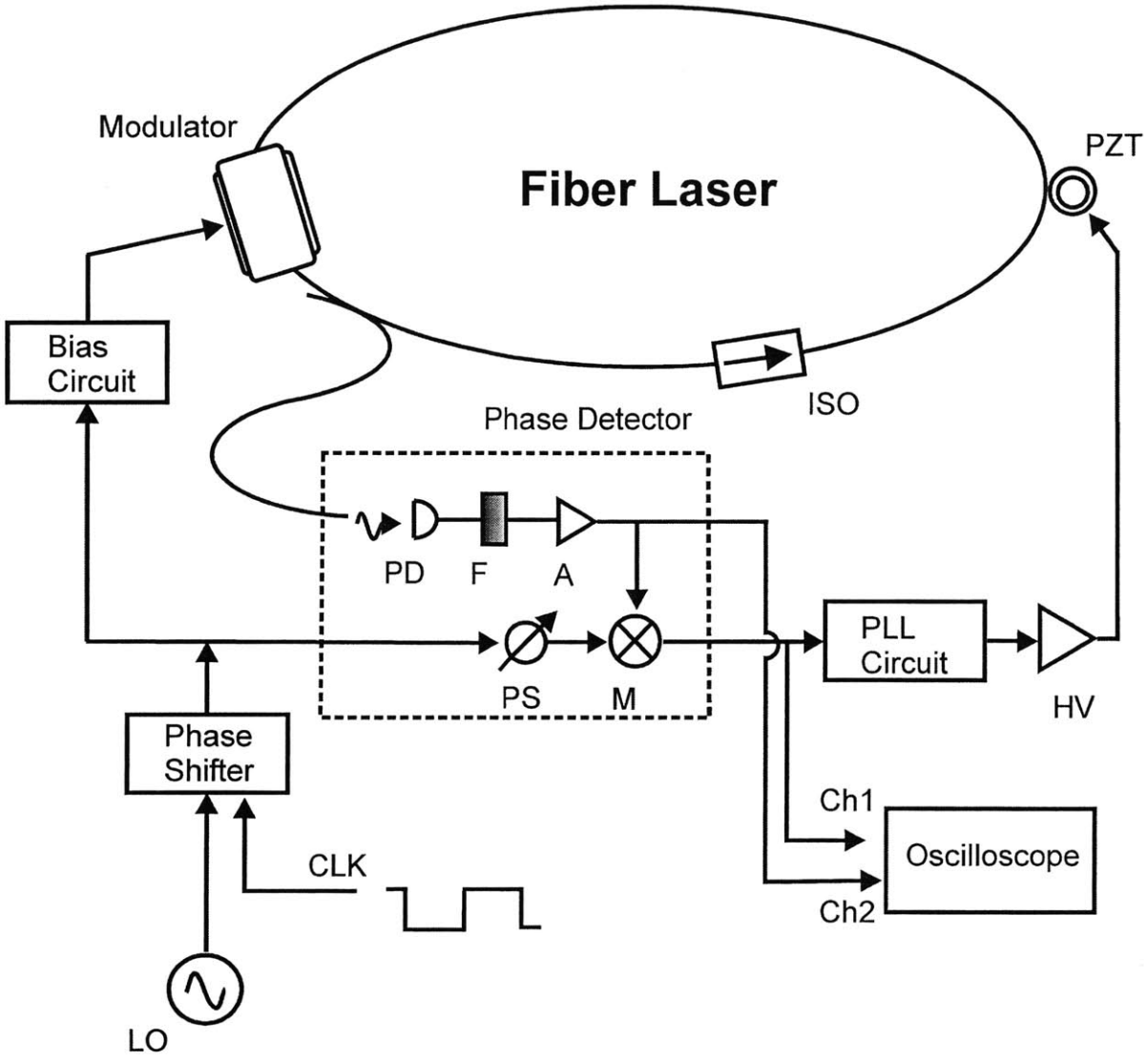

Figure 4-5: Retiming measurement setup. LO local oscillator at 10 GHz, CLK is a TTL pulse train that triggers the phase shifter to alternate the RF phase of the LO delivered to the modulator between two phase states, PS microwave phase shifter, M double-balanced mixer, PD 16 GHz photodiode, F 10 GHz bandpasss filter, A preamplifier, PLL phase-locked loop, HV high-voltage amplifier, PZT fiber-wound piezo-electric transducer, ISO isolator.

with a phase jitter determined by the timing jitter of the laser pulses. The LO signal (after passing through the phase shifter) is input into the LO port of the mixer as well. The LO and laser are phase-locked together, and the carrier frequency of the LO (in this case, 10 GHz) is the same as the laser repetition rate. By proper biasing the phase shifter such that the RF and LO are in quadrature, the output voltage of the mixer (also referred to as the IF port) is proportional to the phase difference between the LO and RF signal (also see chapter 5 on timing jitter measurements for more detail). In other words, the IF voltage is a measure of the distance between the pulses and the center of the modulation window. Also, quadrature detection reduces amplitude fluctuations from the laser pulses by $\sim$10 dB.

In order to maintain active modelocking, the length of the cavity must be set to a subharmonic of the LO frequency to within $\sim$10 kHz. In order to maintain locking, the fiber laser was enclosed in a metal box and temperature controlled to within $\pm 0.01C$ as measured with an RTD temperature sensor. Assuming an index change of 1.1×10^{-5}per degree C, the cavity drift was ± 1.7 Hz. However, it was found that the laser would not maintain modelocking for more than a few minutes without having to adjust either the cavity length or the synthesizer frequency by a few hundred Hz. A phase-locked loop (PLL) with analog control circuitry was constructed in order to maintain modelocking. The voltage from the phase detector (described above) was used as the error signal for the PLL. An inverting proportional control circuit shown in Appendix D (Fig. D-2) provides an integrating pole and a zero for lead-lag control of the PLL. The output of the circuit drives a high-voltage PZT driver (Burleigh PZ-70, adjustable gain and DC offset) that drives a fiber-wound PZT cylinder (wound with $\sim$12 m dispersion-shifted polarization-maintaining fiber). In order that the PLL not interfere with the measured time constants, the loop bandwidth was reduced to < 2 Hz. The noninverting control circuit of Fig. D-1 given in Appendix D seemed to work equally well as the inverting circuit.

4.4.1 Amplitude Modulation

For pure amplitude modulation (with PM set to zero), the governing equations of motion are simplified to

$$\frac{\partial}{\partial T}\Delta p = -\frac{1}{\tau_p}\Delta p + T_R S_p(T) \tag{4.6}$$

$$\frac{\partial}{\partial T}\Delta T = -\frac{2D}{T_R}\Delta p - \frac{1}{\tau_{AM}}\Delta T + T_R S_T(T) \tag{4.7}$$

While we have previously derived the retiming dynamics of pulses using amplitude modulation by employing soliton perturbation theory (see section 3.2), a more straightforward derivation for τ_{AM} can be made. Consider a Gaussian pulse given by

$$a(t) = \exp\left(-t^2/2\tau^2\right) \tag{4.8}$$

with pulse width τ. We will artificially shift the pulse in time by a small amount δt and ask for the changes to δt as it passes through a modulator. For the case of amplitude modulation with depth of modulation M_{AM} and sinusoidal drive frequency of $f_m = \omega_m/2\pi$, we can write the transmission function as

$$M(t) = 1 - \frac{M_{AM}}{2}\omega_m^2 t^2 \tag{4.9}$$

The pulse upon exiting the modulator is modified to yield

$$\begin{aligned} b(t) &= M(t)a(t) \\ &= \left[1 - \frac{M_{AM}}{2}\omega_m^2 t^2\right] \exp\left[-(t-\delta t)^2/2\tau^2\right] \end{aligned} \tag{4.10}$$

The pulse is shifted to a new position $\delta t'$. We can solve for the shift $(\delta t - \delta t')$ and find that the pulse is shifted by $M_{AM}\omega_m^2\tau^2$ per pass through the modulator, resulting in a retiming constant $\tau_{AM} \propto M_{AM}\omega_m^2\tau^2/T_R$. This is identical to equation (3.32) obtained using soliton perturbation theory in chapter 3.

The experiment proceeds as follows: at $t = 0$, an instantaneous "kick" is applied to the phase of the 10 GHz LO signal using the microwave phase shifter. This is equivalent to shifting the position of the pulse by an amount ΔT relative to the LO modulation, as depicted in Fig. 4-

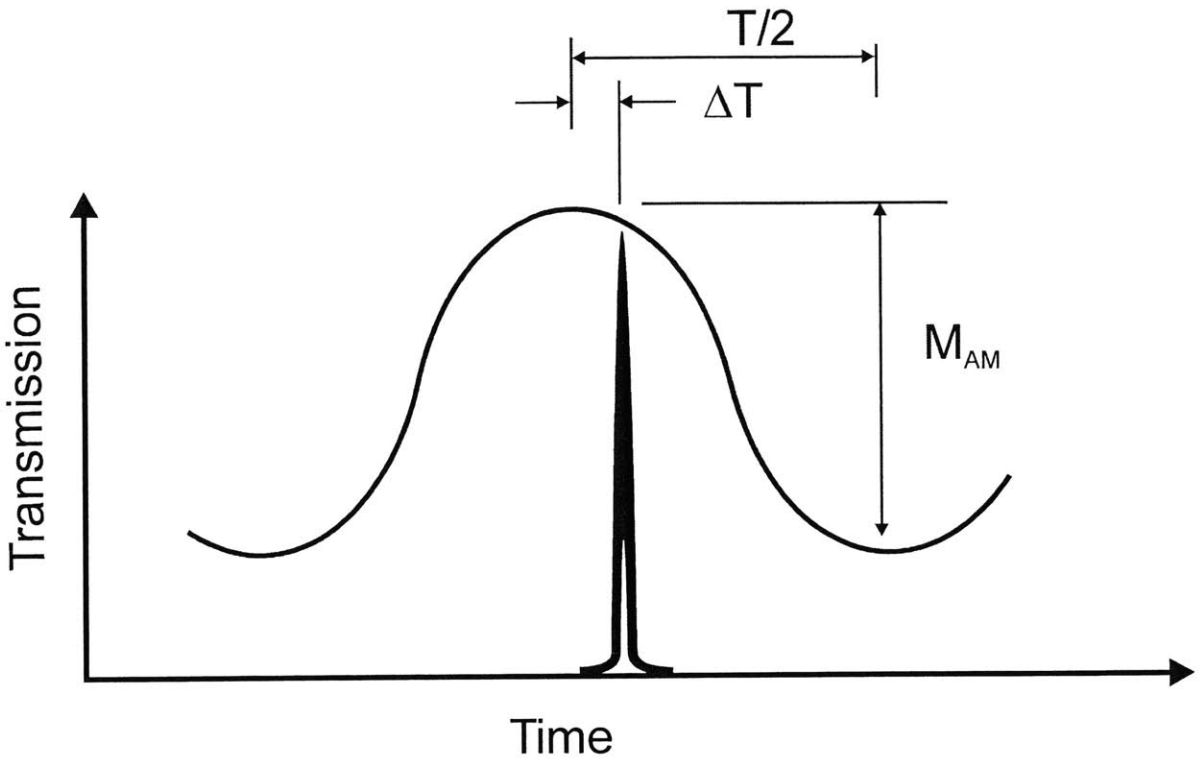

Figure 4-6: Illustration of the transmission of a mistimed optical pulse through an amplitude modulator. ΔT is the instantaneous position of the pulse with respect to the point of maximum modulator transmission, M_{AM} is the modulation depth (values range from 0 to 1), and 1/T is the pulse repetition rate.

6. With the microwave phase detector properly biased, the IF output voltage of the mixer is proportional to ΔT. By monitoring this voltage on an oscilloscope, we can directly observe the dynamics of the pulse as it relaxes to its unperturbed state. Equation (4.7) suggests that, for a step-wise perturbation of the pulse timing and no perturbation of the carrier frequency, the pulse retiming dynamics are governed by a simple first-order exponential of the type

$$\Delta T(T) = \Delta T_0 \exp\left(-\frac{T}{\tau_{AM}}\right) \tag{4.11}$$

where ΔT_0 is the initial perturbation of the pulse position using the microwave phase shifter. A typical measured trace for the case of AM is given in Fig. 4-7. Before $t = 0$, the pulse is near the center of the modulation and $\Delta T(t > 0) = 0$. At $t = 0$, the microwave switch

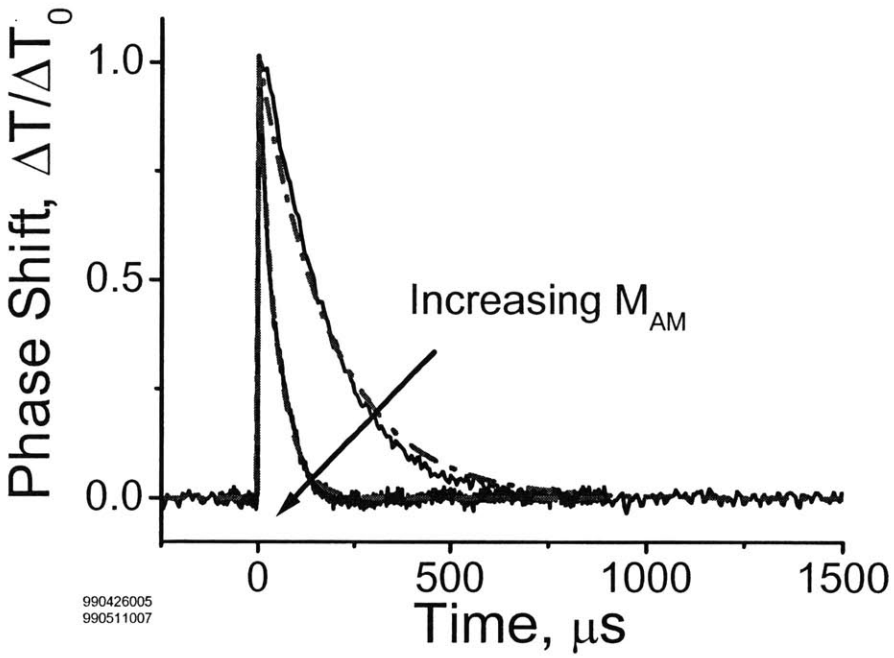

Figure 4-7: Retiming dynamics for the case of AM for two different modulation depths. Solid dark curve, data; dashed and dashed-dotted curves, fit to first-order exponentials.

is activated, the pulse is now shifted from the center of the modulation by ΔT_0 such that $\Delta T(t = 0) = \Delta T_0$. It is seen that after the initial perturbation, the pulse position relaxes back to its original quiescent state at $\Delta T = 0$ at an exponential rate. The dotted curve is the best fit for a first-order exponential recovery with time constant τ_{AM}. By changing the modulation depth, the time constant decreases and the timing recovery happens at a faster rate, as shown in the figure. The time scales of the slower and faster relaxation times shown in Fig. 4-7 are $\sim$200 μs and $\sim$600 μs. Because the roundtrip time of the laser is 833 ns, this relaxation rate corresponds to $\sim$240 and $\sim$720 round trips, respectively.

While monitoring the relaxation rate, the amplitude fluctuation were also monitored (as shown in the setup of Fig. 4-5)–a sample trace is shown in Fig. 4-8. The average power was monitored by tracking the photocurrent after direct detection of the laser pulses using a fast photodetector (3-dB BW $\sim$3 GHz) triggered by the clock controlling the microwave switch.

After the phase kick at $t = 0$, the average power fluctuates by $\sim$2 percent and oscillates for a few hundred microseconds at a rate of $\sim$52 kHz. This rate is also the relaxation oscillation frequency of the fiber laser. The excitation of the relaxation oscillation is most likely caused by the action of the microwave switch as it changes from one state to another, during which time the modulator drive power turns off during the switching. Another explanation is the fact that in the act of instantaneously switching the LO phase, the pulse experiences an instantaneous loss due to the decreased transmission through the modulator. If this were the case, then the amplitude fluctuation should increase as the initial perturbation, ΔT_0, is increased. This was not the case, however, suggesting that the power actually is shut off during the 25 ns as the microwave switch changes from one state to another, as verified by further experiments. The excitation of the relaxation oscillation did not affect the measurement of the time constants because the timing recovery occurred on a much longer time scale, and fluctuations of the average power are suppressed by $\sim$10 dB.

Timing recovery curves were taken for an array of laser parameters by varying the pump power, optical filtering, and modulation depth. For each timing recovery curve, autocorrelations were taken to measure the pulse width. The modulation depth was measured by monitoring the RF power delivered to the modulator using a directional coupler and normalizing it to the power needed to drive the modulator between maximum and minimum optical transmission (data provided by the manufacturer) so that M_{AM} takes on values from 0.0 to 1.0. The retiming constant τ_{AM} was measured for each trace and compared with the theoretical value, as shown in Fig. 4-9. The agreement between the data and the theory is good over a wide range of τ_{AM} values and within experimental uncertainty.

The time constant was also tested as a function of the magnitude of the phase kick, ΔT_0, and shown in Fig. 4-10. Increasing the size of the kicks (while remaining much less than $\pi/4$ (i.e., less than 12.5 ps over 100 ps period) did not change the retiming constant. As evident from the fourth trace in the figure where a large phase kick ($>\pi/4$) was used, the timing recovery exhibited a recovery described with two time constants, and the directly-detected and monitored power fluctuations increased. Pushing the phase kicks to larger offsets led to large oscillations of the average power and large oscillations in the timing recovery. Testing the timing constants in this regime go beyond the parabolic approximation of the modulation function and are not

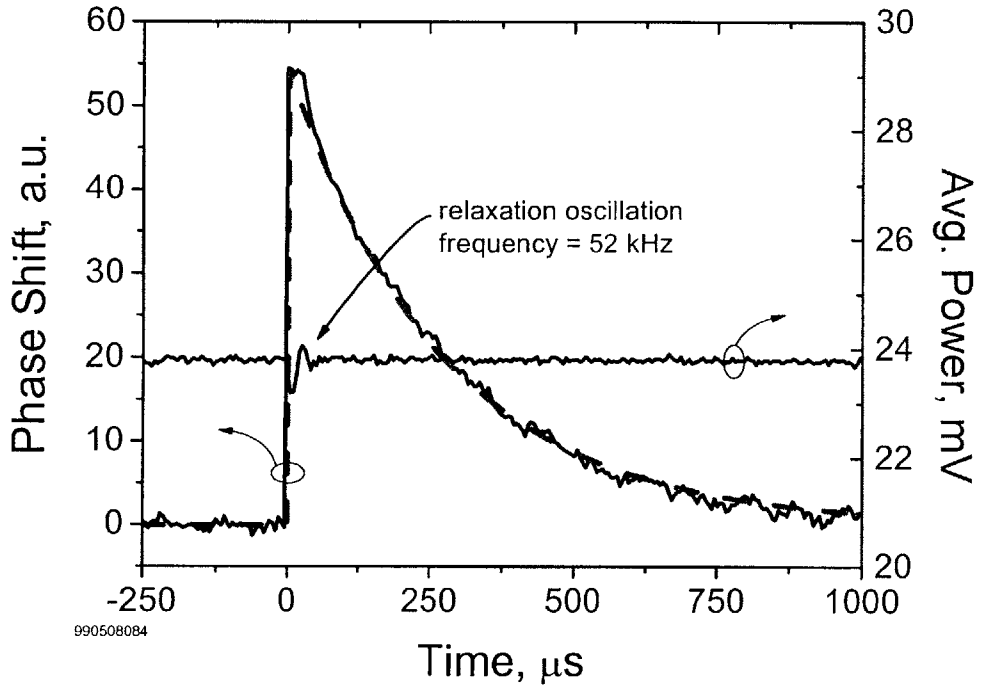

Figure 4-8: Dynamic timing recovery for the case of AM (solid and dashed curve) and measurement of amplitude perturbations via direct detection of the laser pulses with a slow detector. The power oscillation corresponds toa relaxation oscillation frequency of $\sim$ 52 kHz.

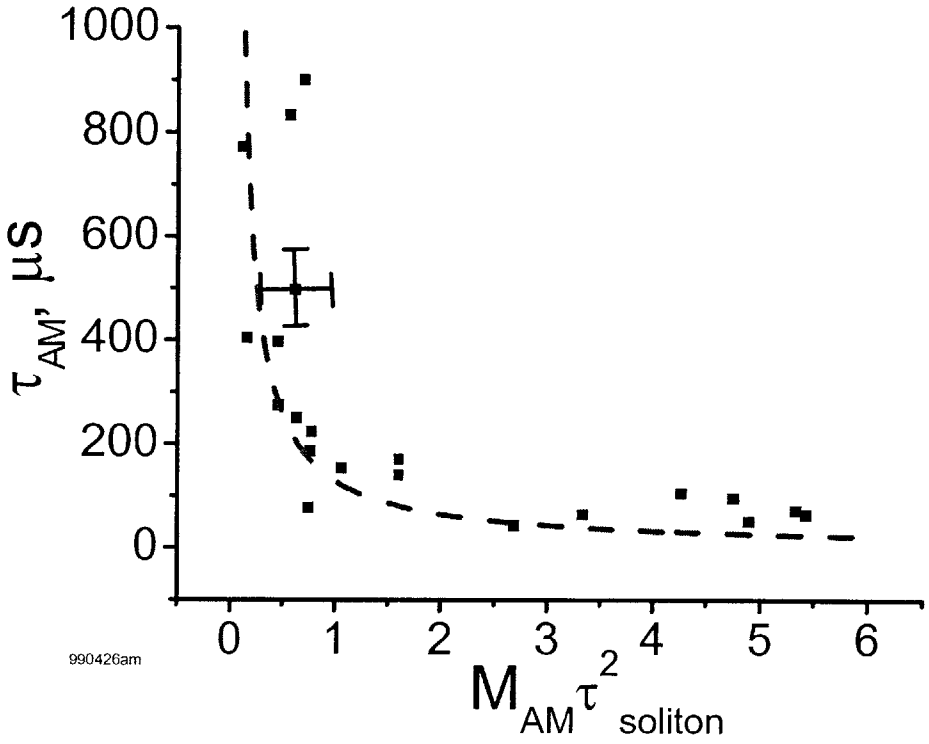

Figure 4-9: Plot of the characteristic time constant τ_{AM} due to amplitude modulation as a function of modulation depth and pulsewidth; dots indicate data points, dotted curve indicates theory. Error bars for the data set are shown on one of the data points.

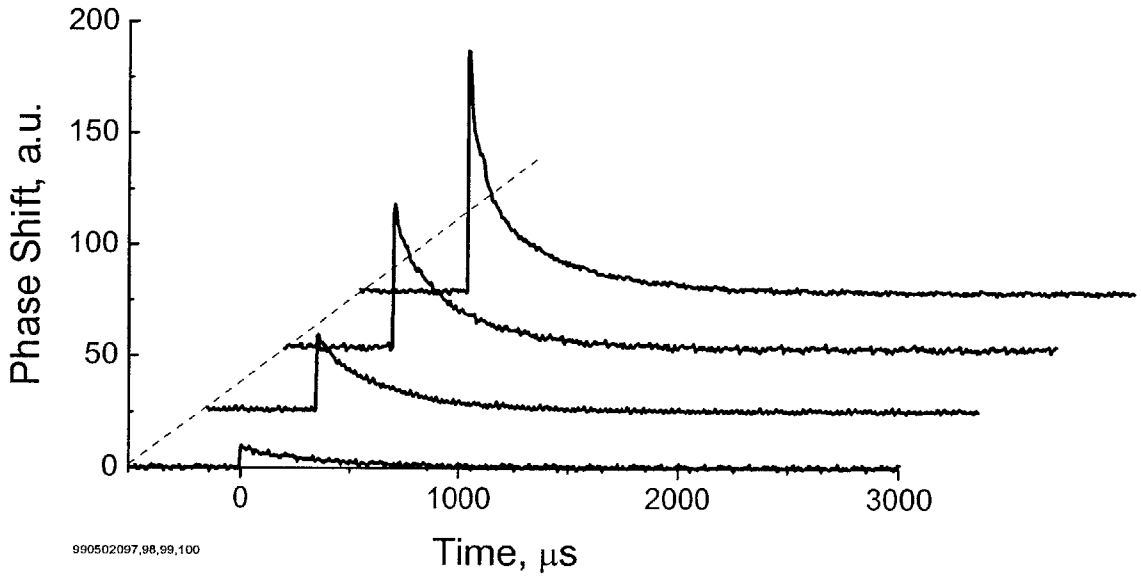

Figure 4-10: Retiming traces for various initial perturbations where the initial offset ΔT_0 was changed, ranging from $0.017\pi, 0.059\pi, 0.11\pi$, and 0.19π where the phase shift on the vertical axis is calibrated as 280 mV=$\pi/2$ radians.

applicable for studies in this thesis.

The pulse width was measured for each value measurement of τ_{AM}. As the depth of modulation was varied (by attenuating the power applied to the modulator), the pulse width τ also varied but only as a very weak function of M_{AM}. The measured dependence is given in Fig. 4-11 for two different settings of pump power. The presence of soliton effects shorten the pulse compared to its Siegman-Kuizenga pulse width and give the pulse its characteristic hyperbolic secant shape, as shown in Fig. 4-2. The solid curve of Fig. 4-11 shows the dependence assuming purely Siegman-Kuizenga active modelocking in which the pulse width is inversely proportional to the fourth root of the modulation depth $\tau_{S-K} \propto \sqrt[-4]{M_{AM}}$. The dependence shown in the figure for both data sets is much weaker. The best empirical fit to the data is given by $\tau \propto \sqrt[-5.7]{M_{AM}}$.

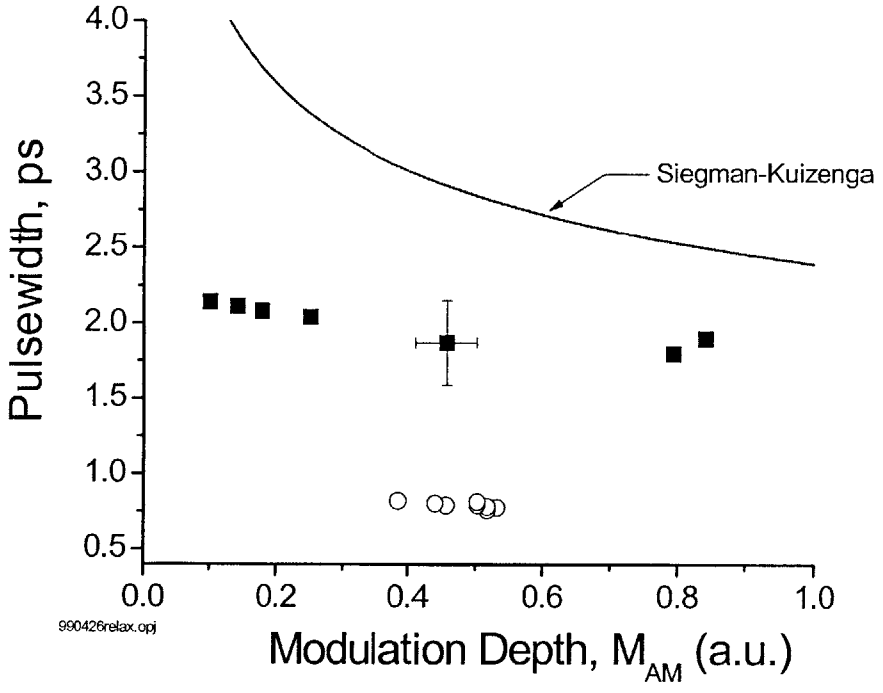

Figure 4-11: Pulse width as a function of modulation depth for the case of amplitude modulation, with the pulse width for Siegman-Kuizenga active modelocking also shown (solid line). The filled squares and empty circles are data for two different pump powers. Error bars for the data sets are shown on one of the data points.

4.4.2 Phase Modulation

The same class of experiments were performed using phase modulation (with amplitude modulation set to zero). The equations of motion in that case are given by

$$\frac{\partial}{\partial T}\Delta p = -\frac{1}{\tau_p}\Delta p + \frac{M_{PM}\omega_m^2}{T_R}\Delta T + T_R S_p(T) \tag{4.12}$$

$$\frac{\partial}{\partial T}\Delta T = -\frac{2D}{T_R}\Delta p + T_R S_T(T) \tag{4.13}$$

For a perturbation of the pulse position only, $S_p(T) = 0$, and we can simplify the equation of motion to the second-order differential equation given by

$$\frac{\partial^2}{\partial T^2}\Delta T + \frac{1}{\tau_p}\frac{\partial}{\partial T}\Delta T + \Omega_{PM}^2 \Delta T = \left(\frac{\partial}{\partial T} + \frac{1}{\tau_p}\right) S_T(T) \tag{4.14}$$

This is the equation of motion for a driven, damped harmonic oscillator with damping time and natural oscillation frequency given by

$$\frac{1}{\tau_p} = \frac{4}{3\Omega_f^2 \tau^2}\frac{1}{T_R} \tag{4.15}$$

$$\Omega_{PM} = \sqrt{2DM_{PM}\omega_m^2}\frac{1}{T_R} \tag{4.16}$$

Unlike the case for AM, the dynamics of pulse retiming for PM requires two constants, given by τ_p and Ω_{PM}. For the experimental conditions of our setup, $\Delta T(t=0) = \Delta T_0$ is the initial kick that we can set, and $\frac{\partial}{\partial T}\Delta T(t=0) = 0$ since the momentum of the pulse immediately after displacement is zero. The initial value problem is easily solved, and the solutions of (4.14) have a character governed by the product $4\left(\tau_p \Omega_{PM}\right)^2$:

- **Case 1** *Underdamped:* $4\left(\tau_p \Omega_{PM}\right)^2 > 1$

  The solution is given by

$$\Delta T(T) = R \exp\left(-\frac{T}{2\tau_p}\right)\cos\left(\mu T - \delta\right) \tag{4.17}$$

where

$$R = \Delta T_0 \sqrt{\frac{4\left(\tau_p \Omega_{PM}\right)^2}{4\left(\tau_p \Omega_{PM}\right)^2 - 1}} \tag{4.18}$$

$$\mu = \frac{1}{2\tau_p}\left(\sqrt{4\left(\tau_p \Omega_{PM}\right)^2 - 1}\right) \tag{4.19}$$

$$\delta = \arctan\left(\frac{1}{\sqrt{4\left(\tau_p \Omega_{PM}\right)^2 - 1}}\right) \tag{4.20}$$

Equation (4.17) is that of an oscillating, decaying sinusoid whose envelope of decay is given by τ_p with natural oscillation frequency μ. This is the underdamped solution. For the case where the oscillation term is much stronger than the damping term such that $4\left(\tau_p \Omega_{PM}\right)^2 \gg 1$, then equation (4.17) simplifies to

$$\Delta T(T) = \Delta T_0 \exp\left(-\frac{T}{2\tau_p}\right) \cos\left[\Omega_{PM} T - \arctan\left(\frac{1}{2\left(\tau_p \Omega_{PM}\right)}\right)\right] \tag{4.21}$$

and the oscillation frequency simplifies to Ω_{PM}.

- **Case 2** *Overdamped:* $4\left(\tau_p \Omega_{PM}\right)^2 < 1$

This is the overdamped solution, given by a sum of decaying exponentials

$$\Delta T(T) = A \exp\left(-r_1 T\right) + B \exp\left(-r_2 T\right) \tag{4.22}$$

where the exponential decay terms r_1 and r_2 are

$$r_{1,2} = -\frac{1}{2\tau_p}\left(1 \pm \sqrt{1 - 4\left(\tau_p \Omega_{PM}\right)^2}\right) \tag{4.23}$$

and the constants A and B are

$$A = \Delta T_0 \left(\frac{-r_2}{r_1 - r_2}\right) \tag{4.24}$$

$$B = \Delta T_0 \frac{r_1}{r_1 - r_2} \tag{4.25}$$

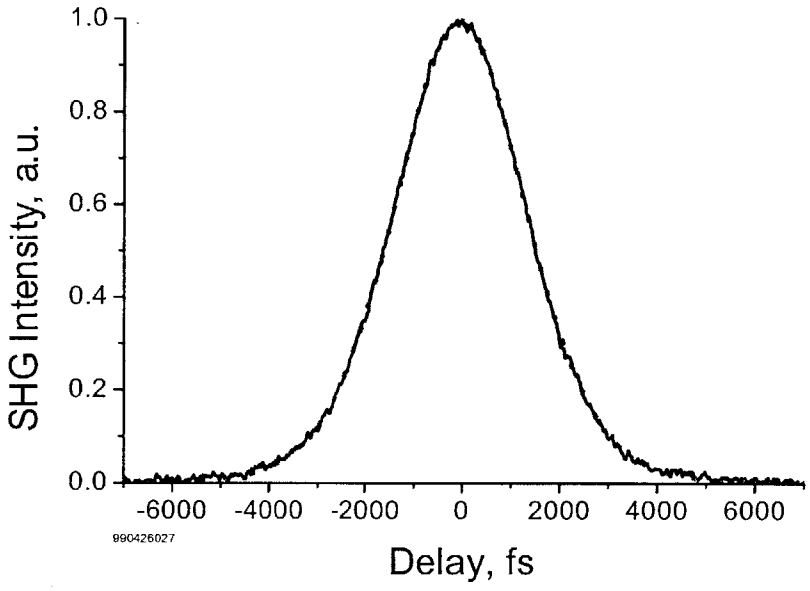

Figure 4-12: Autocorrelation trace for the case of phase modulation. The fit (dotted line) assumes a secant hyperbolic pulse shape with a full-width-at-half-maximum pulse width of 2.06 ps.

For the case where $4\left(\tau_p \Omega_{PM}\right)^2 \ll 1$,

$$\Delta T(T) = A \exp\left(-T/\tau_p\right) + \Delta T_0$$

- **Case 3** *Critically damped:* $4\left(\tau_p \Omega_{PM}\right)^2 = 1$

The motion of the pulse is critically damped and is given by

$$\Delta T(T) = \Delta T_0 \left(1 + \frac{1}{2\tau_p} T\right) \exp\left(-T/2\tau_p\right) \tag{4.26}$$

The pulses generated using phase modulation are almost identical with those generated using amplitude modulation–slightly longer (typically by 10-20% depending on the depth of modulation) but having the hyperbolic secant shape, as shown in Fig. 4-12. The optical and RF spectra were similar to that of AM.

The experiments for PM proceed in an identical fashion as for AM. At $t = 0$, an instantaneous "kick" is applied to the phase of the 10 GHz LO signal, equivalent to shifting the position of the pulse by an amount ΔT relative to the LO modulation. By monitoring the output IF mixer voltage on an oscilloscope, we can directly observe the dynamics of the pulse as it relaxes to its equilibrium position. A typical set of traces are shown in Fig. 4-13. The two traces correspond to different settings of modulation depth. For the lower trace, the pulse oscillates about its equilibrium position and is quickly damped out in a few oscillations–this is the character of an underdamped response. The dashed curve is a two-parameter fit to find the damping, τ_p, and natural oscillation frequency, Ω_{PM}. The value of the product $4\left(\tau_p\Omega_{PM}\right)^2$ is 8.63, consistent with the behavior of an underdamped harmonic oscillator. By decreasing the modulation depth–thus reducing the damping–the retiming resembles that of a critically damped harmonic oscillator as shown in the figure with a dash-dotted curve. For the extracted parameters τ_p and Ω_{PM}, the product $4(\tau_p\Omega_{PM})^2$ is 1.16 and very close to critical damping, as expected.

Just as for the case of AM, the fluctuations of the average power during the switching event was also monitored–an example trace is given in Fig. 4-14 for the case where the response is close to critical damping $\left[4\left(\tau_p\Omega_{PM}\right)^2 = 1.26\right]$. After the switching event for which the phase was shifted by 0.11π (approximately 5.5 ps) at $t = 0$, the power oscillated with a peak fluctuation of $\sim$2 percent and was damped out in $\sim$80 μs with an oscillation frequency of $\sim$20 kHz.

A variety of similar retiming curves were generated after varying the pump power and modulation depth, and for each curve the data was fit using a two-parameter fit to extract τ_p and Ω_{PM}. The resulting data and the comparison with the theory for τ_p and Ω_{PM} are given in Figs. 4-15 and 4-16 and again, just as for the case of τ_{AM}, show good agreement.

4.5 Conclusion

In this chapter, we briefly reviewed the equations of motion that govern the retiming of a soliton under the influence of a driving noise source for the cases of amplitude and phase modulation and identified the characteristic time constants. We demonstrated an apparatus that can directly

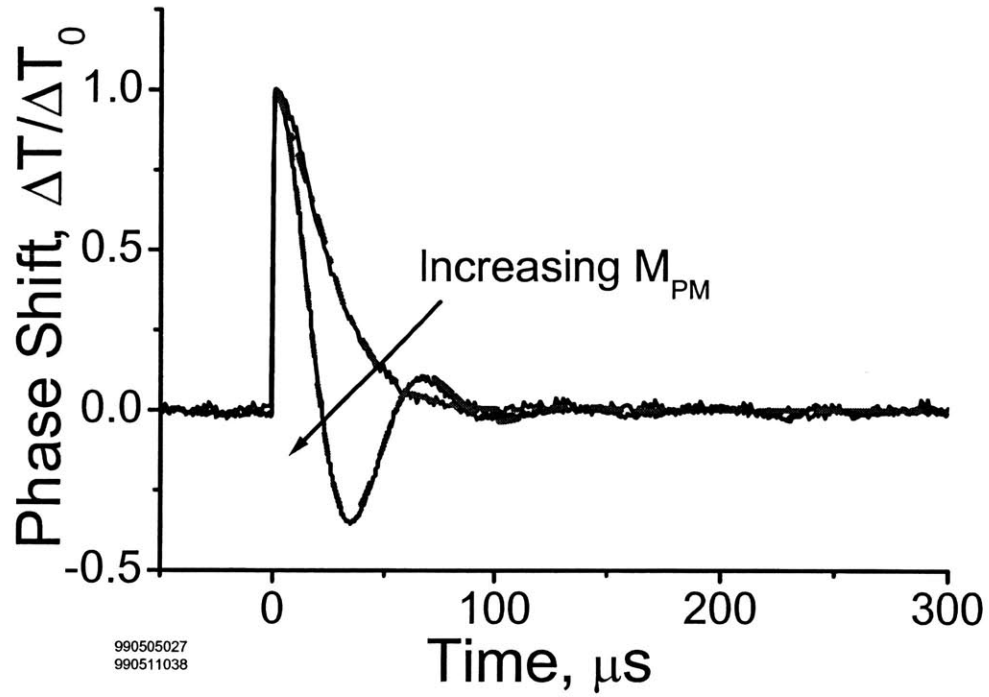

Figure 4-13: Retiming dynamics for the case of PM for two different modulation depths. Solid dark curve, data; dashed and dashed-dotted curves, fit to second-order exponentials.

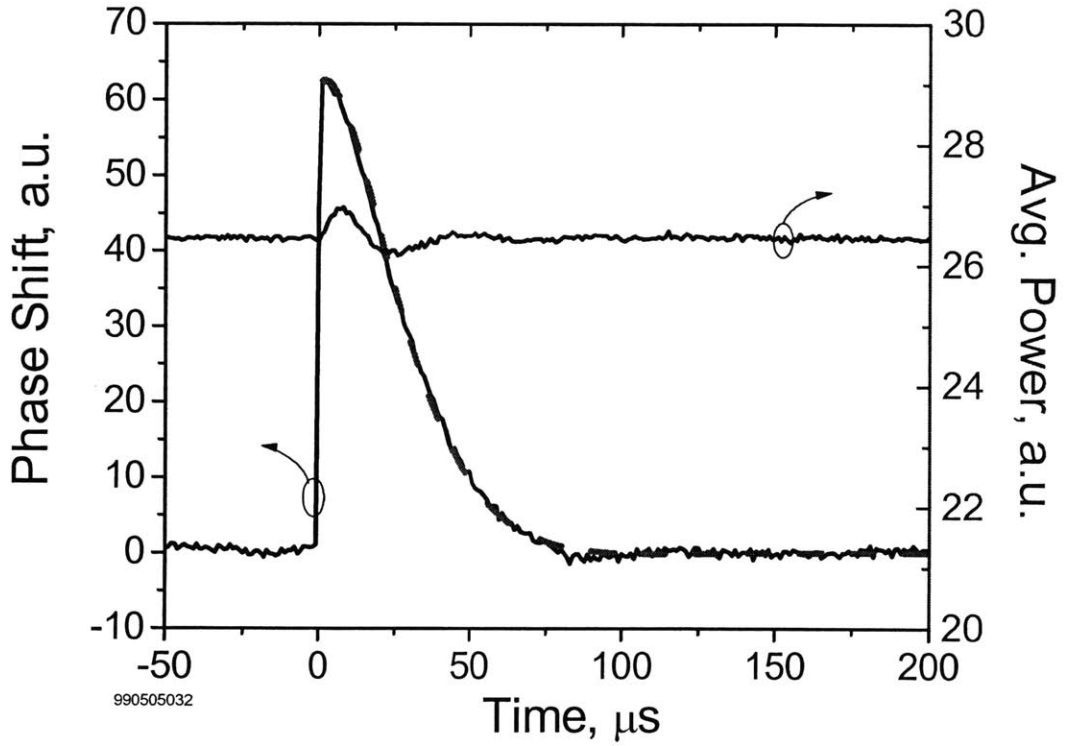

Figure 4-14: Dynamic timing recovery for the case of PM (solid and dashed curve) and measurement of amplitude perturbations via direct detection of the laser pulses with a slow detector. The power oscillation corresponds toa relaxation oscillation frequency of $\sim$ 31 kHz.

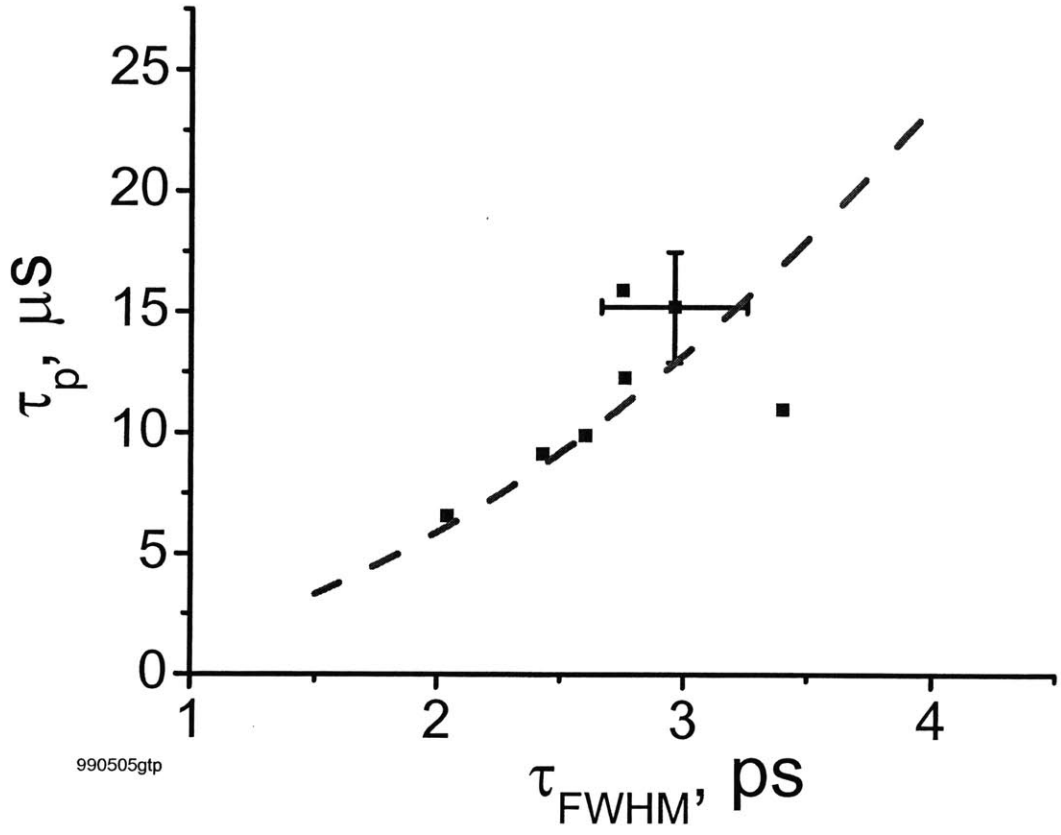

Figure 4-15: Plot of the filtering constant as a function of pulse width (for fixed filter bandwidth). Squares, experimental data; dashed line, theory. Error bars for the data set are shown on one of the data points.

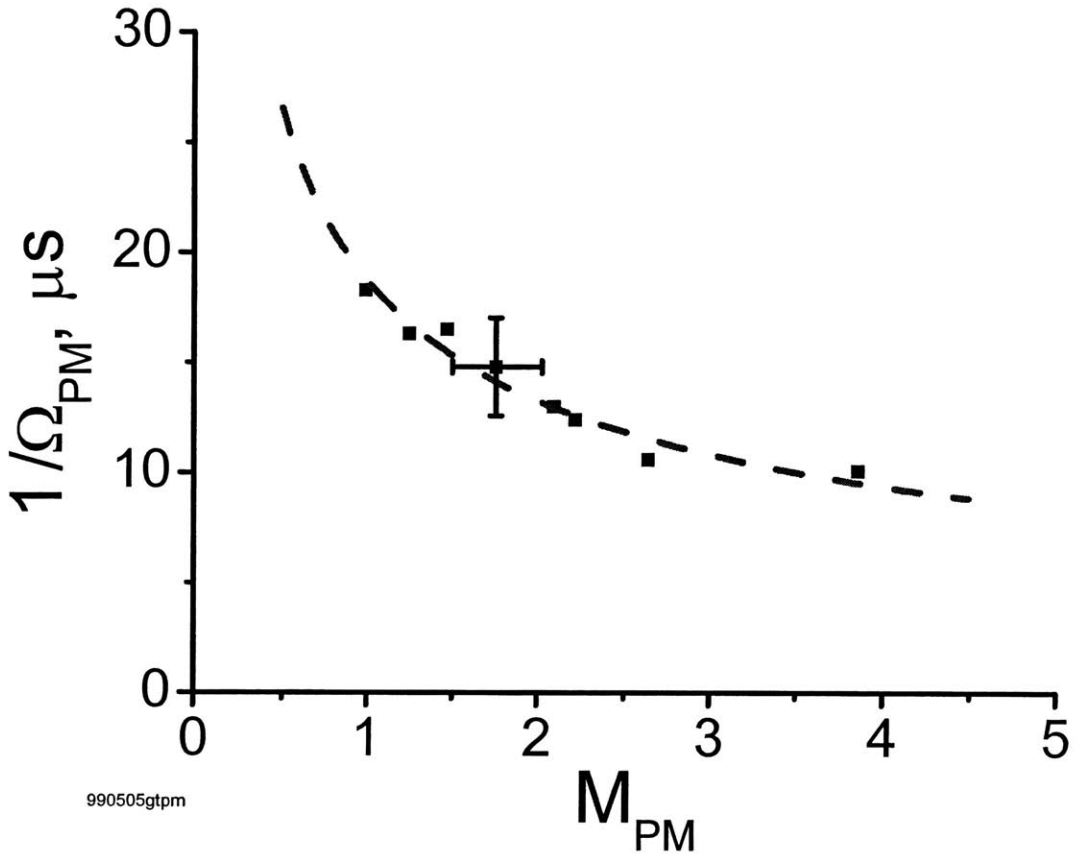

Figure 4-16: Plot of the characteristic constant Ω_{PM} as a function of modulation depth. Squares, experimental data; dashed line, theory. Error bars for the data set are shown on one of the data points.

measure the characteristic constants and compared them with theory, with good agreement.

4.6 Experimental Notes and Ideas for Future Work

Using a modulator that allows both modulation ports to be driven based on external bias circuitry allows for the simultaneous use of both amplitude and phase modulation. The equations of motion resulting from this kind of modulation reveals a damped harmonic oscillator with added damping. The left-hand side of equation 4.14 is given by

$$\frac{d^2}{dT^2}\Delta T + \frac{1}{\tau_p'}\frac{d}{dT}\Delta T + \Omega_{PM}'\Delta T \tag{4.27}$$

where

$$\frac{1}{\tau_p'} = \frac{1}{\tau_p} + \frac{1}{\tau_{AM}} \tag{4.28}$$

$$\Omega_{PM}^{2\prime} = \Omega_{PM}^2 + \frac{1}{\tau_{AM}\tau_p} \tag{4.29}$$

It would be interesting to measure this enhanced damping directly and if there is an optimum way of distributing the RF power between amplitude and phase modulation to achieve the minimum timing jitter.

The time constants measured in these experiments stemmed from the perturbation of the position of the pulse. It would interesting to study the time constants when driven by a perturbation of the pulse carrier frequency to allow for a more direct measure of τ_p and Ω_{PM}.

Modelocking an actively modelocked laser requires the adjustment of a number of parameters for optimum performance, including bias voltage, modulation depth, and detuning between the external reference oscillator and cavity length. The locking circuit constructed for these experiments is designed such that it will reduce the error voltage associated with drift between the external reference oscillator and the cavity harmonics. To initially match the external reference oscillator (LO) and one of the cavity harmonics requires one to either tune the LO or the length of the cavity. Optimum modelocking is determined by monitoring the RF spectrum as well as the optical spectrum. Once this is done, the bias of the phase detector must be manually adjusted to zero by tuning the phase delay from one of the arms of the phase

detection circuit, and then the control circuit is switched on. If one makes an error in the manual adjustment by not biasing the error voltage exactly at zero, turning on the circuit will result in a pulling of the cavity length away from the optimum position. Using regenerative modelocking with an external LO reference is capable of generating true phase-locked loop action and can automatically reduced the relative difference between the LO and the cavity.

It was useful to monitor the autocorrelation traces in real time using a swept delay line (standard speaker drive is sufficient for picosecond pulses). If one used the retiming traces as a measure of optimum modelocking by setting the laser parameters (i.e., bias voltage setting, cavity detuning, modulation depth) to achieve the fastest time constants, it would often be found that the autocorrelation scans revealed large amounts of continuum (sometimes as much as 10%-50% of the power would be in the background compared to the pulse). It was difficult to study these effects systematically, as often they were observed in a quasi-stable state.

Chapter 5

Timing Jitter Measurements

5.1 Introduction

[1]In chapter 3, we derived a theory for the quantum-limited timing jitter for actively modelocked lasers. We found characteristic time constants that describe how the laser responds to noise that leads to timing jitter, and in chapter 4 we experimentally verified the dependencies of the time constants on the laser parameters. In this chapter, we present experimental evidence of quantum-limited jitter in an active harmonically modelocked soliton fiber laser for both AM and PM and compare them to theory. We find experimentally that the spectrum of the timing jitter for harmonic modelocking is an aliased version of that for active modelocking, consistent with the case for which the pulse-to-pulse timing jitter within one round-trip time is uncorrelated. A comprehensive theory for the case of harmonic modelocking is presented in chapter 6.

5.2 Theory

A comprehensive theory of timing jitter in actively modelocked soliton lasers has been presented in chapter 3 and in Ref [36], and the key results are given here. The master equation describes the evolution of the amplitude envelope of the electromagnetic field of a laser pulse[27][32][36][43]

[1]The work in this section was accomplished in collaboration with Leaf Jiang, Jeff Hargreaves, and Paul Juodawlkis. Jesse Searls and Cameron McNeilage provided invaluable assistence and loan of the ultrastable oscillator, and Farhan Rana provided many insightful discussions. Kim Trapp donated the 18 GHz $LiNbO_3$ modulator, Bob Windeler provided the double-clad Er:Yb fiber, Harry Lee loaned a high-speed preamplifier, Kazi Abedin provided a fiber-wrapped PZT, and Robert R. Kerr loaned an ultrastable oscillator.

and the action of linear gain and loss, filtering, group-velocity dispersion (GVD), self-phase modulation, and active modelocking with both amplitude (AM) and phase (PM) modulation. The equation is driven by ASE noise. To treat the resulting laser noise, the master equation is linearized around a soliton solution to produce a set of ordinary differential equations with constant coefficients. These coefficients determine how the laser pulses are affected by the ASE[46]. We found previously that the power spectrum of the timing fluctuations can be solved and written as

$$\left\langle |\Delta T(\Omega)|^2 \right\rangle = \frac{\frac{1}{\tau_p'^2} + \Omega^2}{\Omega^4 + \left(\frac{1}{\tau_p'^2} - 2\Omega_{PM}'^2\right)\Omega^2 + \Omega_{PM}'^4} * \left[\left(\frac{2D}{T_R}\right)^2 \frac{D_{pp}}{\frac{1}{\tau_p'^2} + \Omega^2} + D_{TT}\right] \tag{5.1}$$

where ΔT is the deviation of the pulse timing measured from the average pulse position, and the brackets $\langle\rangle$ denote time or sample averaging. Ω is the offset frequency measured from the laser repetition rate in radians/s, T_R is the round-trip time, and D the group-velocity dispersion (GVD). D_{TT} and D_{pp} are diffusion constants determined by the ASE[43] and are given as $D_{TT} = 2\pi^2\tau^2 g\theta h\nu/(3w_0 T_R)$ and $D_{pp} = 4g\theta h\nu/(3w_0\tau^2 T_R)$ where g is the gain per pass, θ is the gain-inversion factor, h Planck's constant, ν the optical carrier frequency, τ the soliton pulse width, and w_0 the pulse energy. From equation (5.1), the spectrum is determined by characteristic coefficients[46], given as

$$1/\tau_p' = 1/\tau_p + 1/\tau_{AM} \tag{5.2}$$

$$\Omega_{PM}'^2 = \Omega_{PM}^2 + 1/(\tau_p\tau_{AM}) \tag{5.3}$$

where

$$\frac{1}{\tau_{AM}} = \frac{\pi^2}{6} M_{AM}\omega_m^2\tau^2\frac{1}{T_R}$$

$$\frac{1}{\tau_p} = \frac{4}{3\Omega_f^2\tau^2}\frac{1}{T_R}$$

$$\Omega_{PM} = \sqrt{2DM_{PM}\omega_m^2}/T_R$$

Laser Parameters	Value
g	10
D	0.1 ps^2
Ω_f	10 nm
w_0	7.6 pJ
τ	1.05 ps
T_R	483 kHz
$1/\tau_\nu^{'}$	42×10^3 rad/s
$\Omega_{PM}^{'}$	22×10^3 rad/s

Table 5.1: Parameters used for theoretically-determined single-sideband timing jitter spectrum for the case of AM.

As defined previously, Ω_f is the optical filtering bandwidth, M_{AM} and M_{PM} are the modulation depths for AM and PM, respectively, and ω_m the modulation frequency in radians/s. Here, we have allowed for simultaneous AM and PM action. The spectrum of the jitter given in (5.1) is similar to that of a driven damped harmonic oscillator (but with important differences, as discussed in section 3.3). The effect of AM is to restore the pulse timing with time constant τ_{AM} and is reduced for long pulses, large modulation depth, and shorter laser cavities. The effect of PM is to impart frequency shifts Ω_{PM} that are translated into retiming via GVD and is enhanced for large modulation depth and large GVD. However, while GVD helps to restore the pulse timing using PM, GVD also increases the Gordon-Haus jitter[66] (in which ASE-induced frequency shifts are converted to timing shifts via GVD). Thus, there is an optimum GVD that minimizes the overall jitter[36] for the case of PM. Strong spectral filtering (small τ_p) limits the frequency shifts. Using AM and PM simultaneously leads to an enhancement of the imparted frequency shifts (Ω'_{PM}) and stronger filtering (τ'_p). The relative strength of the product $4(\Omega'_{PM}\tau'_p)^2$ governs the characteristic spectrum of the jitter and can vary from underdamped (product is greater than one) to overdamped (product is less than one)[36][37].

The spectrum of the jitter (given in units for single-sideband phase-noise measurement) is given in Fig. 5-1 for a set of typical laser parameters given in Table 5.1. The modulation was

set for predominantly AM operation, thus we can simplify equation (5.1) to

$$\left\langle |\Delta T(\Omega)|^2 \right\rangle \simeq \frac{1}{\Omega^2 + \frac{1}{\tau_{AM}^2}} \left[\left(\frac{2D}{T_R} \right)^2 \frac{D_{pp}}{\Omega^2 + \frac{1}{\tau_p^2}} + D_{TT} \right] \tag{5.4}$$

$$\simeq \frac{D_{TT}}{\Omega^2 + \frac{1}{\tau_{AM}^2}} \left[\frac{\Omega^2 + \left(\frac{1}{\tau_p^2} + \left(\frac{2D}{T_R} \right)^2 \frac{D_{pp}}{D_{TT}} \right)}{\Omega^2 + \frac{1}{\tau_p^2}} \right] \tag{5.5}$$

where we have written the equation in a form suitable for Bode-plot type of analysis and identification of the turning points in the spectrum. The spectrum is flat from $\Omega = 0$ until the frequency encountered at $\Omega = 1/\tau_{AM}$ after which the the spectrum falls off by 20 dB per decade (dB/dec)–this reflects the fact that the action of amplitude modulation restricts the random-walk behavior at frequencies up to $1/\tau_{AM}$ due the ability of the modulator to retime pulses. The next turning point occurs at $1/\tau_p$ after which the spectrum falls off at 40 dB/dec and is due to the strength of filtering that reduces the Gordon-Haus jitter that is caused by random fluctuations of the carrier frequency that translate into timing fluctuations via GVD. Increasing the filtering strength reduces the amount of frequency deviation. The frequency in the numerator occurs at

$$\Omega_{pull} = \sqrt{\frac{1}{\tau_p^2} + \left(\frac{2D}{T_R} \right)^2 \frac{D_{pp}}{D_{TT}}} \tag{5.6}$$

after which the spectrum is pulled up to 20 dB/dec, and Ω_{pull} depends on the magnitude of the noise sources due to carrier frequency shifts D_{pp} and timing shifts D_{TT}–this noise-dependent frequency is not encountered in the typical equation of motion for the position of a particle trapped in a potential well and comes about because of the Gordon-Haus effect. As GVD approaches zero, Ω_{pull} approaches $1/\tau_p$, and the spectrum of the jitter is reduced to a simple Lorentzian of the form

$$\left\langle |\Delta T(\Omega)|^2 \right\rangle \simeq \frac{D_{TT}}{\Omega^2 + \frac{1}{\tau_{AM}^2}} \tag{5.7}$$

and the carrier frequency noise D_{pp} does not couple to the timing jitter.

The features at harmonics of the round-trip frequency of 483 kHz are the supermodes of the cavity. The spectrum of the supermodes reveal information about pulse-to-pulse correlations[71]. For the case where the pulses are uncorrelated, the spectra of the super-

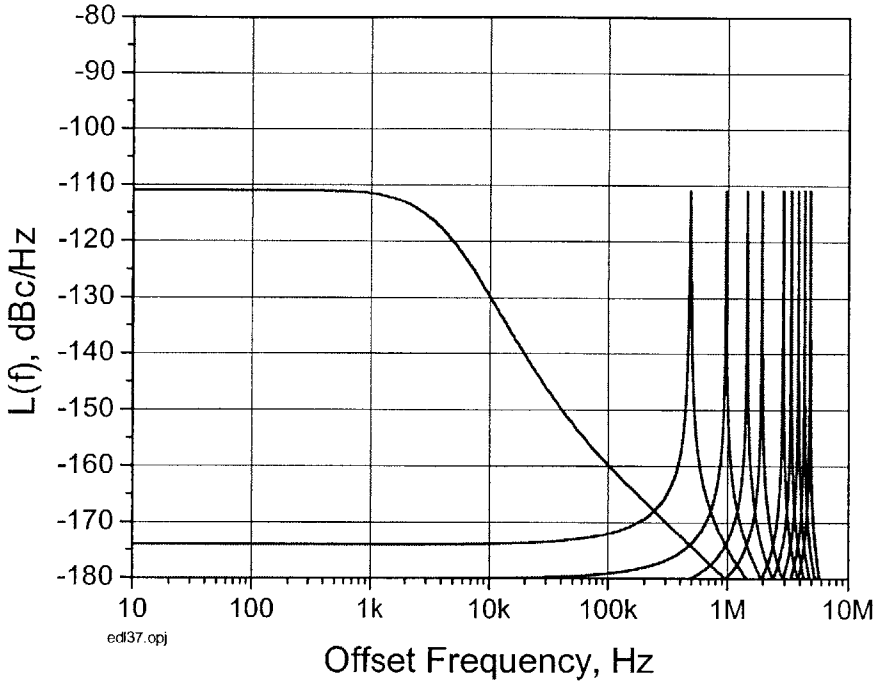

Figure 5-1: Theoretical single-sideband curve for the harmonically modelocked laser with parameters given in Table 5.1 for the case of AM assuming that the pulse-to-pulse timing jitter is uncorrelated.

modes are identical to that of the spectrum at the harmonically-modelocked repetition rate and discussed in more detail below and in chapter 6. The spectra of the supermodes appear to be compressed compared to the spectrum at baseband, but this is due to the log-log plot.

Table 5.2 gives another set of typical laser parameters for the case where the modulation is mostly PM, and the theoretical spectrum of the jitter is given in Fig. 5-2. Again, the spectrum at low frequency offsets is flat–the action of phase modulation limits the random walk of the pulse position. The physics underlying retiming for phase modulation is that pulses arriving at the wrong time compared to the LO are frequency shifted by the phase modulator by an amount depending on the slope of the phase modulation, given by the square root of the product of the modulation depth and the square of the repetition rate (for a sinusoidal driving frequency). The frequency shift is translated to timing jitter via GVD. Optical filtering limits

Laser Parameters	Value
g	10
D	0.1 ps^2
Ω_f	10 nm
w_0	7.6 pJ
τ	1.05 ps
T_R	483 kHz
$1/\tau_\nu^{'}$	24×10^3 rad/s
$\Omega_{PM}^{'}$	32×10^3 rad/s

Table 5.2: Parameters used for theoretically-determined single-sideband timing jitter spectrum for the case of PM and underdamping.

the amount of frequency shift and damps the pulse retiming, leading to characteristic retiming that can be overdamped, underdamped, or critically damped. The peaking in Fig. 5-2 indicates underdamped retiming.

5.3 Sigma Fiber Laser

The actively modelocked fiber laser used for our experiments shown in Fig. 5-3 is similar to that previously described[45]. The dual-drive lithium-niobate modulator (Lucent x2624, 18 GHz bandwidth) can be configured for any combination of AM and PM. The gain is provided by a double-clad Er:Yb optical amplifier side-pumped at 980 nm. The GVD is 1.1 ps/nm/km (anomalous). A phase-locked loop (PLL)–using a fiber-wound piezo-electric cylinder and an integrating, amplifying control circuit–is used to stabilize the cavity length fluctuations[72]. The ring portion of the laser consists of all polarization-maintaining fiber and devices with polarization-maintaining fiber pigtails. The linear portion of the cavity consists of non-polarization-maintaining fiber.

The sigma geometry allows for a laser cavity whose operation is similar to that of a polarization ring cavity in that it is stable in the presence of environmental perturbations. The principle of operation of the laser is as follows: pulses exiting the PBS from the ring in the clockwise direction enter the linear portion of the cavity traveling to the right and are linearly polarized. Upon passage through the long lengths of fiber in the linear portion, the polarization

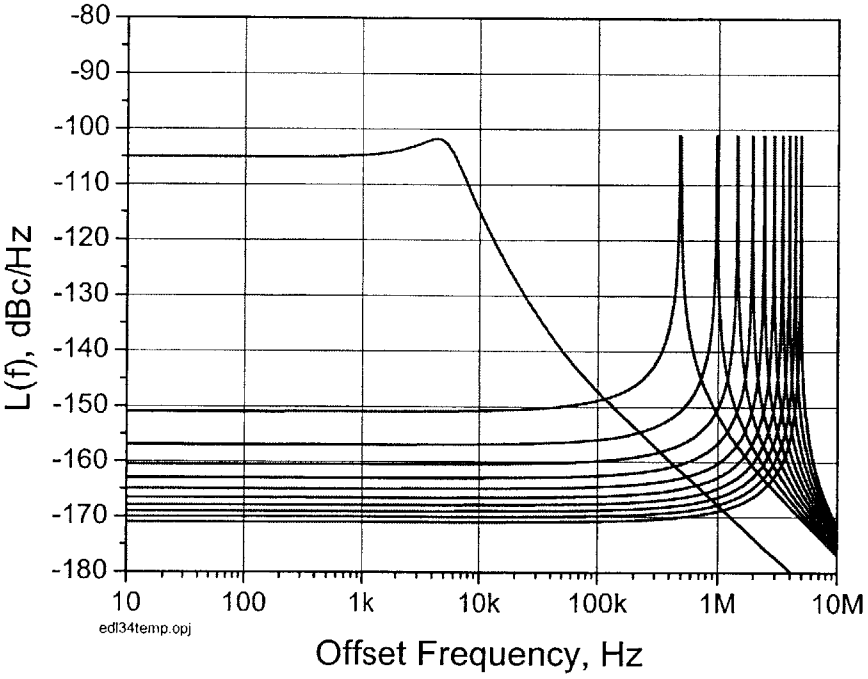

Figure 5-2: Theoretical single-sideband curve for the harmonically modelocked laser with parameters given in Table 5.2 for the case of PM (underdamped case) assuming that the pulse-to-pulse timing jitter is uncorrelated.

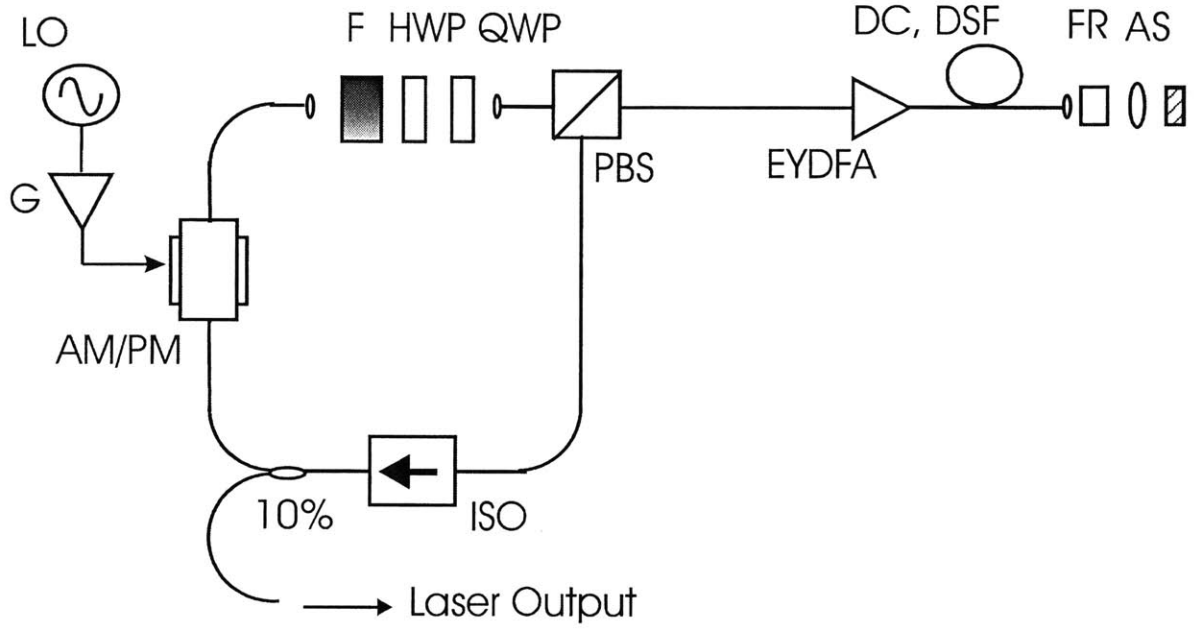

Figure 5-3: Actively modelocked sigma fiber laser setup for amplitude and phase modulation. ISO isolator, PBS polarizing beam splitter, HWP and QWP half- and quarter-wave plate, F optical filter (10 nm), EYDFA erbium/ytterbium-doped amplifier, DSF and DCF dispersion-shifted (110 m) and dispersion-compensating (13.3 m) fiber, FR Faraday rotator, AS aspheric lens, LO local oscillator, and G is an RF power amplifier.

evolves into a general elliptical state due to birefringence. After making two passes through the faraday rotator, the major and minor axes of the elliptical polarization are switched, and the polarization state of the pulse entering the PBS from the linear portion of the ring and traveling to the left is linear and orthogonal compared to the signal leaving the PBS, and thus is switched down into the ring in the clockwise direction. The linear portion of the cavity is subject to environmental drift over time, which will alter the polarization state of the laser pulse. Because the time scale of environmental drift is on the order of ms, the pulses experience a constant birefringence (transit time of the laser pulse through the linear portion of the ring is on the order of microseconds), and the Faraday rotation ensures that the pulses travels along both virtual birefringent axes. The primary advantage of the sigma laser design is that it allows for the use of non-polarization maintaining fiber components without sacrificing the stability of an all polarization-maintaining fiber ring laser design.

The gain is provided by a 15.5 m length of co-doped erbium-ytterbium in a silica host (Lucent Technologies) with a 0.45-N.A. polymer outer cladding, a nearly hexagonal 131-mm inner cladding, a 6-mm-diameter core with a N.A. of 0.16, and an absorption of 2.2 dB/m at 975 nm. The fiber was side-pumped with a 975-nm, 2-W (at 3.0 A) broad stripe diode (SDL, Inc.) by a V-groove pump coupling technique[73][74] with pump light counterpropagating relative to the signal. The double-cladding fiber's ends were fusion spliced to TruWave (Lucent Technologies) single-mode fiber pigtails. Typical small-signal gain for the amplifier is shown in Fig. 5-4 and typically ~30 dB. The spectrum of the gain is slightly red-shifted compared to erbium-doped silica fiber. As shown in Fig. 5-5, the spectrum of the gain is blue shifted as the pump current is increased.

The laser produced transform-limited pulses (hyperbolic secant shape) at 9.00 GHz (the 18,634th harmonic of the 483 kHz fundamental cavity repetition rate) with pulse widths between 1.5 and 3.5 picoseconds at 1558 nm with typically ~75 dB of supermode suppression and up to 10 mW output power. A typical autocorrelation trace (non-colinear, background-free in a 2 mm POM crystal) is shown in Figs. 5-6, with the dotted line a fit to a hyperbolic secant. Figure 5-7 shows the RF spectrum of the directly detected photocurrent with $>$ 75 dB of supermode suppression.

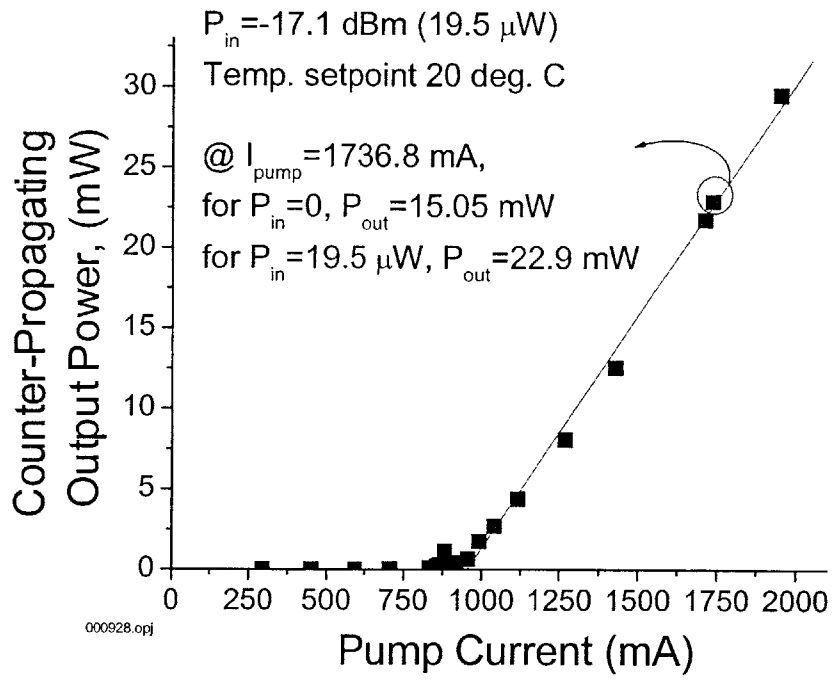

Figure 5-4: Counter-propagating gain for the 15.5 m Erbium-Ytterbium fiber pumped with a single multimode edge-emitting laser diode at 975 nm.

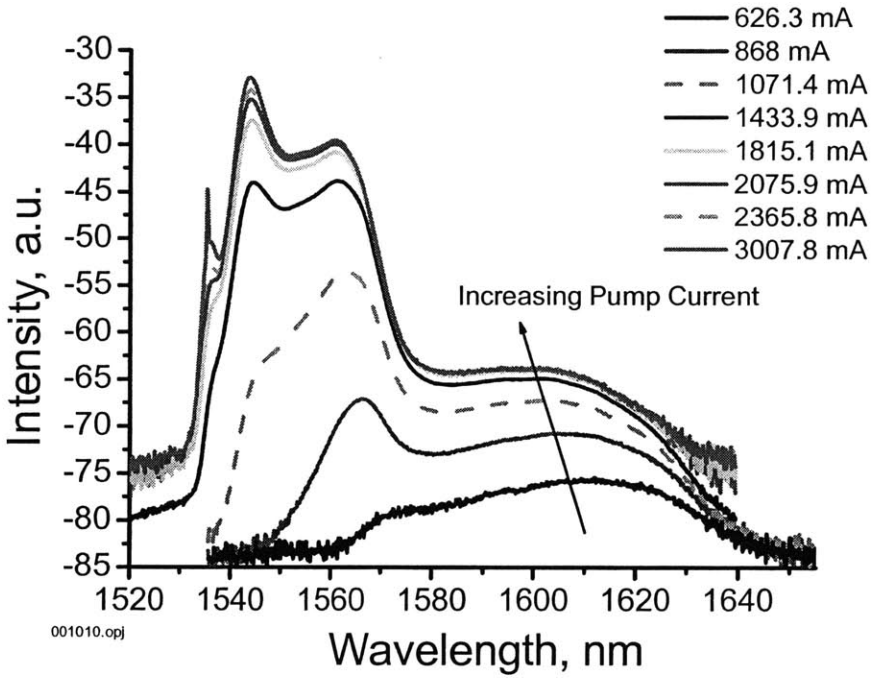

Figure 5-5: Spontaneous emission spectrum of the erbium-ytterbium double-clad amplifier side-pumped at 975 nm from a single mulitimode laser diode in a counterpropagating geometry as a function of pump current. The pump diode was temperature stabilized at 20.0 C.

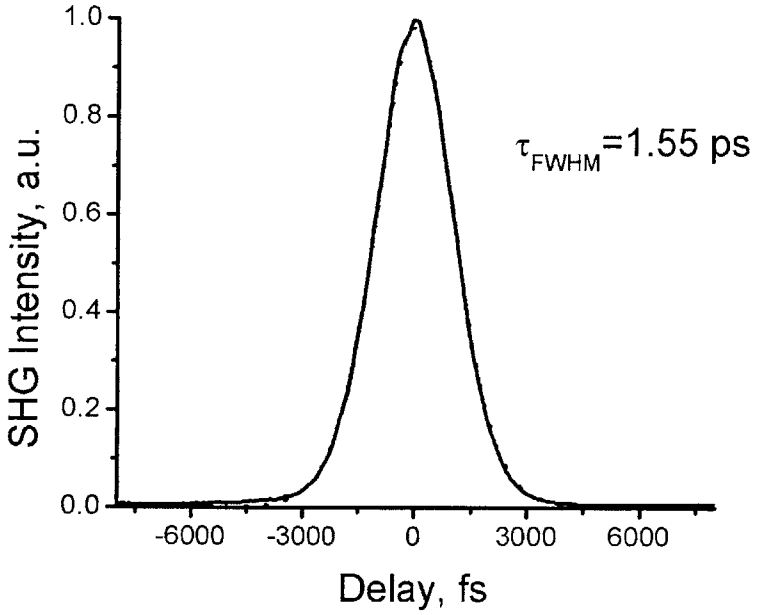

Figure 5-6: Autocorrelation trace of the intensity of the second-harmonic as a function of pulse delay. Dotted curve is a fit to a secant hyperbolic pulse shape with a full-width-at-half-maximum pulse width of 1.55 ps.

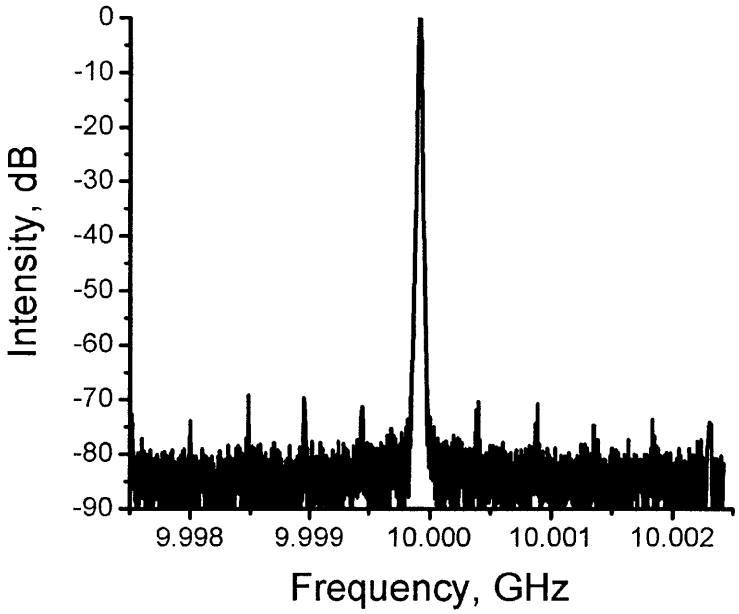

Figure 5-7: RF spectrum of the directly detected photogenerated current; supermode suppression > 70 dB.

5.4 Timing Jitter Measurement Scheme

There are a number of techniques for measuring timing jitter. Von der Linde proposed using direct detection and a large bandwidth RF spectrum analyzer to measure timing (and amplitude) jitter [75]. Optical cross correlation has also been used[76][77]. Another method relies on the rapid scanning of two lasers but at slightly different repetition rates with optical cross-correlation[78][79]. Phase-encoded optical sampling has also been shown to measure timing jitter while achieving large rejection of amplitude noise[18]. The phase-detector method is a technique often used in the measurement of ultrastable microwave clocks and oscillators[80][81][82] and has been shown to be useful for timing jitter measurements[9][10][55][57][83][84] and is the technique used for measurements here.

The phase detector method requires that the laser pulse train be converted into a sinusoidal waveform after photodetection by low-pass filtering of the harmonics of the repetition rate. The timing jitter of the optical pulses is then converted to phase noise of the sinusoidal carrier frequency at the laser repetition rate. To extract the phase noise from the carrier frequency, the carrier signal is beat against a low-noise RF local oscillator (LO) with homodyne RF detection, thus downconverting the phase noise on the sinusoidal carrier frequency to baseband. At baseband, we can use sophisticated electronic processing of the signal with high performance digital electronics not available at the RF carrier frequency. Also, by removing the carrier frequency, we can achieve very high dynamic range in our measurements of the noise. A good review article on using the phase-detector method for measuring timing jitter is given in Ref. [85].

With a phase-locked loop maintaining quadrature between a local oscillator and the laser repetition rate, the mixer output voltage is proportional to the difference between the LO and phase (timing) of the laser pulse train:

$$\begin{aligned} V_{out}(t) &= 2k_\phi V_L(t) V_{LO}(t) \\ &= k_\phi \sin\left[\omega_L t + \phi(t)\right] \cos(\omega_{LO} t) \\ &= k_\phi \sin\left[2\omega_L t + \phi(t)\right] + k_\phi \sin\left[\phi(t)\right] \end{aligned} \tag{5.8}$$

where the RF frequency of the LO and laser–ω_{LO} and ω_L, respectively–are the same (and phase

locked). Quadrature detection using a double-balanced mixer suppresses the effects of the laser amplitude fluctuations by ~10-15 dB. The high frequency component at $2\omega_L$ is filtered out, and for the case where $\phi(t) \ll 1$,

$$V_{out}(t) \simeq k_\phi \phi(t) \quad \text{for } \phi(t) \ll 1 \tag{5.9}$$

where k_ϕ is a calibration term for the mixer (measured in V/radian) and depends on the mixer technology, LO average power, and average RF power, given by

$$k_\phi = \alpha \frac{V_{LO} V_L}{2} \tag{5.10}$$

where α is the mixer conversion constant. For a typical level-7 mixer with LO power +7 dBm and RF power +6 dBm, k_ϕ is ~0.25 V/rad.

The frequency spectrum of the mixer output that is directly measured on the FFT analyzer is the spectrum of the voltage, from (5.9)

$$S_\phi(f) = \left(\frac{V_{out}(f)}{k_\phi} \right)^2 \tag{5.11}$$

measured in rad^2/Hz. Typically, the spectrum of the phase noise is referred to the equivalent noise that would result if an oscillator with phase noise $S_\phi(f)$ were phase-modulating a carrier wave[86]. If $S_\phi(f)$ is small, then sidebands develop close to the carrier, and the spectrum of one of the sidebands is given as

$$L(f) = S_\phi(f)/2 \tag{5.12}$$

where $L(f)$ is measured in dBc/Hz and referred to as the single-sideband phase noise. $S_\phi(f)$ is related to the spectrum of the timing jitter $S_{tt}(f)$

$$S_\phi(f) = (2\pi f_m)^2 S_{tt}(f) \tag{5.13}$$

where $f_m = \omega_m/2\pi$ is the laser repetition rate, and $S_{tt}(f)$ is the spectrum of the jitter for a train of pulses in units of s^2/Hz, derived in detail in chapter 6. In chapter 3, we had discussed the spectrum of the timing jitter after defining a variable ΔT for the position of

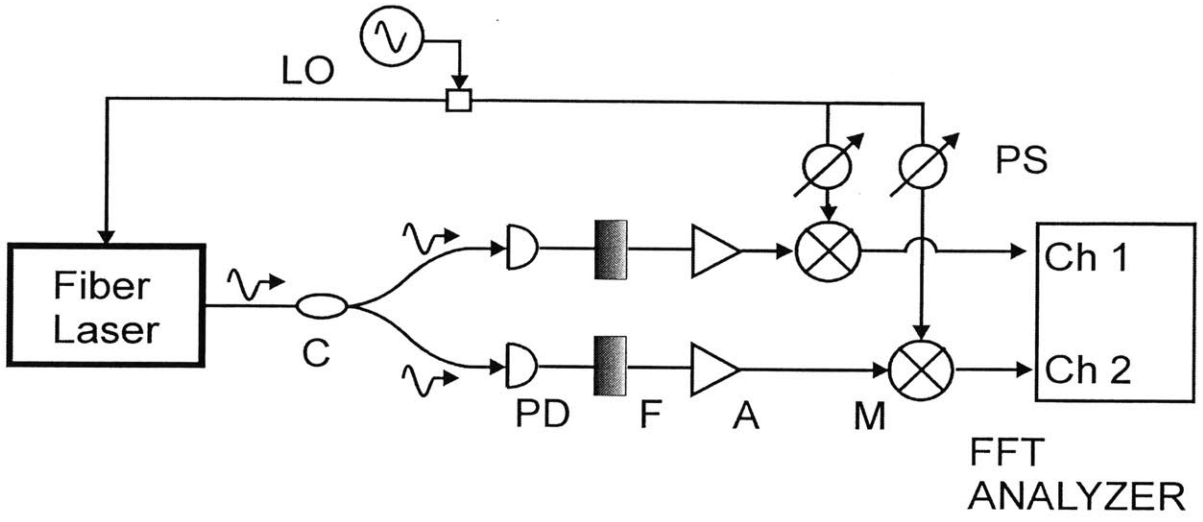

Figure 5-8: Dual-channel single-sideband phase-noise setup. C is a fiber-coupled 50/50 splitter, PD photodiode, F bandpass filter, A preamplifier, M double-balanced mixer, LO local oscillator, and PS phase shifter.

a single pulse, and the resulting equations of motion for ΔT did not include pulse-to-pulse correlations. For a fundamentally modelocked laser (or a harmonically modelocked laser whose pulses are strongly correlated), $S_{tt}(f) = \left\langle |\Delta T(f)|^2 \right\rangle$, and $L(f) = \frac{(2\pi f_m)^2}{2} \left\langle |\Delta T(f)|^2 \right\rangle$. For a harmonically modelocked laser whose fundamental cavity length is f_R and whose pulses are totally uncorrelated, $S_{tt}(f) = \Sigma_n \left\langle |\Delta T(f - nf_R)|^2 \right\rangle$ and $L(f) = \frac{(2\pi f_m)^2}{2} \Sigma_n \left\langle |\Delta T(f - nf_R)|^2 \right\rangle$. Again, these results are discussed in more detail in chapter 6.

The timing jitter measurement scheme is shown in Fig. 5-8. The laser pulses are split by a 50/50 coupler into two identical channels consisting of a fast photodetector (16 GHz bandwidth), amplifier (8-12 GHz bandwidth, N.F. 3.9), and double-balanced mixer. The generated photocurrent is lowpass filtered to eliminate harmonics at the repetition rate, leaving a sinusoid whose phase noise is determined by the timing jitter of the pulse train. This sinusoidal signal is amplified and input to the RF port of a double-balanced mixer. The LO is input into the LO port of the mixer after passing through an adjustable phase shifter. By using two channels, we can reduce the measurement noise floor and increase the sensitivity, as discussed below.

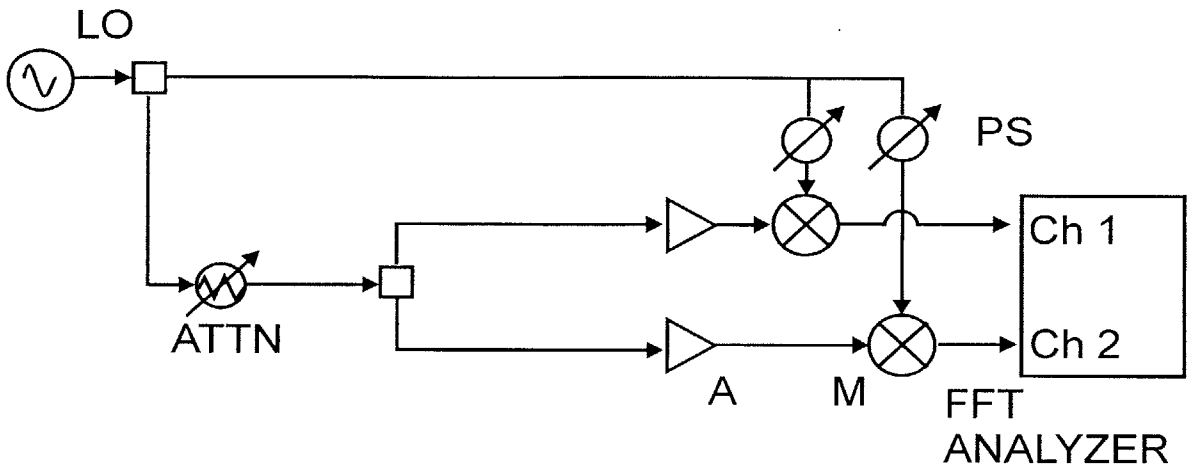

Figure 5-9: Dual-channal single-sideband setup for establishing the measurement phase noise floor. LO is a local oscillator, PS phase shifter, ATTN attenuator, A preamplifier, and M double-balanced mixer.

The measurement noise floor of the system is found by replacing the photodiodes and filter with an attenuated version of the LO, as shown in Fig. 5-9. The level of attenuation is set such that the output current after the attenuator is equivalent to the photocurrent generated after direct detection of the laser pulses. In this way, the noise floor reflects conditions of the measurement system closely resembling those during the experiment. The resulting noise floor is given in Fig. 5-10 and measured in dBc/Hz expressing the number of radians of deviation of the phase at the carrier frequency (here, at 9.00 GHz) per Hz of bandwidth. The phase noise is plotted in terms of offset frequency from the carrier frequency. The bandwidth of the FFT analyzer used here (HP 89410A) is from 0-10 MHz and can achieve frequency resolution bandwidths down to mHz. Each channel was independently calibrated for k_ϕ in order to convert the measured voltage on the FFT analyzer (in $V/\sqrt{Hz}$) into units of measured phase with respect to a carrier frequency (dBc/Hz), and the results are shown in Fig. 5-10. Each channel is matched to within 1 dB over the measurement range. The level of each channel's measurement noise suggests that the limiting factor is noise added by the preamplifiers: at 1 kHz offset, the single-sideband noise is ~-132 dBc/Hz. The noise floor of each channel is dominated by 1/f for $0 < f < 1$ kHz, and by $1/f^2$ for 1 kHz$< f <$ 10 kHz, and $1/f^3$ for 10

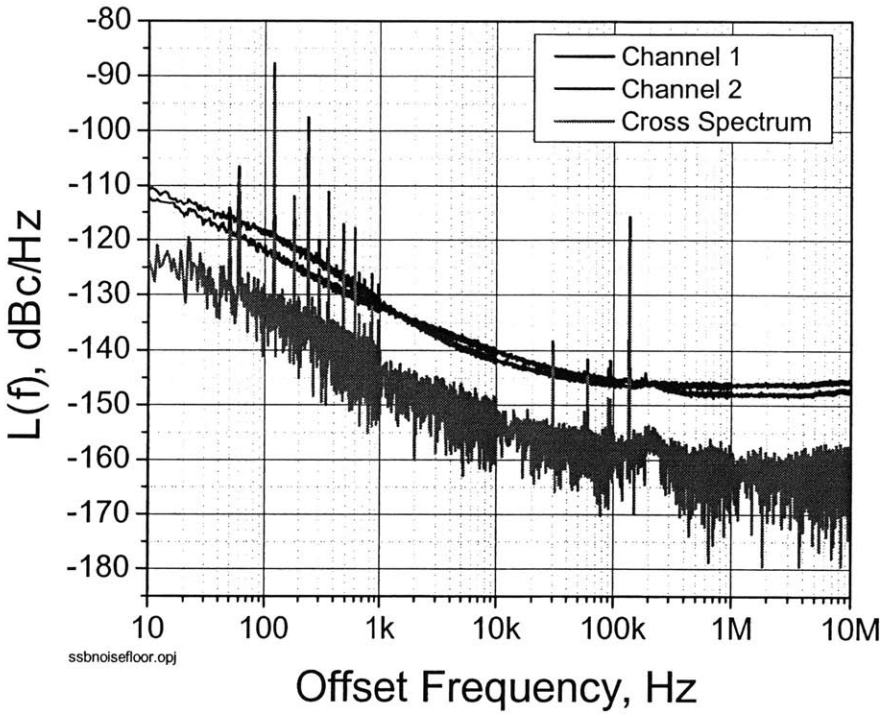

Figure 5-10: Single sideband phase measurement noise floor for channels 1 and 2 and for the electronic cross-correlation between the channels as a function of offset frequency.

kHz$< f <$ 100 kHz.

It was previously demonstrated in Ref. [87] that the measurement noise floor can be lowered by crosscorrelating the two channels using the FFT analyzer. The idea is that while the thermal noise from the preamplifiers between the two channels are uncorrelated, the phase noise we want to measure is correlated (and identical) in both channels. By crosscorrelating the two channels with the FFT analyzer, the uncorrelated thermal background is reduced. Using this technique, it was found that the noise floor was reduced an additional ~14 dB, as shown in Fig. 5-10. Each amplifier was driven with an independent power supply so as to mitigate power-supply-dependent noise that could lead to unwanted noise correlations. Johnson noise from a 50 Ω resistor (from the mixer or from the photodetector, for example) is $V = \sqrt{4kTR} = 0.9$ nV/$\sqrt{\text{Hz}}$ (-181 dBV/$\sqrt{\text{Hz}}$) where k is Boltzman's constant equal to $1.38x10^{-23}$ J/K, T is the ambient temperature of the resistor (ambient 293 K). This gives a level of -177 dBm/Hz, resulting in a phase-noise level of -174 dBc/Hz. This is well below the -132 dBc/Hz level of the amplifier and below the crosscorrelation level of -155 dBc/Hz (for offsets $>$ 50 kHz), suggesting that the noise floor is dominated by the thermal noise of the preamplifiers or from the local oscillator. The sharp spikes are due to ground loops and other electromagnetic pickups.

5.5 Timing Jitter Measurements

Fig. 5-11 shows the measured spectrum of the jitter for one set of laser parameters g~10, D = 0.1 ps^2, 10 nm, w_0 = 7.6 pJ, T_R = 483 kHz, τ = 1.05 ps with the modulation set to be mostly AM and a small amount of PM. For each decade of frequencies, the data was averaged and then reassembled. While residual phase-noise measurement schemes can reduce the influence of LO phase noise on the measurement, it has been observed that one achieves better results when using an LO with low-phase-noise[83]. This is perhaps due to the fact the LO noise can be reduced at low offset frequencies due to the filtering action of the modulator, but at higher offset frequencies the LO phase noise is not filtered, and a poor LO with large phase noise will dominate the spectrum. The phase noise of the 9.00 GHz oscillator (Poseidon Shoe-Box Oscillator: –112 dBc/Hz @ 100 Hz, -141 dBc/Hz @ 1 kHz, -161 dBc/Hz @ 10 kHz, -172 dBc/Hz @ 100 kHz) is lower than that of the laser phase noise. The many sharp spikes

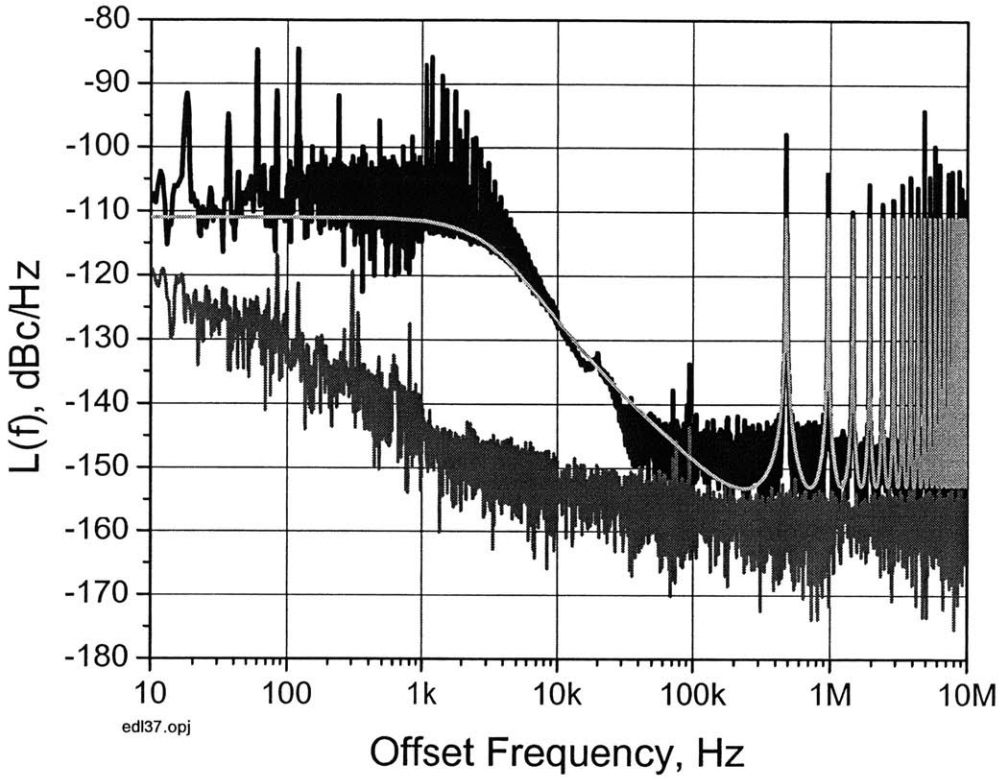

Figure 5-11: Single-sideband phase noise for the case of mostly AM. Dark solid line, data; gray line, theory; lower dark line, measurement noise floor.

from 10 Hz to 10 kHz and again at 70 kHz and 90 kHz are due to electromagnetic interference, ground loops, line voltage fluctuations, and their harmonics picked up in the detection circuitry and data acquisition cables.

The peak near 20 kHz corresponds to the relaxation-oscillation frequency of the laser and is mainly an artifact of insufficient amplitude noise rejection of the measurement system and does not contribute to phase noise[88]. The shoulder near 2.5 kHz is due to the retiming constant $1/\tau_{AM}$, after which the spectrum falls off by approximately 30 dB per decade (dB/dec) for $f > 2.5$ kHz and 20 dB/dec for $f > 50$ kHz. Another feature is the series of harmonics at 483 kHz–these are the cavity supermodes and reveal information about the pulse-to-pulse

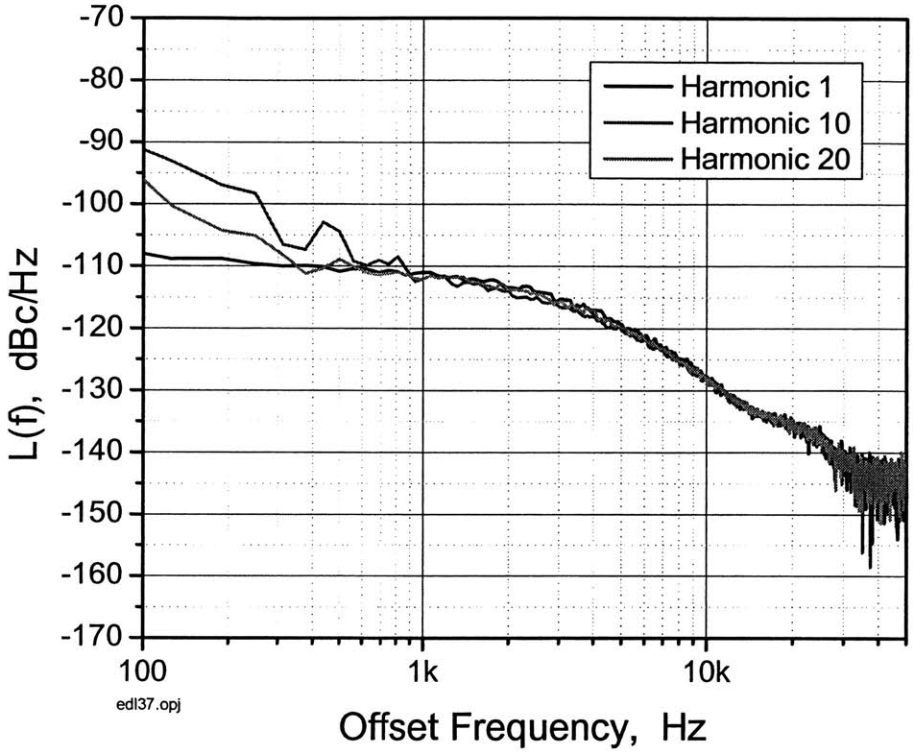

Figure 5-12: Single sideband phase noise of the baseband mode and supermodes using the measurement setup of Fig. 5-8 with electronic cross correlation. The spectra of the noise for harmonics 1, 10, and 20 are superimposed.

correlations[71].

The theory for the quantum-limited timing jitter from (5.1) is also shown in Fig. 5-11 where $L(f) = C\sum_n \left\langle |\Delta T(f - nf_R|^2 \right\rangle$, $f_0 = 483$ kHz, and C is a normalization constant. This is a valid model insofar as the pulses are uncorrelated. For the twenty displayed supermodes, we find that the supermodes have the same spectrum as the baseband mode as shown in Fig. 5-12 (the baseband mode is labeled as Harmonic 1 in the figure). This is consistent with the case in which the pulse-to-pulse noise is uncorrelated.

The theoretical fit shows that the apparently flat floor in the data near -152 dBc/Hz (and above the measurement noise floor) is due to the overlapping tails of the supermodes and not

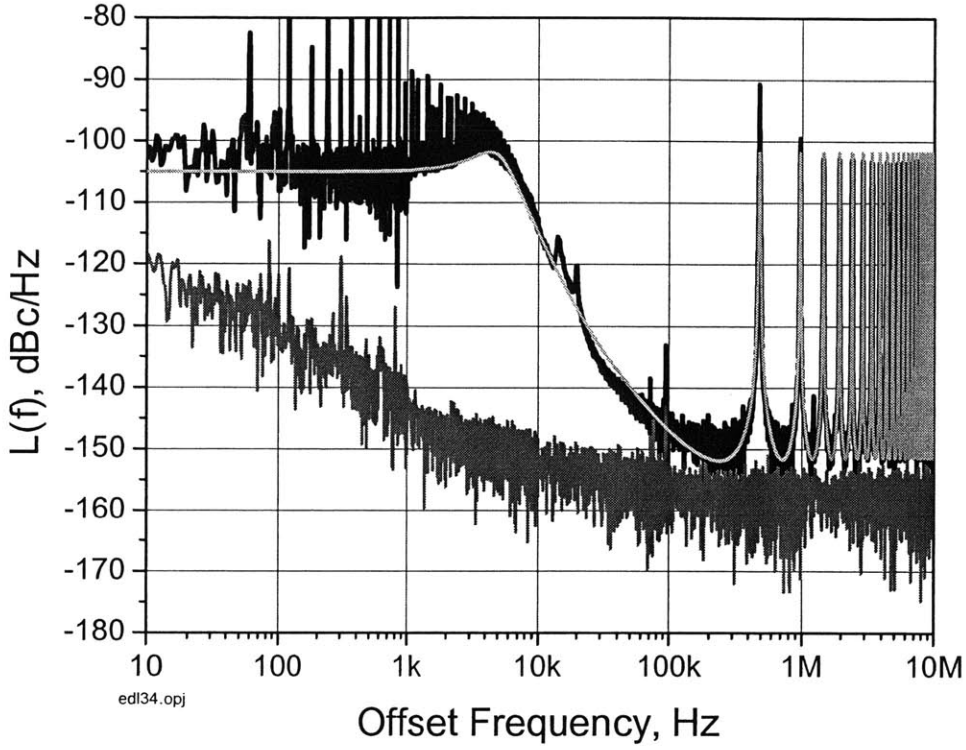

Figure 5-13: Single-sideband phase noise for the case of mostly PM. Dark solid line, data; gray line, theory; lower dark line, measurement noise floor.

due to thermal or shot noise. The level of the floor is very sensitive to the parameters used for fitting–it is not possible to independently adjust τ_p' and Ω_{PM}' without adjusting the level of the floor. The -152 dBc/Hz level is well above the calculated shot noise floor of ~ -166 dB (for an average photodetector current of 3.5 mA, incident optical power 7 mW, photodetector responsivity 0.5 A/W). The match between theory and the experiment–including the proper turning points in the spectrum as well as the supermode overlap–is quite good and verifies our theoretical model for the timing jitter.

For the case of Fig. 5-13, the laser parameters were kept fixed, but the amount of PM was increased at the expense of AM and the pulse width was increased to $\tau = 3.5$ ps. The features near 12 kHz, 70 kHz, and 95 kHz in Fig. 5-13 are artifacts of the measurement and not part of

the laser spectrum. The relaxation oscillation frequency can be observed near 20 kHz. The feature near 15 kHz was not present in repeated measurements and is probably a measurement artifact. The spectrum falls off rapidly for $f > 4$ kHz at approximately 40 dB/dec and 20 dB/dec for $f > 70$ kHz as predicted from the theory. For the case of Fig. 5-13, the GVD was not optimized to minimize jitter, and the product $4\left(\tau_p'\Omega_{PM}'\right)^2$ is $7.1 \gg 1$, consistent with underdamping (due to insufficient filtering) and the observed peak near 4 kHz. In comparison, $4\left(\tau_p'\Omega_{PM}'\right)^2$ is 1.1 for the case of Fig. 5-13, indicating critical damping.

Phase noise can be readily converted into a measure of timing jitter, σ, in a root-mean-square sense

$$\sigma\left[f_l, f_h\right] = \frac{1}{2\pi f_m}\sqrt{\int_{f_l}^{f_h} L(f)df} \tag{5.14}$$

where f is the frequency offset measured from the laser repetition rate, and f_l and f_h are the low and high limits of integration. The results of the integrated data via equation (5.14) and the theoretical values are given in Table 5.3. The discrepancy between the theoretical and measured values is mainly due to the inclusion of the erroneous noise spurs in the measurement system.

5.6 Conclusion

In conclusion, we have observed the quantum-limited timing jitter of an active, harmonically modelocked laser. We have examined the influence of AM and PM on the timing jitter spectrum and compared the measured spectrum and the governing characteristic coefficients with that determined by theory. We have shown that the measured spectra of the timing jitter is in good agreement–both qualitatively and quantitatively, with that given by the theory developed in chapter 3. We have also shown that the spectra of the supermodes are identical to that at baseband, indicative of uncorrelated pulse-to-pulse timing jitter. With knowledge of the quantum-limited jitter spectrum, we can engineer the laser parameters to achieve lower jitter.

Integration. Range	σ, Fig.5-11	σ, Fig. 5-13
10 Hz-241.5 kHz	9.74 (9.66) fs	80.0 (62.2) fs
10 Hz-10 MHz	37.0 (19.3) fs	113.2 (88.1) fs

Table 5.3: Integrated jitter values of the data; measured values (no parenthesis) and theoretical values (in parenthesis).

5.7 Future Work and Ideas

The sigma laser cavity used in these experiments are on the order of ~200 m long, with effective cavity lengths on the order of ~400 m. These very long cavities require good enclosures, electronic feedback, and temperature control to maintain good modelocking. Making a shorter fiber laser (say, on the order of meters) would be advantageous in that the cavity would be much less sensitive to environmental perturbations.

Applying stretched-pulse (or dispersion-managed) laser design principles to the actively modelocked laser would benefit in achieving very low dispersion while maintaining high pulse energy. Achieving stretching ratios on the order of 2-3 is difficult for picosecond pulses. For example, the sum of GVD through each section of a two-section, balanced dispersion-managed laser (one section with anomalous GVD, the other section with normal GVD of the same absolute value) for a 2 ps pulse would need to be 12 ps^2, equivalent to propagation through 600 m of SMF. While it has been reported that significant stretching is occurring in some sigma laser designs with only ~200 m of length[45], it would be optimal if some other means for achieving large swings in GVD could be attainable in a shorter span.

Chapter 6

Timing Jitter in Harmonically Modelocked Lasers

6.1 Introduction

[1]The spectrum of the noise for a harmonically modelocked laser differs from that of a fundamentally modelocked laser due to the nature of the pulse-to-pulse correlations. In this chapter, we derive the spectrum of the timing jitter for a harmonically modelocked laser for the case of uncorrelated noise and give experimental results that verify the model.

6.2 Model

Rather than starting from the master equation of modelocking, we will begin our analysis assuming a train of pulses generated by the laser with pulse-to-pulse correlations we will specify and not derive from first principles. Consider a train of pulses with intensity $I(t)$ modelocked at the Nth harmonic:

$$I(t) = \sum_n E_0 f(t - nT_N) \tag{6.1}$$

where E_0 is the average pulse energy, f the time-dependent intensity of a single pulse normalized such that its integration is unity, T_N the average separation between pulses where the repetition

[1]Work in this section was accomplished in close collaboration with John Fini, Leaf Jiang, and Farhan Rana, and many of the results reported here appear in Ref. [71].

rate $f_N = 1/T_N = N/T_R$ where T_R is the round-trip fundamental cavity delay, and $P_0 = E_0/T_N$ is the average power. The notation used here is slightly different than that presented in a previous chapters (i.e., we previously used "T" as a time scale in the master equation as that on the scale of pulse separations, and "t" on the time scale of the pulse width). The notation used here was modified to be consistent with Ref. [71]. Introducing timing and energy fluctuations $\Delta E[n]$ and $\Delta t[n]$ and expanding to first order,

$$\begin{aligned} I(t) &= \sum_n \left(E_0 + \Delta E[n]\right) f\left(t - nT_N - \Delta t[n]\right) \\ &\simeq \sum_n \left(E_0 + \Delta E[n]\right) f\left(t - nT_N\right) - E_0 \sum_n \dot{f}\left(t - nT_N\right) \Delta t[n] \end{aligned} \tag{6.2}$$

Assuming stationary noise processes, we can characterize the noise of the laser with correlation functions, written as

$$R_{\alpha\beta}[n] = \langle \Delta\alpha[n] \Delta\beta[0] \rangle \tag{6.3}$$

where $[\alpha, \beta]$ equals any one of $[E, t]$. For the rest of this section, we will only be concerned with timing jitter, and we will assume that there is no coupling between amplitude and timing such that $R_{EE}[n] = R_{Et}[n] = 0$. The Fourier transform of the correlation function is the spectral density[89]:

$$S_{tt}(\Omega) = \sum_{n=-\infty}^{\infty} R_{tt}[n] \exp\left(-j\Omega T_N n\right) \tag{6.4}$$

The spectral density function is periodic with the period of the repetition rate, $1/T_N$. If the spectral density functions are known (i.e., by measurement), we can take the inverse Fourier transform of the spectral density to find the correlation function, given by

$$R_{tt}[n] = \frac{1}{\omega_N} \int_{-\omega_N/2}^{+\omega_N/2} S_{tt}(\Omega) \exp\left(j\Omega T_N n\right) \, d\Omega \tag{6.5}$$

where the integration bandwidth is that over a single period at repetition rate $f_N = \omega_N/(2\pi)$. The rms value of the timing jitter is the integrated spectral density function,

$$\sigma_t^2 = \int_{-\omega_N/2}^{+\omega_N/2} S_{tt}(\Omega) \, d\Omega \tag{6.6}$$

$$= R_{tt}[0] \tag{6.7}$$

So far, our approach has used discrete notation for the pulses, as was done in Ref. [90]. The use of continuous functions[89] for the correlations was done similarly[43][76] with the same results.

6.3 Harmonic Modelocking, Uncorrelated Noise

For the case in which N pulses within the laser cavity are uncorrelated with each other, the correlation function $R_{tt}[n]$ is nonzero only for pulses that are separated by an integer multiple of round trips; i.e., pulse n and $n+kN$ are correlated for integers k. In the frequency domain, the frequency of correlation is not the repetition rate as for a fundamentally modelocked laser, but rather given by the frequency of the round-trip time where $f_R = 1/(N \cdot f_N)$. Then the spectral density function from (6.4) becomes

$$\begin{aligned} S_{tt}(\Omega) &= \sum_{n=-\infty}^{\infty} R_{tt}[n] \exp\left(-j\Omega T_N n\right) \\ &= \sum_{k=-\infty}^{\infty} R_{tt}[kN] \exp\left(-j\Omega T_N kN\right) = \sum_{k=-\infty}^{\infty} R_{tt}[kN] \exp\left(-j\Omega T_R k\right) \end{aligned} \tag{6.8}$$

The spectral density $S_{tt}(\Omega)$ is periodic with frequency given by that of the round-trip frequency–this is a result that we have shown in chapter 5 (recall Figs. 5-1, 5-2, 5-11, and 5-13)–the spectrum of the noise is aliased at harmonics of the round-trip time. The root-mean-square of the timing jitter can be found by either integrating the spectral density over a frequency span given by the repetition rate f_N (up to the Nyquist rate for a periodic signal at f_N), or by just integrating over a frequency span given by the round-trip rate f_R and multiplying by square of the harmonic number N:

$$\sigma_t = \frac{1}{2\pi f_N} \sqrt{\int_{-\omega_N/2}^{\omega_N/2} S_{tt}(\Omega)\, d\Omega} \tag{6.9}$$

$$= \frac{\sqrt{N}}{2\pi f_N} \sqrt{\int_{-\omega_R/2}^{\omega_R/2} S_{tt}(\Omega)\, d\Omega} \tag{6.10}$$

Correlations can develop between pulses in the laser cavity through a number of mechanisms. It was shown[91] in a previous experiment on a harmonically modelocked semiconductor laser

that the pulses amplitudes were negatively correlated through the laser gain dynamics. For actively modelocked fiber laser, the phase noise of the active modelocker positively correlates the pulses and appears in the spectrum of the timing noise at the repetition rate (low-frequency spectrum in a residual phase-noise measurement) and does not appear at the supermodes. The formalism for handling generalized pulse-to-pulse correlations can be found in Ref. [71].

The spectrum of the noise can be found by a number of methods. The photocurrent $i_{\mathrm{det}}(t)$ after direct detection of the train of laser pulses is given by

$$i_{\mathrm{det}}(t) = \eta \int \chi'(t') I(t - t')\, dt' \tag{6.11}$$

where $\chi(t')$ is the photodetector response (normalized to have unity area) and η the photodetector responsivity (in units of A/W). Assuming a photodetector whose bandwidth is much larger than the largest offset frequency of interest, then the spectrum of the photocurrent noise is given by

$$\begin{aligned} S_{II}(\Omega) &= \lim_{T\to\infty} \frac{1}{T} \int_{-T/2}^{T/2} \langle [i_{\mathrm{det}}(t) - \langle i_{\mathrm{det}}(t)\rangle]\,[i_{\mathrm{det}}(t+\tau) - \langle i_{\mathrm{det}}(t+\tau)\rangle]\rangle\ dt \\ &\approx (\eta P_0)^2 \left[\frac{1}{P_0^2 T_N} S_{ee}(\Omega) + \Omega^2 T_N S_{tt}(\Omega) + \frac{j\Omega}{P_0} \left[S_{ET}(\Omega) - S_{ET}^*(\Omega) \right] \right] \\ &\approx (\eta P_0)^2\, \Omega^2 T_N S_{tt}(\Omega) \end{aligned} \tag{6.12}$$

where we have assumed that the amplitude noise and amplitude-timing noise are zero. Note that this is the spectrum of the photocurrent noise, so the sum of delta functions that usually appears has been subtracted out from (6.12). This is the result Von der Linde had derived previously[75]–the spectrum of the timing jitter appears in the spectrum of the photocurrent noise directly proportional to the square of the offset frequency.

Using residual phase-noise techniques (discussed in chapter 5) allows for a more direct measurement of the timing jitter spectrum by automatically subtracting out the deterministic signal, achieves high dynamic range, and facilitates measurements at lower frequencies where one can use more sophisticated electronic processing (Hz to MHz) than that available at higher frequencies (tens of GHz). In that case, we find that the measured single-sideband phase noise

$L(\Omega)$ can be easily related to the spectrum of the jitter $S_{tt}(\Omega)$ by a proportionality constant–one that is typically calibrated for a given measurement setup.

6.4 Measurements

The sigma fiber laser from the previous section was used for the experiments. The data for the cases of mostly AM and PM and the fits to the jitter theory assuming uncorrelated supermodes from Figs. 5-11 and 5-13 give very strong evidence of the case for uncorrelated pulses. A closer look at the overlapping spectra shown in Fig. 5-12 also shows very strong agreement for the case of uncorrelated pulses.

Another test of the theory is to compare the integrated timing jitter from single-sideband traces with the timing jitter obtained from cross-correlation measurements. For the test, a dielectric resonant DRO with oscillation frequency at 10.0 GHz and internally phase-locked to the external 10 MHz reference of an HP 83732B synthesizer was used for a local oscillator (NXPLOS-IX-1000). The performance of the sigma laser was similar to that when driven with the 9.00 GHz Poseidon ShoeBox oscillator–a typical optical spectrum and RF spectrum with over 80 dB of sidemode suppression are shown in Figs. 6-1 and 6-2.

A typical single-sideband phase noise spectrum of the sigma laser is shown in Fig. 6-3. The maximum offset frequencyof 1 GHz is 1/5 of the 5 GHz Nyquist frequency (for a repetition rate of 10 GHz) and limited by the IF frequency output of the double-balanced mixer. IUnlike the measurements in chapter 5, the floor near -145 dBc/Hz is due to the noise floor of the NXPLOX-IX-1000 local oscillator. The integrated spectrum from 100 Hz to 10 MHz is 27.2 fs, and from 10 MHz to 1 GHz is 243.5 fs. Multiplying by 5 (to get to Nyquist frequency and assuming that the jitter spectrum is the same in the 1-5 GHz range as it is in the ~0-1 GHz), the jitter is calculated as 1.11 ps. Because the measurement is limited by the LO noise floor, this is an overestimate of the noise–assuming a constant level of -145 dBc/Hz over all frequencies, the local oscillator noise floor integrates to 89.5 fs. We can also calculate the jitter by integrating the jitter around one of the supermodes and multiplying by $\sqrt{N}$ where $N = 20921$ is the harmonic number of the cavity. For a typical harmonic, integrating by the jitter over a span of 478 kHz yields 2.70 fs, and the total rms jitter is calculated as $2.70 \times \sqrt{20921} = 391$ fs. This

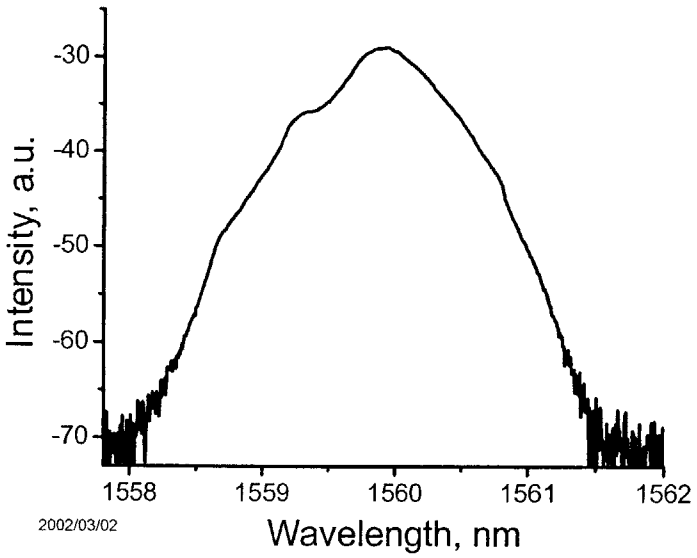

Figure 6-1: A typical optical spectrum of the directly-detected photocurrent (log scale) for the 10.0 GHz sigma laser driven with the DRO.

is a factor of 2.8 less than that computed by integrating the full jitter spectrum.

We can compare these results to those obtained by optical cross correlations[76][77]. For the case of uncorrelated pulses, the broadening of the detected SHG cross correlation compared to that of the autocorrelation is a good measure of the total rms timing jitter (integrated over all frequencies). We found that delaying pulse 1 to pulse number 2, 3, and approximately pulse numbers 99, 100, 101, 102, 4997, 4998, 4999, and 5000 that the broadening due to cross correlation remained constant, which is further verification of the claim that the timing jitter between pulses in one round trip (i.e., within one pulse pattern) are uncorrelated. Fig. 6-4 shows a typical cross-correlation trace for one pulse delay. The timing jitter computed from the broadening of the cross-correlation trace compared to the autocorrelation trace is given by

$$\sigma = \sqrt{\tau_{xc}^2 - \tau_{ac}^2} \tag{6.13}$$

where τ_{xc} is the cross-correlation width, and τ_{ac} is the autocorrelation width. For the data in Fig. 6-4, the autocorrelation width was 4.82 ps, and the ensemble-averaged cross-correlation

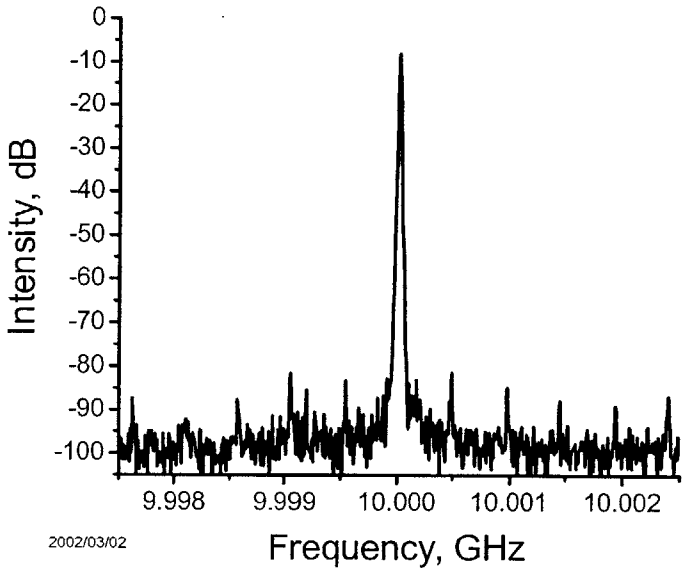

Figure 6-2: A typical RF spectrum of the directly-detected photocurrent for the 10.0 GHz sigma laser driven with the DRO.

width was 4.91 ps, resulting in $\sigma = 0.95 \pm .3$ ps (the magnitude of the error is a measure of the repeatability of the cross-correlation traces over a large number of data sets and not an absolute measurement error). This is within a factor of ~2.5 of the estimated value assuming that all the pulses are uncorrelated.

6.5 Conclusions

We have presented a model of the timing jitter for harmonically modelocked lasers and found that for the case of uncorrelated noise, the spectrum of the timing noise aliases at the supermodes. We also showed that the timing jitter can be computed by either integrating over the repetition rate or by just integrating over one round-trip frequency and multiplying by the square root of the harmonic number.

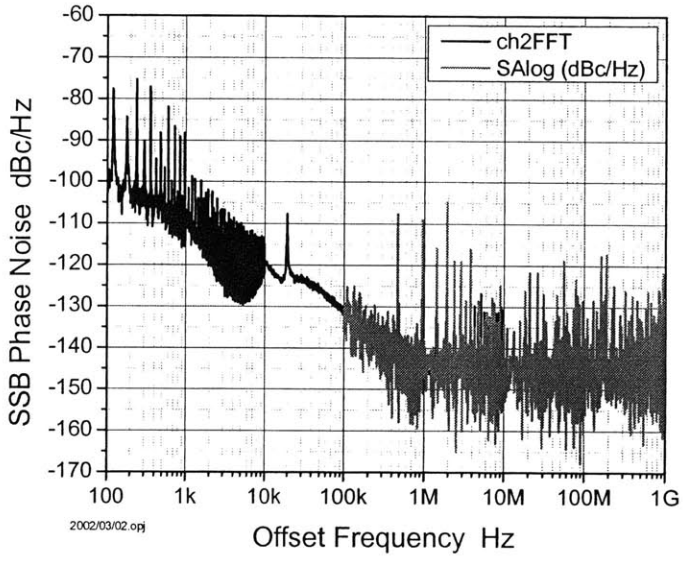

Figure 6-3: Single-sideband phase noise spectrum. The HP 89410A (single channel) was used for the range 100 Hz to 10 MHz. The Agilent RF spectrum analyzer was used from 100 kHz to 1 GHz (with a scaled resolution bandwidth for each decade of offset frequencies).

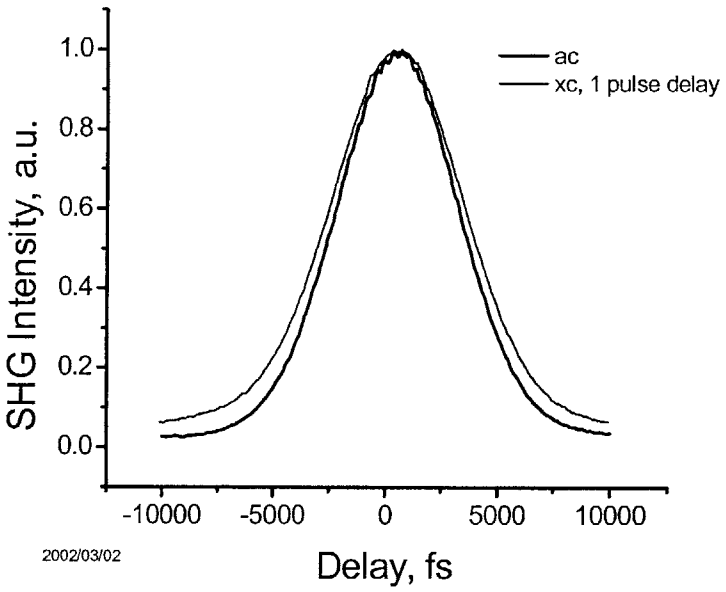

Figure 6-4: Intensity of the second-harmonic signal generated from a background-free for two traces: an auto-correlation trace and a cross-correlation trace between two neighboring pulses.

6.6 Future Work and Ideas

Results have been reported for the active, harmonic modelocking of a fiber laser using a Fabry-Perot etalon (FPE) designed such that the free-spectral range is equal to the repetition rate helps to prevent pulse dropouts[92][93]. It was also shown recently (Delfyett group, CREOL) that an FPE suppresses the supermode noise. It is important to understand the degree of correlation using an FPE, including correlations of the pulse-to-pulse optical phase. It is conjectured that using the FPE should act as a noise filter and reduce the absolute phase of the pulse train. It has been shown that some means for correlating pulses–such as using a composite cavity[94][95]–only results in a redistribution rather than an overall reduction of the timing jitter.

Chapter 7

Timing Jitter Reduction using Phase Modulation and Group-Velocity Dispersion

7.1 Introduction

[1]In this chapter, we study linear Hamiltonian processes, such as dispersion in an optical fiber, and time-dependent processes, such as phase modulation, which affect the position (timing) and momentum (carrier frequency) of an optical pulse. These processes are closely analogous to the quantum propagation of a free particle and its focusing by a lens[96]. While the problem of quantizing a propagating electric field in both linear dispersionless inhomogeneous dielectric media and in linear homogeneous dielectric media with dispersion have been studied[97][98][98][99][100][101][102], the effects of phase modulation have not. The combination of dispersion and phase modulation can reduce the position fluctuations (timing jitter) at the expense of momentum fluctuations (carrier frequency jitter). This can be contrasted with generation of squeezed states–using parametric processes utilizing either second order ($\chi^{(2)}$) or third order ($\chi^{(3)}$) nonlinearities[103][104][105][106][107][108][109]–in which the projections of zero-point fluctuations are manipulated through their phase-sensitive nature. Classical ana-

[1]Work in this section benefitted greatly from contributions from John Fini and Prof. J. Shapiro. Prof. H. Haus provided most of the key concepts for this work, much of which appears in Ref. [59].

logues to squeezing have also been demonstrated[110][111][112]. The approach here achieves a reduction of position uncertainty by renormalization of the excitations and is entirely classical. Aside from its theoretical interest, this finding is of practical importance: the reduction of the timing jitter of a pulse can improve the accuracy of optical sampling for analog-to-digital conversion[2][11][12][14][17] and for retiming pulses at the end of a transmission link. A process that reduces the timing jitter at the expense of frequency jitter leads to improvement of the timing signal, since the optical bandwidth of detectors is large enough to be insensitive to frequency jitter. We consider Gaussian pulses, such as are produced by active modelocking, and quantize them. We develop equations of motion for the position and momentum operators as affected by dispersion and phase modulation. Then we show that this system conserves commutator brackets and thus the area of the uncertainty ellipse. Reduction of pulse position fluctuations (timing jitter) is demonstrated theoretically.

7.2 Quantization of the Optical Pulse

We consider a periodic train of Gaussian pulses. The envelope of the electric field amplitude is quantized if described in terms of the annihilation operator $\hat{a}(T, x)$, where T and x represent two time scales: the slow time scale T of pulse evolution, and the fast time scale (expressed as a spatial scale) $x = v_g t$, where v_g is the group velocity. The operator obeys the commutation relation[113][114]

$$[\hat{a}(T, x), \hat{a}^\dagger(T, x')] = \delta(x - x') \tag{7.1}$$

We separate the excitation into a classical c-number part a_0 in terms of which the pulses are described, and a perturbation operator $\Delta\hat{a}$ that characterizes the noise

$$\hat{a} = a_0 + \Delta\hat{a} \tag{7.2}$$

The commutator associated with the perturbation operator is:

$$[\Delta\hat{a}(T, x), \Delta\hat{a}^\dagger(T, x')] = \delta(x - x') \tag{7.3}$$

Focusing on one of the pulses, we write the c-number part of the excitation in the form

$$a_0 = A_0\psi_0(\frac{x}{\xi}) \tag{7.4}$$

where ψ_0 is the zeroth-order Hermite-Gaussian of the set:

$$\psi_n(\frac{x}{\xi}) = \frac{1}{\sqrt{2^n n!\xi\sqrt{\pi}}} H_n(\frac{x}{\xi}) e^{\frac{ix^2}{2\omega''(T-ib)}} e^{-i(n+1)\phi} \tag{7.5}$$

where $b = \xi_0^2/\omega''$, $\omega'' = d^2\omega/d\beta^2$ is the group-velocity dispersion, and $\phi = \tan^{-1}(z/b)$. This set expresses, in general, chirped pulses after a time T starting with minimum width ξ_0. The pulse width changes when the pulse propagates in a dispersive medium according to the law

$$\xi^2 = \xi_0^2\left[1 + \left(\frac{T}{b}\right)^2\right] \tag{7.6}$$

The perturbation is expanded in a complete set

$$\Delta\hat{a} = \Sigma_n \Delta\hat{A}_n \psi_n(\frac{x}{\xi}) \tag{7.7}$$

The annihilation operators $\Delta\hat{A}_n$ can be expressed as sums of Hermitian operators

$$\Delta\hat{A}_n = \Delta\hat{A}_n^{(1)} + i\Delta\hat{A}_n^{(2)} \tag{7.8}$$

where $\Delta\hat{A}_n^{(1)}$ and $\Delta\hat{A}_n^{(2)}$ are in quadrature. A displacement and a carrier frequency change are represented by the first-order Hermite-Gaussian. The coefficient ΔA_1 is obtained from the expansion of a pulse that has been displaced by ΔX and frequency shifted by $\Delta\omega$. The pulse is described by

$$A_0\psi_0(x, T, \Delta X, \Delta\omega) = \frac{A_0}{\sqrt{\xi\sqrt{\pi}}} \exp\left[i\frac{(x - \Delta X + \omega''\Delta\omega T/\nu_g)^2}{2\omega''(T - ib)}\right] \exp\left[-i\frac{\Delta\omega x}{\nu_g}\right] \exp\left[-i\phi\right] \tag{7.9}$$

The expansion is carried out to first order in ΔX and $\Delta\omega$, the perturbations are replaced by operators, and the result is equated to $\Delta\hat{A}_1\hat{\psi}_1(x,T)$ with the result

$$\Delta\hat{A}_1 = \frac{1}{\sqrt{2}}\left(\frac{\Delta\hat{X}}{\xi_0} - i\frac{\Delta\hat{\omega}}{\nu_g}\xi_0\right) = \frac{1}{\sqrt{2}}\left(\frac{\Delta\hat{X}}{\xi_0} + i\Delta\hat{P}\xi_0\right) \tag{7.10}$$

where we have introduced the momentum operator

$$\frac{\Delta\hat{\omega}}{\nu_g} = -\Delta\hat{P} \tag{7.11}$$

The position and momentum operators can be related to the in-phase and quadrature components of the expansion coefficient $\Delta\hat{A}_1$

$$\Delta\hat{X} = \frac{\sqrt{2}}{A_0}\xi_0\Delta\hat{A}_1^{(1)} \text{ and } \Delta\hat{P} = \frac{\sqrt{2}}{A_0}\frac{1}{\xi_0}\Delta\hat{A}_1^{(2)} \tag{7.12}$$

The operators $\Delta\hat{A}_1^{(1)}$ and $\Delta\hat{A}_1^{(2)}$ obey a commutation relation that can be gleaned from (7.3) and (7.8)

$$\left[\Delta\hat{A}_1^{(1)}, \Delta\hat{A}_1^{(2)}\right] = \frac{i}{2} \tag{7.13}$$

We find the commutation relation for position and momentum

$$\left[\Delta\hat{X}, \Delta\hat{P}\right] = i\langle n\rangle \tag{7.14}$$

where $\langle n\rangle = A_0^2$ is the average photon number.

7.3 Phase Modulation and Group-Velocity Dispersion

A carrier frequency shift changes the group velocity of the pulse propagation. A pulse propagating over a time T changes its position in a manner proportional to the carrier frequency change and the dispersion $\omega'' = d^2\omega/d\beta^2$. This leads to an equation relating the position after propagation over a time T to its initial value $\Delta\hat{X}(0)$

$$\Delta\hat{X}(T) = \Delta\hat{X}(0) + \omega''T\Delta\hat{P}(0) \tag{7.15}$$

A phase modulator multiplies the pulses of equation (7.7) by $iM\cos\Omega_M(t-\Delta X/v_g)$, where M is the depth of modulation, and Ω_M is the modulation frequency. When expanded to first order in ΔX, we find a first-order Hermite Gaussian in quadrature. This term produces a momentum perturbation

$$\Delta\hat{P}_{out} = \Delta\hat{P}_{in} - M\frac{\Omega_M^2}{v_g^2}\Delta\hat{X} \tag{7.16}$$

7.4 ABCD Formalism for Position and Momentum

We have found that the operators $\Delta\hat{X}$ and $\Delta\hat{P}$ between input and output experience transformations that can be described by ABCD matrices

$$\begin{bmatrix} \Delta\hat{X}_{out} \\ \Delta\hat{P}_{out} \end{bmatrix} = \begin{bmatrix} A & B \\ C & D \end{bmatrix} \begin{bmatrix} \Delta\hat{X}_{in} \\ \Delta\hat{P}_{in} \end{bmatrix} \tag{7.17}$$

The matrices are, respectively, for propagation through dispersion:

$$\begin{bmatrix} A & B \\ C & D \end{bmatrix} = \begin{bmatrix} 1 & \omega''T \\ 0 & 1 \end{bmatrix} \tag{7.18}$$

and through a phase modulator

$$\begin{bmatrix} A & B \\ C & D \end{bmatrix} = \begin{bmatrix} 1 & 0 \\ -M\frac{\Omega_M^2}{v_g^2} & 1 \end{bmatrix} \tag{7.19}$$

The determinants of these matrices are unity, and cascading of the components leads to ABCD matrices that also have a unity determinant as required by Heisenberg's uncertainty principle.

An example of a position fluctuation reduction arrangement is shown in Fig. 7-1. A section of dispersive fiber ω_1'' and delay T_1 is followed by a phase modulator, and then followed by another dispersive fiber ω_2'' with delay T_2. The computed position fluctuation reduction is shown in Figs. 7-2a and 7-2b for the cases where the input position and momentum fluctuations are uncorrelated. The uncertainty of the pulse position at the output has been reduced at the expense of the momentum uncertainty in regions of phase space in which $S < 1$. We find that the best position fluctuation reduction occurs for the case where the modulation depth and

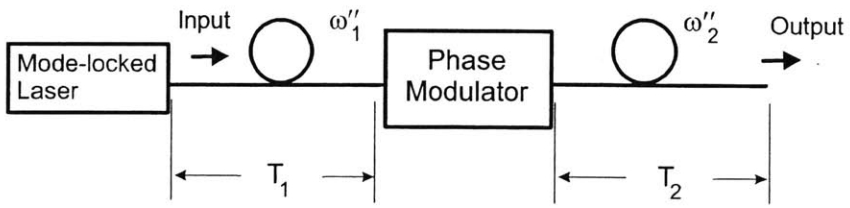

Figure 7-1: Schematic of system analyzed for Fig. 7-1 where ω'' is the group-velocity dispersion, and T the propagation delay.

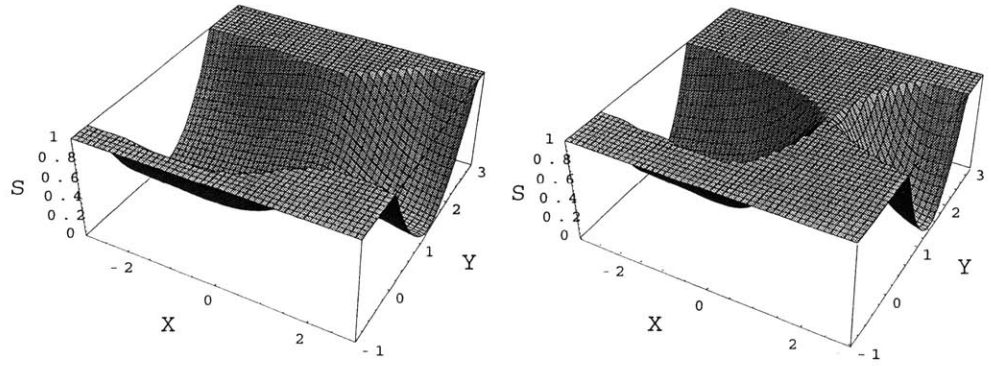

Figure 7-2: $R = (M\Omega_M^2/v_g^2)^2 \left\langle \left|\Delta\hat{X}\right| \right\rangle^2 / \left\langle \left|\Delta\hat{P}\right| \right\rangle^2$ for the cases (a) $R_{in} = 2$ and (b) $R_{in} = 1$ where $S \equiv R_{out}/R_{in}$, $X \equiv (M\Omega_M^2/v_g^2)\omega_1''T_1$, and $Y \equiv (M\Omega_M^2/v_g^2)\omega_2''T_2$. The pulse position fluctuations are reduced in the regions where $S < 1$. Regions for $S > 1$ are not shown.

modulation frequency are large, and the dispersion $\omega''T$ is large and can be either anomalous or normal. Experimentally, the measurement of position fluctuations is classical and can be achieved using conventional RF phase noise detection techniques employing direct detection with a fast photodetector, a double-balanced mixer, and a local oscillator (as shown in chapter 5), and the position fluctuations before and after the setup of Fig. 7-1 can be compared.

7.5 Conclusions

We have shown that the perturbation operators of pulse position and momentum, when acted upon by dispersive propagation and/or phase modulation, obey an $ABCD$ matrix transformation. The uncertainty ellipse of position and momentum fluctuations can be transformed using

a system containing phase modulators and dispersive propagation segments. The reduction of position fluctuations can be used to improve timing signals obtained from detected pulse trains. The system need not operate at the minimum uncertainty limit to be of use.

7.6 Ideas and Future Work

Preliminary experiments[115] have shown that jitter reduction using phase modulation and GVD is possible. Additional experiments are under way.

Chapter 8

Two-Photon Absorption for Supermode Suppression

8.1 Introduction

[1]In chapters 4 and 5, the fiber lasers that were demonstrated were hundreds of meters long, leading to fundamental repetition rates of hundreds of kHz or a few MHz. Achieving GHz repetition rates required that the laser operate at a harmonic, N, of the fundamental repetition rate, which created N pulses per round trip. However, because of the millisecond gain lifetime of erbium, the gain cannot equalize the pulse energies in each of the time slots in a fiber laser so that, in general, the output may contain unequal-amplitude pulses or even pulse dropouts, as illustrated in Fig. 8-1.

Several techniques for stabilizing the pulse trains of harmonically modelocked lasers have been developed. A high-finesse Fabry-Perot etalon matched to the repetition rate of the laser produced a stabilized output[93]. Several techniques that use intensity limiting have been demonstrated to equalize pules energies. Proper biasing of nonlinear polarization rotation in the presence of a polarizer provides a stabilization mechanism through additive-pulse limiting. Although this technique is effective, it suffers from environmental instability[47]. Recently, other researchers demonstrated that the regime of stability can be extended by use of dispersion

[1]Experiments in this section were obtained in collaboration with Erik Thoen, Elizabeth Koontz, Gale Petrich, and Prof. L. Kolodziejski. Results from this chapter also appear in Refs. [49][116][117].

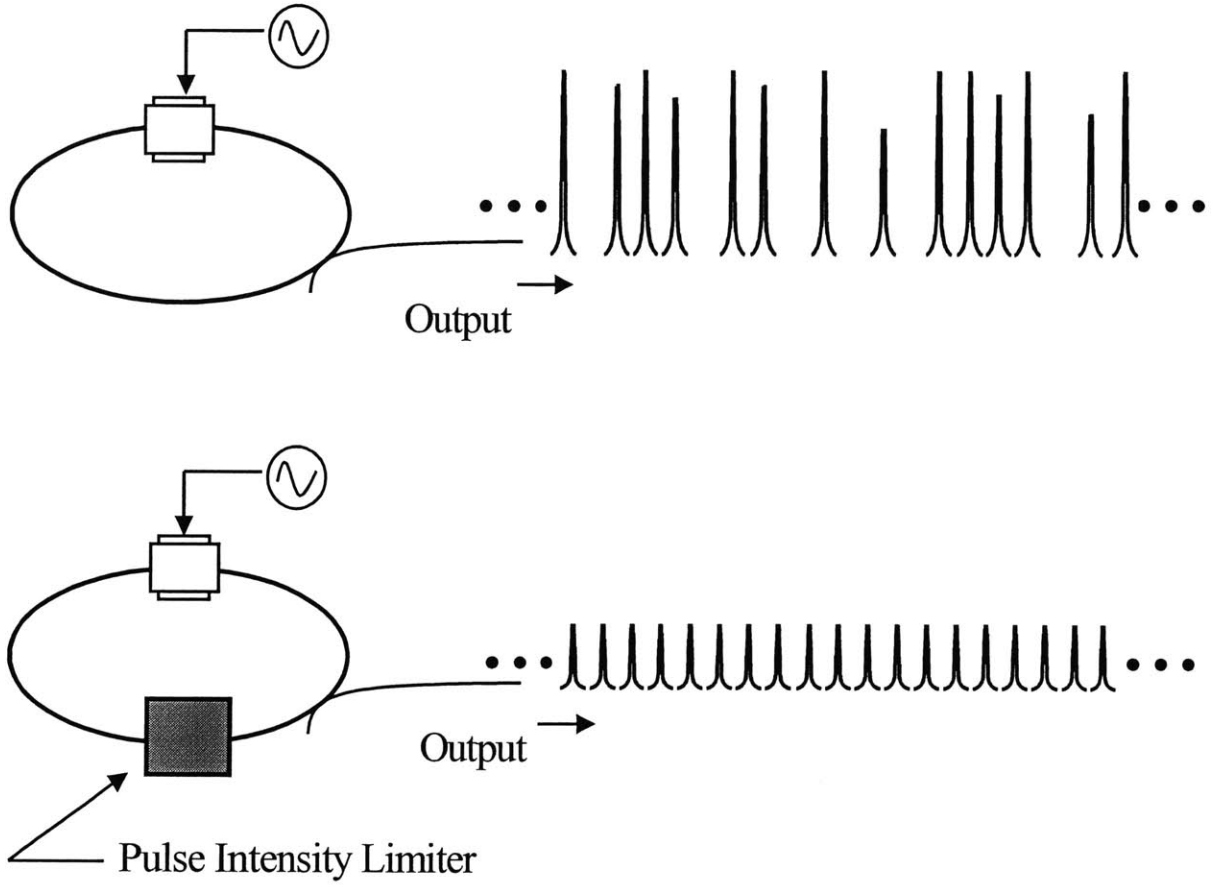

Figure 8-1: Illustration of the phenomenon of pulse dropouts and amplitude fluctuations in an active, harmonically modelocked ring laser. Pulse dropouts are prevented using an intracavity pulse intensity limiter that operates on the pulse peak intensity. The average power in the cavity is distributed equally among the time slots.

management in a sigma laser[118]. Spectral broadening owing to self-phase modulation (SPM) in the presence of filtering stabilizes against pulse fluctuations[48]–this is the technique used for the fiber lasers previously presented in this thesis. However, hundreds of meters of fiber are typically required for generating the necessary SPM to stabilize the pulse train, and long fiber lengths are undesirable because of the enhanced instability due to environmental fluctuations.

Peak-intensity limiting in the form of two-photon absorption (TPA) by a GaAs wafer in transmission was shown to prevent Q switching in fundamentally modelocked Nd:YAG laser[119]. Recently, TPA in a semiconductor saturable absorber mirror was used to stabilize pulses against Q-switched modelocking[4][120]. In this chapter, we report on experiments exploiting TPA in a semiconductor mirror to stabilize a train of picosecond pulses and prevent pulse dropouts in a short 2 GHz harmonically modelocked fiber laser.

8.2 Theory of Operation

Stabilization of pulse intensities requires a mechanism that responds much faster than the pulse repetition rate (tens to hundreds of ps) and is sensitive at low (~pJ) pulse energies. Pulses with carrier frequencies near 1.55 μm have energies ~0.8 eV and are transparent at low fluence when incident on a semiconductor such as InP with a bandgap of ~1.35 eV. As the fluence of the incident pulse increases, the probablity of two-photon absorption increases. The instantaneous transmission through a TPA region of length L is given by

$$1 - q_{TPA} = \exp\left(-\alpha_{TPA} L\right) \tag{8.1}$$

where q_{TPA} is the instantaneous loss and α_{TPA} is the TPA loss coefficient given by

$$\alpha_{TPA} = \frac{\beta A_{Struct} |A|^2}{A_{Eff}}$$

where β is the TPA coefficient for the material (typically in units of cm^2/GW), A the intensity of the electric-field envelope, A_{Struct} a parameter accounting for structural effects (e.g., standing wave field, intensity enhancement due to various optical coatings), and A_{Eff} the spot size on

the TPA region. For small TPA absorption,

$$q_{TPA} \simeq \alpha_{TPA} L \tag{8.2}$$

The time-averaged loss (absorption) for the pulse is expressed as

$$\tilde{q}_{TPA} = \frac{1}{w_0} \int_{-\infty}^{\infty} q_{TPA} |A|^2 dt \tag{8.3}$$

where w_0 is the average pulse energy. Assuming a hyperbolic secant pulse shape with pulse width τ

$$A = A_0 \text{sech} \frac{t}{\tau} \tag{8.4}$$

we can solve for time-averaged loss by substituting eqns. (8.2) and (8.4) into (8.3)

$$\tilde{q}_{TPA} = \frac{\alpha_{TPA} L}{w_0} \int_{-\infty}^{\infty} A_0^2 |\text{sech} \frac{t}{\tau}|^2 dt \tag{8.5}$$

$$= \frac{\alpha_{TPA} L}{w_0} A_0^2 \frac{4}{3} \tau \tag{8.6}$$

We recall from chapter 2 that the pulse energy is related to the amplitude and pulse width by the relation

$$w_0 = 2 A_0^2 \tau \tag{8.7}$$

Substituting in (8.5), the time-averaged loss (absorption) is given by

$$\tilde{q}_{TPA} = \frac{\beta A_{Struct} L}{3 A_{Eff}} \frac{w_0}{\tau} \tag{8.8}$$

For a given TPA semiconductor sample, the absorption is proportional to the product of the average pulse energy times the interaction length, and inversely proportional to the pulse width.

8.3 Semiconductor Mirror Structures

The TPA semiconductor mirror used for the experiments is shown in Fig. 8-2[2]. The mirror consists of a bulk 5.2 μm InP layer (22 $\lambda/2$ layers) deposited by gas source molecular beam epitaxy onto a 22-period GaAs/AlAs distributed Bragg reflector (> 99% reflectivity over 100 nm, centered at 1.55 μm). A dielectric antireflection coating ($\lambda/4$) is deposited onto the structure (following the epitaxial growth) to enhance the field in the InP. The structure exhibits only TPA and free-carrier absorption (FCA) in the InP layer, and the structure is designed for normal incidence. Because of the very thick InP layer, the horizontal axis of the plot is broken so as to include the major features of the semiconductor mirror structure. The engineering and design of the structure were detailed in previous thesis work[121][122].

To characterize the structure, time-averaged reflectivity measurements were performed using a wavelength-tunable synchronously-pumped optical parametric oscillator (OPO) with ~150 fs pulses at 82 MHz repetition rate. The reflectivity measurements were not performed on the structure of Fig. $8-2$ but were done on a very similar structure[4] with a smaller InP region ($\lambda/2$) and two InGaAs quantum wells within ~15 nm from the top layer surface. For the reflectivity measurements, the position of the quantum wells corresponded to the nulls of the electric field, and the wavelength of the OPO was ~90 nm below the bandedge of the quantum wells, thus minimizing the effects of the quantum wells. Reflectivity measurements for that structure are shown in Fig. $8-3$ to demonstrate the TPA effect in the InP. The fluence was changed by varying the average power, pulse width, and spot size incident on the semiconductor sample.

At low fluence, the structure acts as a linear dielectric mirror with $\sim$ 99.6% reflectivity, indicating that the DBR stack and material was of high quality with low non-saturable losses. At higher fluences, the reflectivity rapidly rolled off in a manner consistent with TPA. The solid line was fit using a simple model given by

$$R(t) = 1 - \beta A_{Struct} L I(t) + \alpha_0 \tag{8.9}$$

where $R(t)$ is the instantaneous reflectivity, t is time on the scale of the pulse width, $I(t)$ the

[2]The semiconductor structures were grown by Elizabeth Koontz.

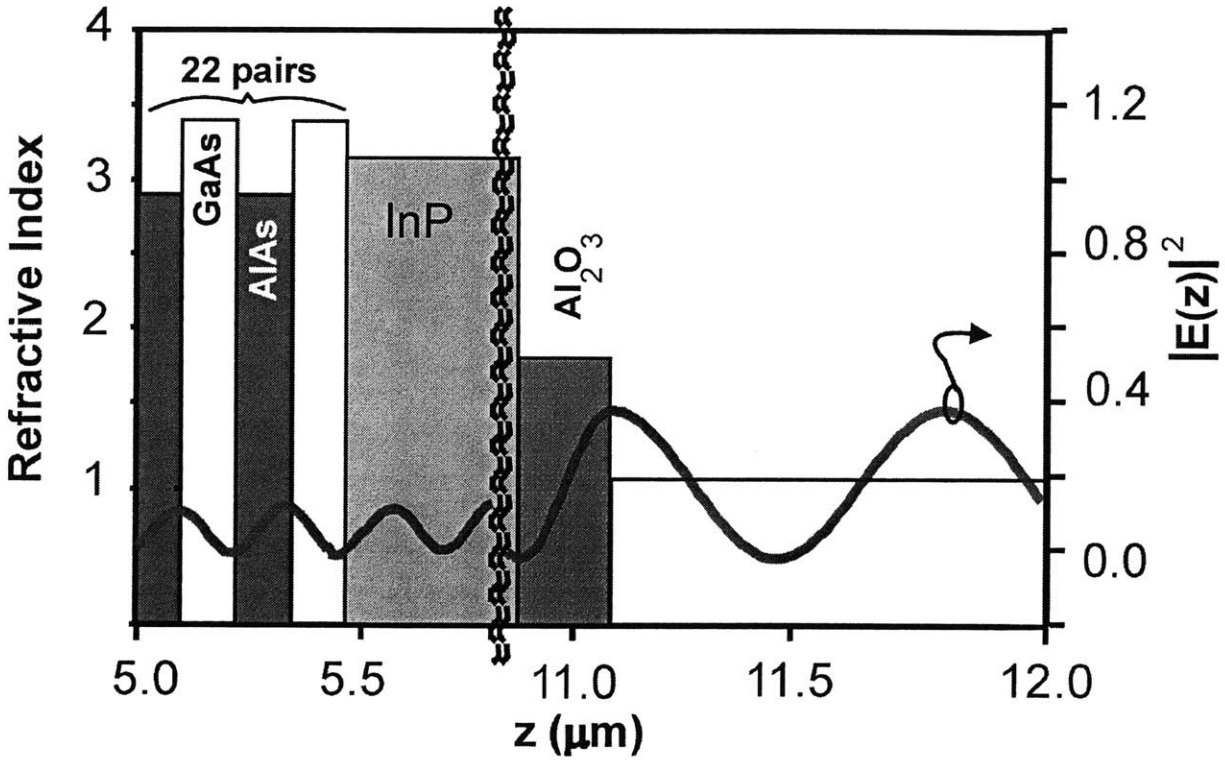

Figure 8-2: Schematic of an anti-reflection-coated semiconductor structure and distributed Bragg reflector stack, sample # SBR5AR. The refractive index and magnitude squared of the electric field ($\lambda = 1.54\ \mu m$, incident from the left-hand side) are plotted as a function of distance from the GaAs substrate-DBR interface. The scale of the plot is adjusted so as to include the major features of the structure.

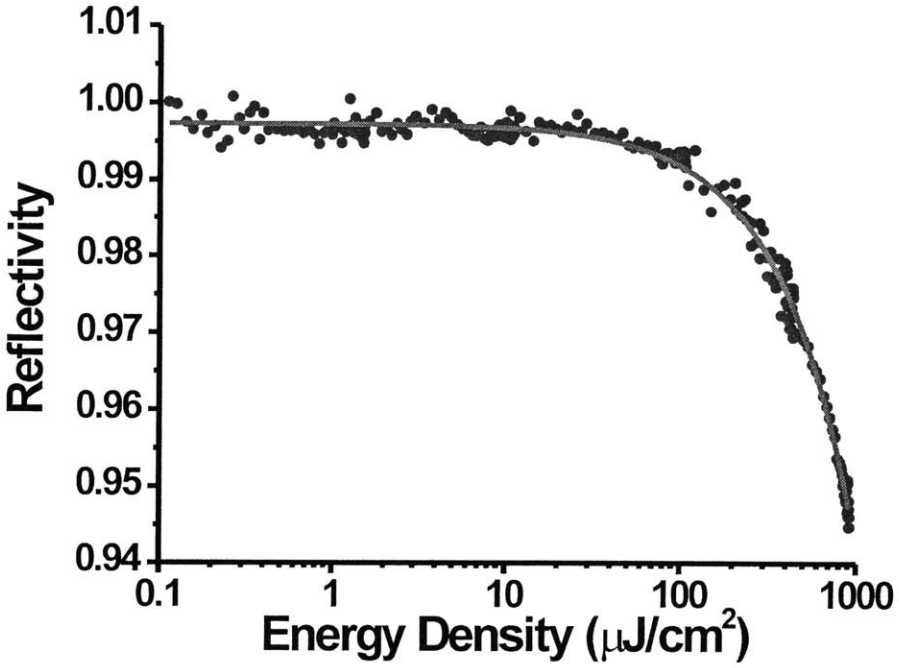

Figure 8-3: Time-averaged reflectivity measurements of a similar semiconductor mirror structure with one $\lambda/2$ InP layer using 150 fs pulses at 1.54 μm from a synchronously-pumped optical parametric oscillator at 82 MHz as a function of fluence. Figure appears in Ref. [4].

instantaneous pulse intensity (assuming a Gaussian pulse shape), β the TPA coefficient, A_{Struct} a structural factor accounting for the field distribution determined by the dielectric coating and the DBR, L the thickness of the TPA region, and α_0 the non-saturable loss.

To determine the nature of the nonlinear reflectivity measurements, pump-probe reflectivity measurements were performed[3] on the structure of Fig. 8-2 to be used in the experiment. The pump-probe measurements were performed using a ~150 fs pulses at 1.55 μm from an OPO with an 82 MHz repetition rate in a cross-polarized, collinear arrangement in which the differential reflectivity of the probe was monitored as a function of the probe delay. Figure 8-4 shows an array of non-normalized traces corresponding to a variety of fluence levels. At low fluences, the dominant feature of the trace is the instantaneous change of the nonlinear reflectivity at zero delay. This is the pump-pulse-induced TPA as observed by the probe when the two pulses overlap. The width of the trace corresponds to that of the cross correlation between the pump and probe pulses, consistent with the instantaneous TPA response. As the fluence was increased (by increasing the focusing and/or the average power), a longer-lived feature appears with a time constant ~6-8 ps appears and is much longer than the time scale of the pump and probe pulse widths. This is explained by the creation of a large number of free-carriers in the conduction band by the strong pump pulse, and these free carriers can absorb single photons from the probe, resulting in a change of the probe reflectivity[123]. This free carrier absorption (FCA) takes place until the carriers recombine (interband process). While in pure semiconductor materials this can take on the order of nanoseconds, defects in the semiconductor mirror structure create recombination centers in the InP that speed up the recovery time. Defects can be intensionally introduced by a number of mechanisms, including low-temperature growth[124][125] and proton bombardment[117]. However, increasing the defect density can also lead to unwanted nonsaturable losses and an additional time constant due to photoinduced absorption due to carriers trapped in defect states[126][127]. While both TPA and FCA result in nonlinear losses that increase with higher intensity, the carriers generated by FCA must recombine at a time scale much faster than the repetition rate in order for it to be useful in a high repetition rate laser; else, the fluence will need to be reduced to a level such that the free carrier contribution is negligible.

[3]Time-resolved pump-probe measurements were performed by Juliet Gopinath.

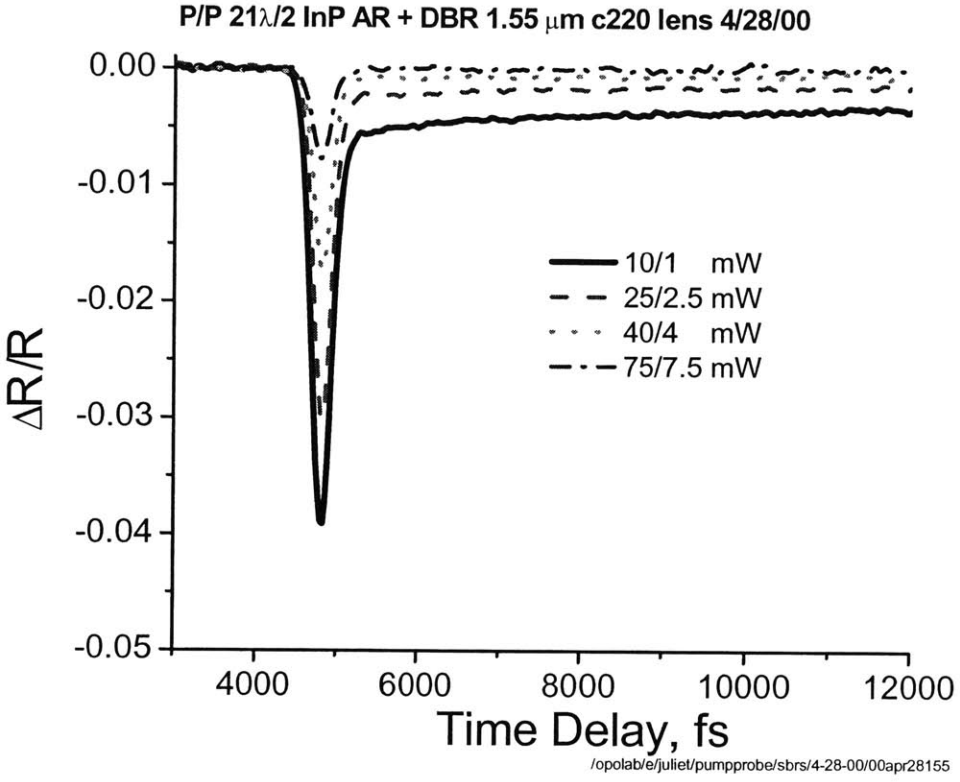

Figure 8-4: Time resolved nonlinear reflectivity measurements of the TPA semiconductor mirror structure as a function of fluence for various pump-to-probe power levels. Data provided by Juliet Gopinath.

8.4 Experiments

To test the effect of TPA in a harmonically modelocked fiber laser, we designed the laser shown in Fig. 8-5 to eliminate the stabilizing effect of additive-pulse limiting or SPM and filtering. The cavity consists of polarization-maintaining PANDA-type fiber (including the pigtails of all devices) to eliminate additive-pulse limiting effects. To minimize the effects of SPM and filtering, the cavity length was reduced to ~47 m (fundamental cavity frequency ~4.3 MHz), and a wide 20-nm tunable interference filter is used to shift the operating wavelength away from the sharp gain peak near 1530 nm. The cavity includes a circulator with a collimator to permit insertion of a normal-incidence mirror. Aspheric lenses with various focal lengths are added following the collimator to control the spot size on the mirror. The average group-velocity dispersion of the cavity is ~6 ps/nm/km and anomalous. The laser is modelocked at the ~465th cavity harmonic with a $LiNbO_3$ amplitude modulator driven by a rf synthesizer (HP 83732B) near 2 GHz. The entire laser, with the exception of the amplitude modulator, focusing lens, and dielectric end mirror or TPA mirror structure, were placed in a temperature-controlled, resistively-heated metal box to reduce thermal drift of the cavity. Over the time scale of these experiments, we found that no electronic stabilization of the cavity length (using a fiber-wound PZT, for example) referenced to the synthesizer frequency was necessary.

8.4.1 Modelocking in a Short Cavity Without TPA

Initially, the TPA mirror was placed in the laser cavity without a focusing lens, thus producing a large spot size (~9.5 x 10^{-3} cm^2) and created negligible TPA based on nonreflectivity measurements of a similar structure[4], shown in Fig. 8-3. The 20-nm filter was adjusted such that the laser operated at ~1555 nm. The output power from the 10% coupler was ~164 μJ, and the laser produced clean, transform-limited 980 fs hyperbolic secant pulses–as expected for soliton pulse shaping–with a spectral full-width-at-half-maximum (FWHM) of 2.65 nm. The second-harmonic-generated (SHG) autocorrelation (noncollinear, background-free) is shown in Figs. 8-6 and the optical spectrum in Fig. 8-7. While the autocorrelation and optical spectrum is clean, the absence of stabilization is revealed in the RF spectrum of the directly detected photogenerated current, as shown in Fig. 8-8. The suppression of sidemodes is only on the

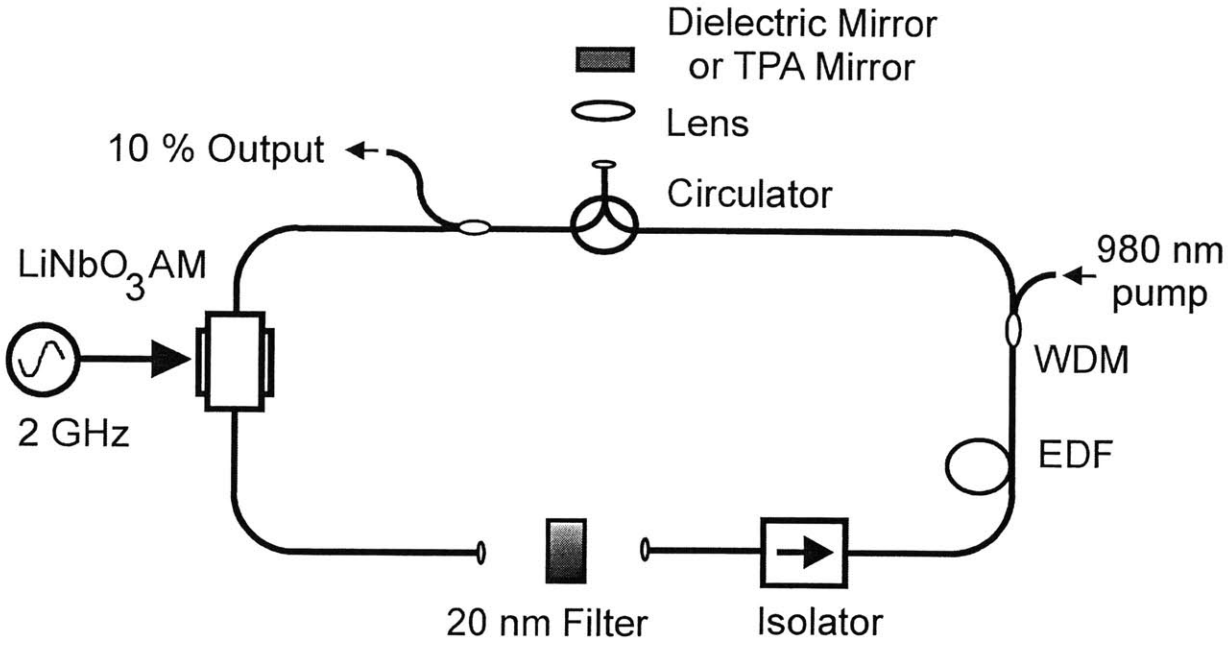

Figure 8-5: Schematic of an actively modelocked fiber ring laser for stabilization studies; WDM wavelength-division multiplexer for the 980 nm pump; EDF erbium-doped fiber.

order of 25-30 dB, indicative of massive pulse dropouts and/or large amplitude fluctuations. Qualitatively, this is not enough to determine the amount of amplitude and timing fluctuations. However, the pulse pattern can directly be observed on an oscilloscope, as shown in Fig. 8-9. While the sampling rate of 5 Gs/s is not fast enough to reveal each time slot (pulse-to-pulse separation of 0.5 ns), the entire pattern can be viewed in time where the pattern length is just one roundtrip time, or 235 ns. The 300 ns span of the trace of Fig. 8-9 reveals shows the pattern repeating itself. The oscilloscope trace reveals that there are large numbers of pulse dropouts and distribution of amplitudes amongst pulses in the pattern. The data from the oscilloscope trace was obtained with direct triggering from the 2 GHz synthesizer. The stability of the pattern indicated that the particular configuration of amplitudes and dropouts in the figure was not transient. Perturbing the cavity (by turning off the 2 GHz synthesizer and remodelocking, adjusting the bias voltage, or changing the cavity loss) resulted in a the formation of a new pattern, but once formed would be maintained over a period of tens of seconds to minutes.

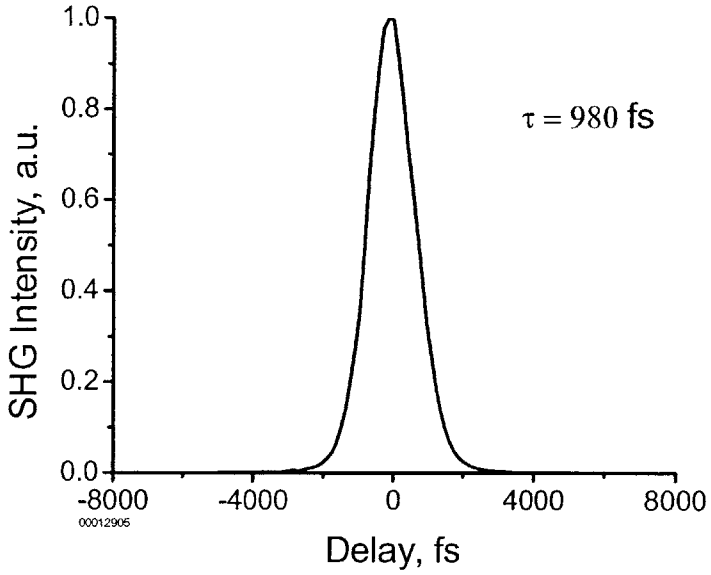

Figure 8-6: Non-collinear, background-free autocorrelation trace for the case without the TPA mirror structure. Pulse width is the full-width-at-half-maximum of a hyperbolic secant pulse shape.

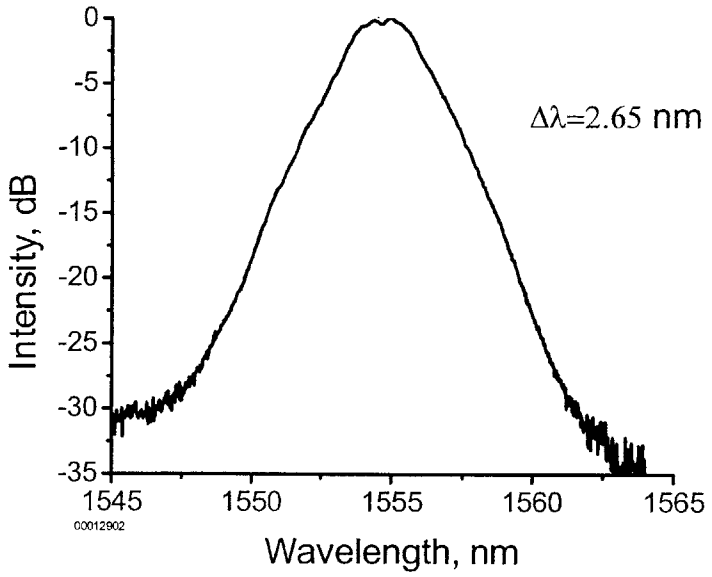

Figure 8-7: Optical spectrum (log scale) for the case without the TPA mirror structure.

8.4.2 Modelocking in a Short Cavity With TPA

An aspheric lens with a 4.5 mm focal length, N.A. 0.55 (ThorLabs C230) was inserted to produce a small spot size of $\sim 5 \text{x} 10^{-8}$ cm^2 on the TPA semiconductor mirror structure. In making room for the addition of the lens and lens-adjusting translation stages in the cavity, the cavity length was slightly increased to 4.35 MHz. The filtering (20 nm), lasing wavelength (1555 nm), modulation depth (corresponding to +29 dBm before the bias tee and biasing circuit) and average power (164 μJ) were all kept constant in order to compare the case with and without the lens. The incident pulse energy on the absorber was $\sim$2.8 pJ, and the calculated fluence based on the spot size and average power was ~ 56 $\mu J/\text{cm}^2$.

The resulting autocorrelation and optical spectrum are shown in Figs. 8-10 and 8-11, respectively. Compared to the case without TPA, the pulses broadened by a factor greater than two (from 980 fs to 2.4 ps), and the spectrum correspondingly narrowed (from 2.65 nm to 1.4 nm). The explanation for the pulse broadening is that because shorter pulses have larger peak power (and, hence, larger fluence) than longer pulses focussed into the TPA region, the

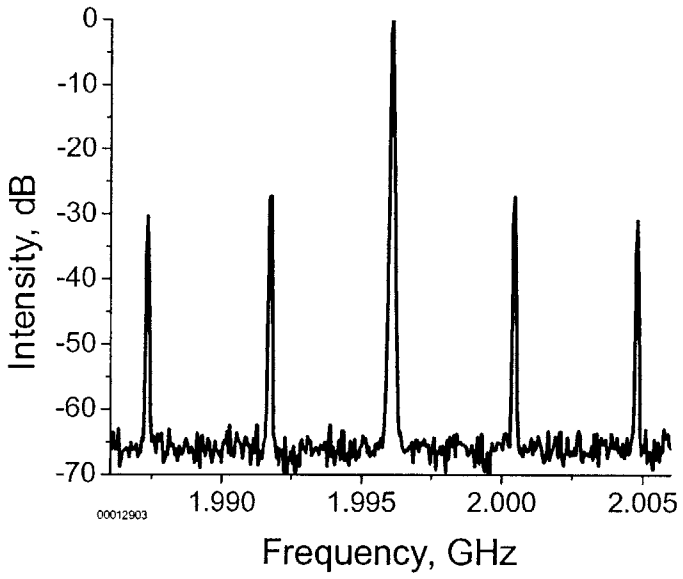

Figure 8-8: RF spectrum (log scale) for the case without the TPA mirror structure. The supermode suppression is > 25 dB.

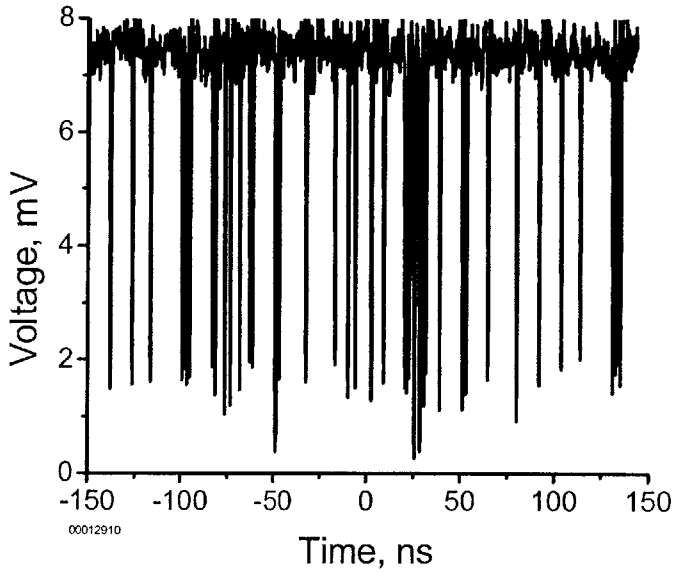

Figure 8-9: Oscilloscope trace of the directly-detected laser pulse train (sampling rate of 5 Gsamples/s) for the case without the TPA mirror structure. Individual time slots can not be resolved, but massive pulse dropouts and various pulse amplitudes can be observed.

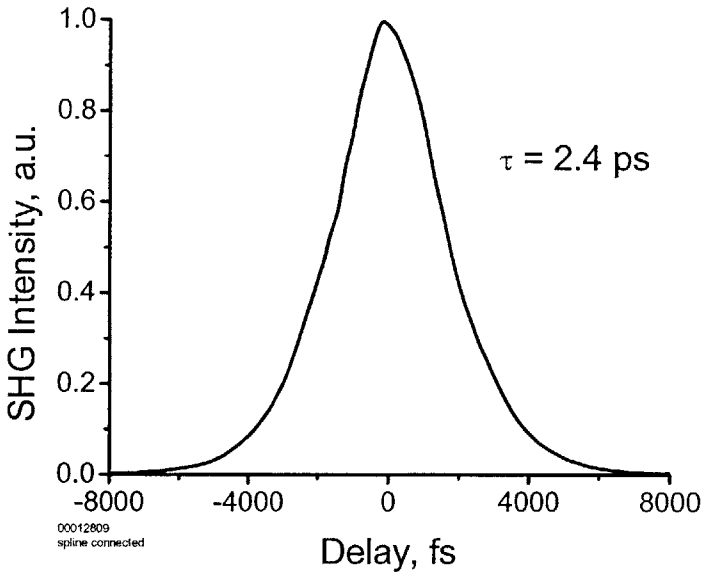

Figure 8-10: Non-collinear, background-free autocorrelation trace for the case with the TPA mirror structure. Pulse width is the full-width-at-half-maximum of a hyperbolic secant pulse shape.

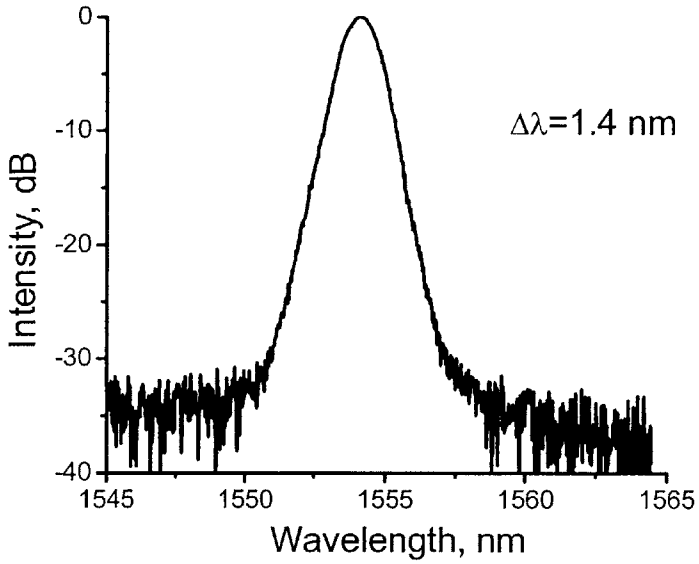

Figure 8-11: Optical spectrum (log scale) for the case with the TPA mirror structure.

shorter pulses experience more loss than longer pulses. This extra induced loss favors the formation of longer pulses.

A spectrum of the directly-detected photogenerated current is shown in Fig. 8-12. The supermodes are suppressed by an additional 25-30 dB as compared to the case without TPA stabilization. A trace from a real-time digital oscilloscope is shown in Fig. 8-13. Again, because of the limited sampling rate of the scope (5 GS/s), individual time slots of 0.5 ns width cannot be resolved. The traces do not show evidence of either amplitude fluctuations at levels > 2.8 % nor any pulse dropouts. The choppiness of the trace is due to the noise of the oscilloscope, as shown by the lower trace in which the optical input to the photodetector preceding the oscilloscope was blocked and the fluctuations measured. As shown on the figure, both traces fluctuated by approximately the same amount.

Another interesting feature of the oscilloscope plot is the conservation of area: while the average power for each case (with and without the TPA mirror structure) was held to be approximately constant, the maximum detected voltage level of the oscilloscope for the case without TPA in Fig. 8-9 of 7.8 mV is much higher than the 6.4 mV level for the case with

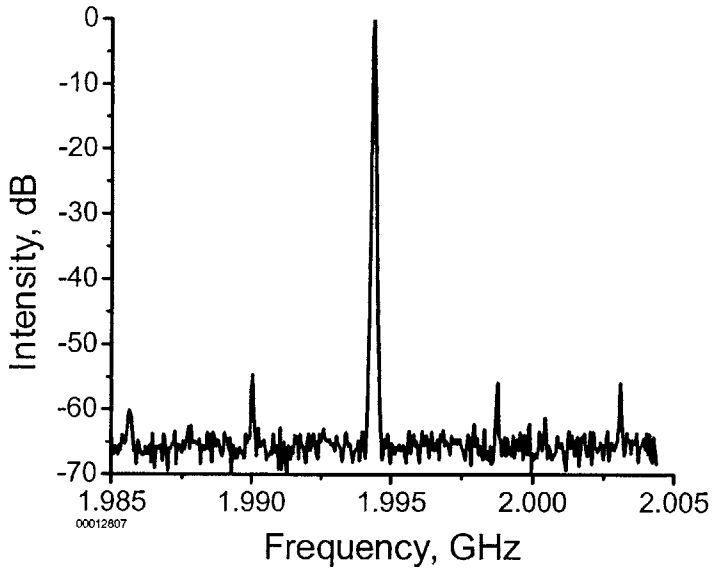

Figure 8-12: RF spectrum (log scale) for the case with the TPA mirror structure. The supermode suppression has been improved (compared to the case without the TPA sample) to > 55 dB.

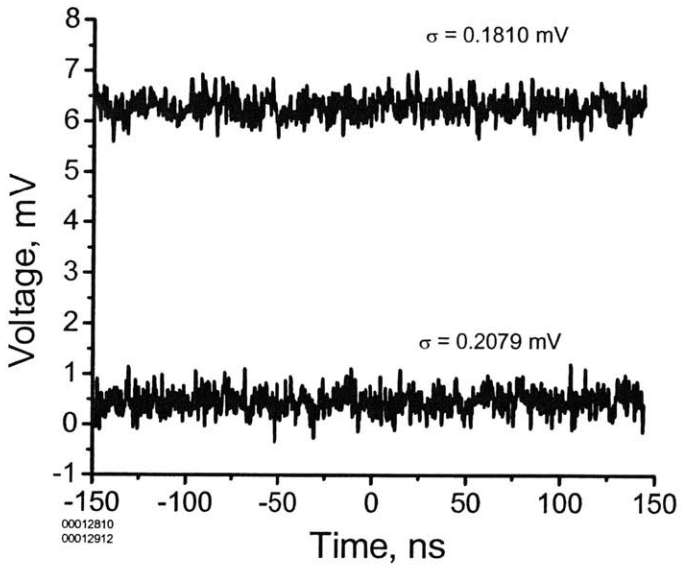

Figure 8-13: Oscilloscope trace of the directly-detected laser pulse train (sampling rate of 5 Gsamples/s) for the case with TPA mirror structure. The lower trace is a measure of the instrument noise, obtained while blocking the optical input to the photodetector. The sigma values given are for the amplitude deviations of the voltage level and determined by the instrument noise, not laser amplitude-noise fluctuations.

TPA in Fig. 8-13. This is due to the fact that while the peak detected power level is the same as the average for Fig. 8-13, the large number of dropouts for the case without TPA indicates that in order to maintain the same average power, the peak voltage level must be higher than the average of 6.9 mV.

In order to further test for the stability enhancement due to TPA, we removed the TPA mirror from the cavity and inserted a standard dielectric mirror which did not exhibit TPA at normal incidence while keeping in the 4.5 mm aspheric focusing lens in the cavity. The results obtained were identical to those shown as for the case with the TPA mirror structure and large defocusing[116].

The nonlinear loss of TPA was estimated by use of a TPA coefficient of 90 cm/GW for InP[128] and integration over the standing-wave field present in the TPA mirror. For the estimated intracavity intensity in the absorber, the induced nonlinear loss was estimated to be 0.5%-1.0%. This estimate agrees with experiments performed externally on a similar structures[4] for the fluence estimated to be present in the TPA mirror structure. To test for the presence of FCA, external measurements of the time-resolved nonlinear reflectivity measurements (same setup used to collect the data from Fig. 8-4) of the TPA mirror structure were performed. In that experiment, the fluence level was increased until the maximum nonlinear-induced loss reached between 0.5%-1.0% and shown in Fig. 8-14. For this level of nonlinear loss, only the TPA response is seen, and no FCA is observed. Thus, the nonlinear mechanism responsible for the elimination of pulse dropouts was TPA.

8.5 Discussion

The evidence presented here proves the efficacy of TPA as a mechanism for stabilizing against pulse dropouts. We showed that by incorporating a TPA mirror structure in the fiber laser cavity that pulse dropouts could be eliminated. Time resolved pump-probe traces revealed that the mechanism causing nonlinear loss was entirely due to TPA and not due to absorption caused by the generation of free carriers.

Using TPA to stabilize a harmonically modelocked laser offers some advantages over other methods. Because the nonlinearity required for peak intensity limiting is contained in a thin

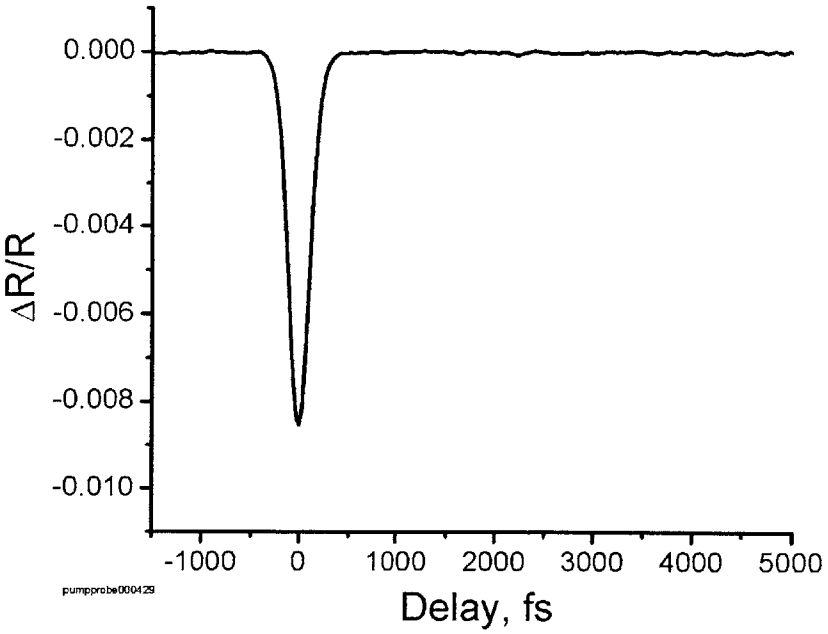

Figure 8-14: Pump-probe trace with C220 (11 mm) aspheric lens at a fluence level necessary to produce a maximum nonlinear reflectivity change between 0.5% and 1.0%. Figure reproduced from Ref. [5].

semiconductor layer, stabilization of short cavities is possible. The TPA mirror structure's small size, compared with hundreds of meters of fiber, makes it much less sensitive to environmental changes, and the mirror can easily be incorporated into polarization-maintaining or sigma-type laser cavities. Because the TPA depends on the peak intensity, it is effective regardless of the group-velocity dispersion in the laser, thus it should be possible to stabilize a harmonically modelocked laser that operates in with normal average GVD. Because most semiconductors exhibit TPA over a broad wavelength range, TPA mirror structures can be used in variety of laser systems over a large selection of operating wavelengths.

8.6 Ideas for Future Work

Using a passive InP waveguide should allow for better stabilization by overcoming diffraction-limited focussing experienced in bulk InP. Other nonlinear-induced loss mechanisms can be employed in to achieve stabilization, including semiconductor optical amplifier waveguide employing TPA in an SOA waveguide designed for 1.3 μm.

Also, one could use a nonlinear crystal for second-harmonic generation (SHG). The amount of signal converted to SHG is filtered out of the laser (by an optical filter and by the limited gain bandwidth) and results in an intensity-dependent loss. We can compare the efficiency of SHG-induced loss to that of TPA-induced loss. Writing the transmission for the input and output intensities $I_{in}(t)$ and $I_{out}(t)$,

$$\begin{aligned} I_{out} &= I_{in} - I_{2\omega} && (8.10)\\ &= I_{in} - \eta_{SHG} {I_{in}}^2 && (8.11)\\ I_{out}/I_{in} &= T = 1 - \eta_{SHG} I_{in} && (8.12) \end{aligned}$$

where $T(t)$ is the instantaneous transmission through the SHG sample, t is time on the scale of the pulse width, $I(t)$ the instantaneous pulse intensity (assuming a Gaussian pulse shape), L the thickness of the SHG region, and η_{SHG} the SHG coefficient in units of cm^2/W and given by

$$\eta_{SHG} = \frac{2\omega^2 d_{eff}^2 L_{SHG}^2}{n_{2\omega} n_\omega^2 c^3 \varepsilon_0} \qquad (8.13)$$

For TPA,

$$\begin{aligned} I_{out} &= I_{in}\exp\left(-\beta_{TPA}L_{TPA}I_{in}\right) \\ &\simeq I_{in}(1-\beta_{TPA}L_{TPA}I_{in}) \\ T &= 1-\beta_{TPA}L_{TPA}I_{in} \end{aligned}$$

So, we find that the ratio of SHG- to TPA-induced loss is

$$\begin{aligned} \frac{SHG\text{ loss}}{TPA\text{ loss}} &= \frac{\eta_{SHG}I_{in}}{\beta_{TPA}L_{TPA}I_{in}} \\ &= \frac{2\omega^2 d_{eff}^2 L_{SHG}^2}{n_{2\omega}n_{\omega}^2 c^3 \varepsilon_0}\cdot\frac{1}{\beta_{TPA}L_{TPA}} \\ &\sim \frac{1}{10^{-17}Fm/s}\cdot\frac{d_{eff}^2 L_{SHG}^2}{\beta_{TPA}L_{TPA}} \end{aligned}$$

where we have set $n_{2\omega}\sim n_{\omega}$, $\varepsilon_0 = 8.85\times10^{-12}F/m$, and $\lambda = 1.55\mu m$. Taking some typical numbers for $d_{eff}\sim 12\times10^{-12}m/V$ (approximate value for POM), $\beta_{TPA}\sim 90cm/GW$ in InP,

$$\frac{SHG\text{ loss}}{TPA\text{ loss}} \sim \frac{1}{2}\frac{L_{SHG}^2}{L_{TPA}} \tag{8.14}$$

where L_{SHG} and L_{TPA} are in meters. For $L_{SHG}\sim 1\times10^{-3}$ m, $L_{TPA}\sim 21\ \lambda/2\sim 5\ \times10^{-6}$ m, the ratio of SHG loss to TPA loss is ~ 0.1, which suggests that SHG in a short POM nonlinear crystal would not be as effective as TPA for the device structure shown here. However, recent advances in periodically-poled $LiNbO_3$ waveguides, for example, achieving very high conversion efficiencies using quasi phase matching and could enable large nonlinear losses (large L_{SHG}) for preventing dropouts in relatively small, fiber-coupled package[129].

Chapter 9

Conclusions

This thesis has described many achievements towards building an understanding of the timing jitter and stability of active harmonically modelocked soliton fiber lasers. A comprehensive semi-classical theory of the noise using soliton perturbation theory was presented, and the equations of motion governing pulse retiming dynamics were derived for the case of ASE-limited noise. It was shown how the ASE leads to fluctuations in the pulse timing and pulse carrier frequency (which lead to timing fluctuations through GVD). It was shown that while the characteristics of the steady-state modelocked pulses for amplitude and phase modulation are similar, the forces governing pulse retiming are rather different. For AM, mistimed pulses are retimed directly, whereas for PM, mistimed pulses are retimed through a second-order process involving carrier-frequency shifts that translate to timing shifts through GVD. The retiming dynamics for PM were shown to be similar to that of a classical damped harmonic oscillator whose qualitative character could be changed from overdamping to underdamping depending on the relative strengths of filtering and carrier frequency shifting. A set of characteristic coefficients describing the retiming dynamics for AM and PM were derived. The equations of motion and spectra of the timing jitter were derived for AM and PM, and the features of the spectra were described in terms of the characteristic coefficients. Analytical solutions of the integrated timing jitter were found for AM and PM. For AM, the Gordon-Haus contribution to the jitter (in units of time) is proportional to the square of the filter bandwidth and directly proportional to GVD. For low GVD, the jitter for AM is minimized to a value inversely proportional to the square-root of the product of modulation depth and modulation frequency

squared and directly proportional to the noise-to-signal ratio in the cavity. For PM, the Gordon-Haus jitter is proportional to the filter bandwidth and to the square root of GVD–in comparison to AM, the Gordon-Haus jiiter for PM is smaller because the GVD helps to retime pulses. The portion of the jitter due to direct pulse mistiming is inversely proportional to the product of the square root of GVD and filter bandwidth, indicating that GVD is necessary for PM in order to retime pulses that have been mistimed. Thus, for PM there exists an optimum GVD that minimizes the Gordon-Haus jitter while also minimizing the jitter due to direct pulse mistiming. The minimum jitter for PM is inversely proportional to the square-root of the product of modulation depth and modulation frequency squared and directly proportional to the noise-to-signal ratio in the cavity.

A high-performance polarization-maintaining harmonically modelocked fiber ring laser near 1555 nm generating picosecond pulses at 10 GHz with $>$ 65 dB supermode suppression was shown. An apparatus for directly measuring the predicted characteristic constants (and for observing the pulse retiming dynamics in real time) was constructed, and the measured constants for both AM and PM were shown to agree with the theory.

Timing jitter measurements were performed on a sigma-type active harmonically modelocked fiber laser driven with a low-noise local oscillator. A dual-channel residual phase-noise measurement setup using homodyne detection was shown. The measured spectra of the quantum-limited timing jitter for the cases of AM and PM were described. It was shown that the measured spectra agreed both qualitatively and quantitatively with the theory. A theory for the timing jitter of a harmonically modelocked laser was derived, and it was shown that the timing jitter spectra of the supermodes depend on the pulse-to-pulse noise correlations within the pulse pattern. It was shown that the measured timing jitter spectra of the supermodes were identical, in agreement with the case for which the pulses in the harmonically modelocked laser cavity are uncorrelated. It was also shown that the spectra of the supermodes must be included in the evaluation of the timing jitter by comparing the the residual phase-noise measurements with optical cross correlations.

It was shown theoretically that, using phase modulation and GVD in two section of fiber external to the laser cavity, the timing jitter of a train of pulses can be reduced, but only at the expense of the carrier frequency jitter.

Finally, experiments were shown demonstrating that two-photon absorption in a semiconductor mirror structure can be used to stabilize against pulse dropouts in a short harmonically modelocked laser.

Appendix A

Full Expression for the Spectrum of Pulse Timing

The complete expression for the pulse timing, including the cross-correlation terms between the noise projections, is given for AM and PM:

$$\begin{aligned}\left\langle |\Delta T(\Omega)|^2 \right\rangle_{AM} = \frac{1}{\frac{1}{\tau_{AM}^2}+\Omega^2}\Bigg\{ & \left(\frac{g}{\Omega_f w_0}\frac{1}{T_R}\right)^2 \frac{\left\langle |S_w(\Omega)|^2 \right\rangle}{\left(\frac{1}{\tau_w^2}+\Omega^2\right)} \\ & + \left(\frac{g}{\Omega_f w_0}\frac{1}{T_R}\right)\left(2|D|\frac{1}{T_R}\right)\left[\frac{\left\langle |S_w(\Omega)S_p^*(\Omega)| \right\rangle}{\left(\frac{1}{\tau_w}-j\Omega\right)\left(\frac{1}{\tau_p}+j\Omega\right)}\right. \\ & \left. + \frac{\langle |S_w^*(\Omega)S_p(\Omega)| \rangle}{\left(\frac{1}{\tau_w}+j\Omega\right)\left(\frac{1}{\tau_p}-j\Omega\right)}\right] + \left(2|D|\frac{1}{T_R}\right)^2 \frac{\left\langle |S_p(\Omega)|^2 \right\rangle}{\left(\frac{1}{\tau_p^2}+\Omega^2\right)} \\ & + \left(\frac{g}{\Omega_f w_0}\frac{1}{T_R}\right)\left[\frac{\langle |S_w(\Omega)S_T^*(\Omega)| \rangle}{\left(\frac{1}{\tau_w}+j\Omega\right)} + \frac{\langle |S_w^*(\Omega)S_T(\Omega)| \rangle}{\left(\frac{1}{\tau_w}-j\Omega\right)}\right] \\ & + \left(2|D|\frac{1}{T_R}\right)\left[\frac{\langle |S_p(\Omega)S_T^*(\Omega)| \rangle}{\left(\frac{1}{\tau_p}-j\Omega\right)} + \frac{\left\langle |S_p^*(\Omega)S_T(\Omega)| \right\rangle}{\left(\frac{1}{\tau_p}+j\Omega\right)}\right] + \left\langle |S_T(\Omega)|^2 \right\rangle\end{aligned}$$

and

$$\left\langle |\Delta T(\Omega)|^2 \right\rangle_{PM} = \frac{\left(\frac{1}{\tau_p^2} + \Omega^2\right)}{\left[\Omega^4 + \Omega^2\left(\frac{1}{\tau_p^2} - 2\Omega_{PM}^2\right) + \Omega_{PM}^4\right]} * \left\{ \left(\frac{g}{\Omega_f w_0}\frac{1}{T_R}\right)^2 \frac{\left\langle |S_w(\Omega)|^2 \right\rangle}{\left(\frac{1}{\tau_{w'}^2} + \Omega^2\right)} + \left(\frac{g}{\Omega_f w_0}\frac{1}{T_R}\right) * \left(2|D|\frac{1}{T_R}\right) \left[\frac{\left\langle \left|S_w(\Omega)S_p^*(\Omega)\right|^2 \right\rangle}{\left(\frac{1}{\tau_{w'}} + j\Omega\right)\left(\frac{1}{\tau_p} - j\Omega\right)} + \frac{\left\langle |S_w^*(\Omega)S_p(\Omega)|^2 \right\rangle}{\left(\frac{1}{\tau_{w'}} - j\Omega\right)\left(\frac{1}{\tau_p} + j\Omega\right)} + \left(2|D|\frac{1}{T_R}\right)^2 \frac{\left\langle |S_p(\Omega)|^2 \right\rangle}{\left(\frac{1}{\tau_p^2} + \Omega^2\right)} + \left(\frac{g}{\Omega_f w_0}\frac{1}{T_R}\right) \left[\frac{\langle |S_w(\Omega)S_T^*(\Omega)| \rangle}{\left(\frac{1}{\tau_{w'}} + j\Omega\right)} + \frac{\langle |S_w^*(\Omega)S_T(\Omega)| \rangle}{\left(\frac{1}{\tau_{w'}} - j\Omega\right)} \right] + \left(2|D|\frac{1}{T_R}\right) \left[\frac{\langle |S_p(\Omega)S_T^*(\Omega)| \rangle}{\left(\frac{1}{\tau_p} + j\Omega\right)} + \frac{\left\langle \left|S_p^*(\Omega)S_T(\Omega)\right| \right\rangle}{\left(\frac{1}{\tau_p} - j\Omega\right)} \right] + \left\langle |S_T(\Omega)|^2 \right\rangle$$

Appendix B

Modulator Bias Circuit

The circuit used to bias the modulator is shown in Fig. B-1. The 10 GHz local oscillator (HP 83732B synthesizer) is divided in a 50/50 power splitter. In one arm, the bias tee is used to combine the 10 GHz LO and a DC bias voltage. In the other arm, a microwave phase shifter is used to impart an adjustable delay. With the phase shifter set to π, the voltages arriving at the modulator are out of phase. In this configuration (push-pull operation) with V_{bias} set to quadrature, the modulator acts as an amplitude modulator and does not impart any phase modulation to the optical signal. By adjusting the relative delay and power in each arm, the chirp of the modulator can be varied from zero (pure AM) to ± 1 (pure PM).

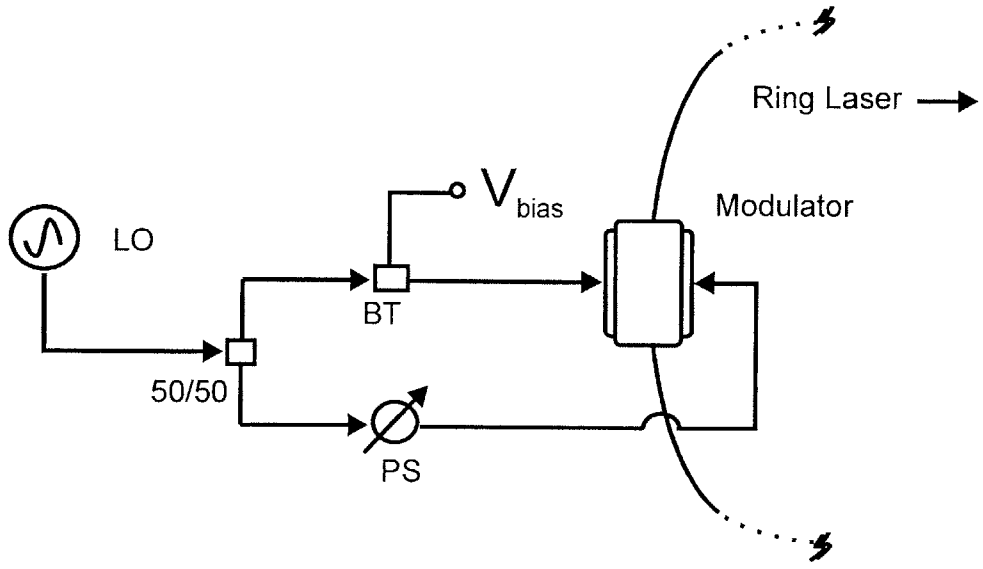

Figure B-1: Microwave bias control circuit to control the relative amounts of amplitude and phase modulation. LO is the microwave local oscillator, BT bias tee, V_{bias} bias voltage, PS microwave phase shifter.

Appendix C

Electronically-Controlled Microwave Phase Shifter

The microwave phase shifter is used to change the phase of the 10 GHz LO. The microwave phase switch is comprised of a single-throw double-pole two-port microwave switch and two microwave delay lines, as shown in Fig. C-1. The input voltage from the LO, V_{in}, is directed to either port A or port B, depending on the logic states of the TTL inputs V1 and V2, and the switch can only be in either state A or B. The phase accumulated by the V_{in} is different for the two paths as determined by the phase shifter such that $\phi_A - \phi_B = \phi_{kick}$ The switch logic is such that port A is connected when $V1 = 0$ and $V2 = 1$ (for TTL logic, logical "0" is 0 Volts and logical "1" is +5 Volts), and port B is connected when $V1 = 1$ and $V2 = 0$. Thus, in order to switch from one port to the other requires each $V1$ and $V2$ to be changed. While the intermediate states with $V1 = V2 = 0$ and $V1 = V2 = 1$ are not well defined, testing of the microwave switch showed that when the switch passes through the state $V1 = V2 = 1$, the switch goes unstable and rings for a period on the order of 50 ns. If the switch is initially in the B state, then $V1 = 1$ and $V2 = 0$. In order to switch to the A state, $V1$ must first be pulled down to zero and then $V2$ is pulled up to one. To achieve this, the control circuit shown in Fig. C-2 was designed. The desired rate at which the microwave switch is to flop between two phase states is given at a rate CLK. A delayed version of CLK is generated by propagating CLK through an AND gate with delay time t_{delay}. The outputs $V1$ and $V2$ are

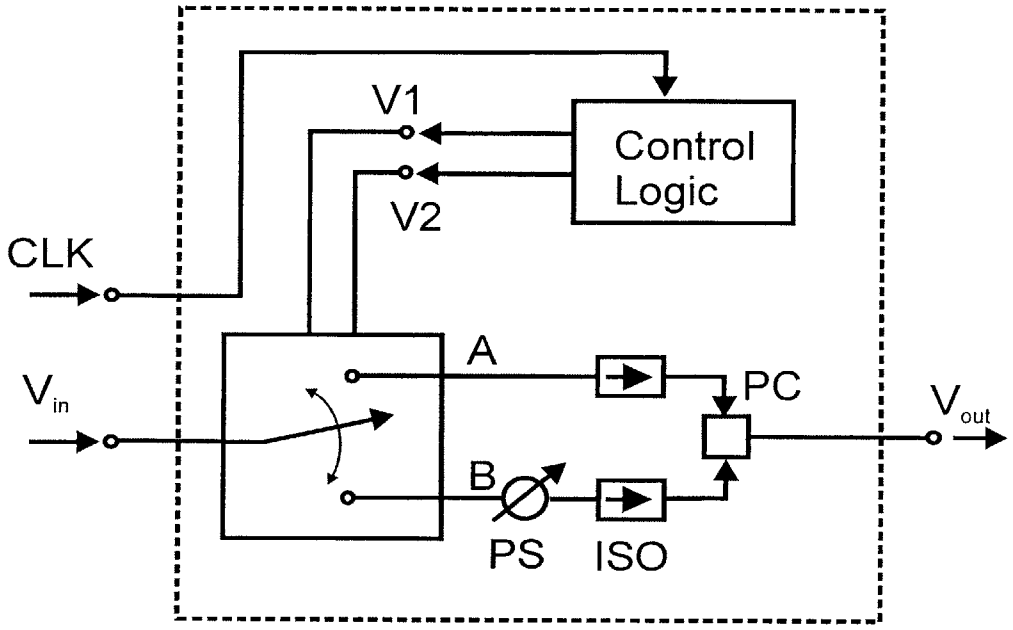

Figure C-1: Schematic of the electronically-controlled microwave phase shifter. CLK is the TTL input that sets the voltages V1 and V2 high or low. PS and ISO are microwave phase shifter and isolator, respectively, and PC is a power combiner. The phase of the output voltage V_{out} is determined by the relative phase diffference set between the two paths as determined by the microwave phase shifter.

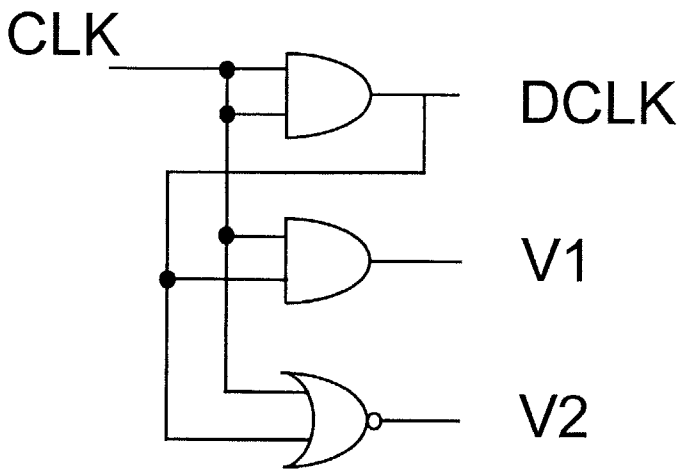

Figure C-2: Logic circuit to control the microwave switch. DCLK is a delayed version of CLK.

CLK	DCLK	V1	V2
0	0	0	1
1	0	0	0
0	1	0	0
1	1	1	0

Table C.1: Boolean logic table of microwave circuit controller.

given by the timing diagram of Fig. C-3 and obey the logic given in Table C.1. The reader can convince him(her)self that the circuit prevents both $V1$ and $V2$ going high at the same time. The resulting switching time in going from state A to state B (or state B to state A) was reduced to < 25 ns and shown in Fig. C-4.

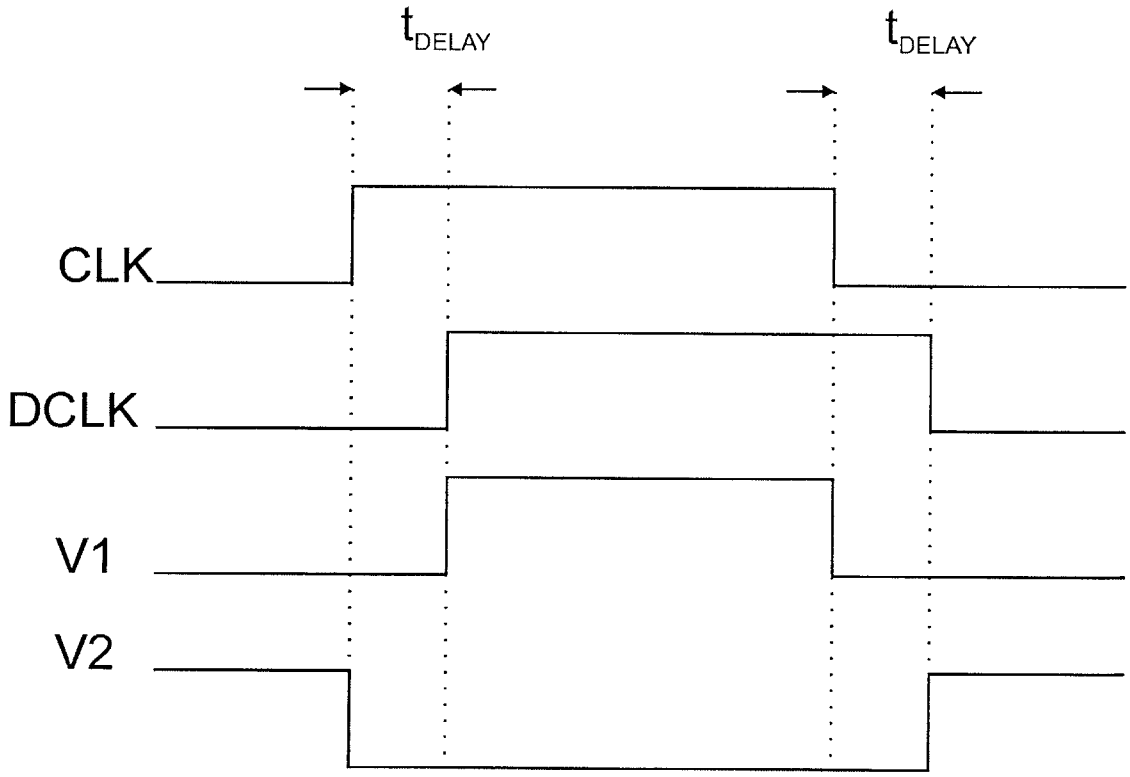

Figure C-3: Timing diagram for the logic circuit used to control the microwave single-pole double-throw switch. Delay through the AND gate (SN74S08) is 6 ns; delay through NOR gate (SN74S02) is 5 ns. The rising edge of V1 and falling edge of V2 follow the delayed clock DCLK, and the falling edge of V1 and rising edge of V2 follows CLK.

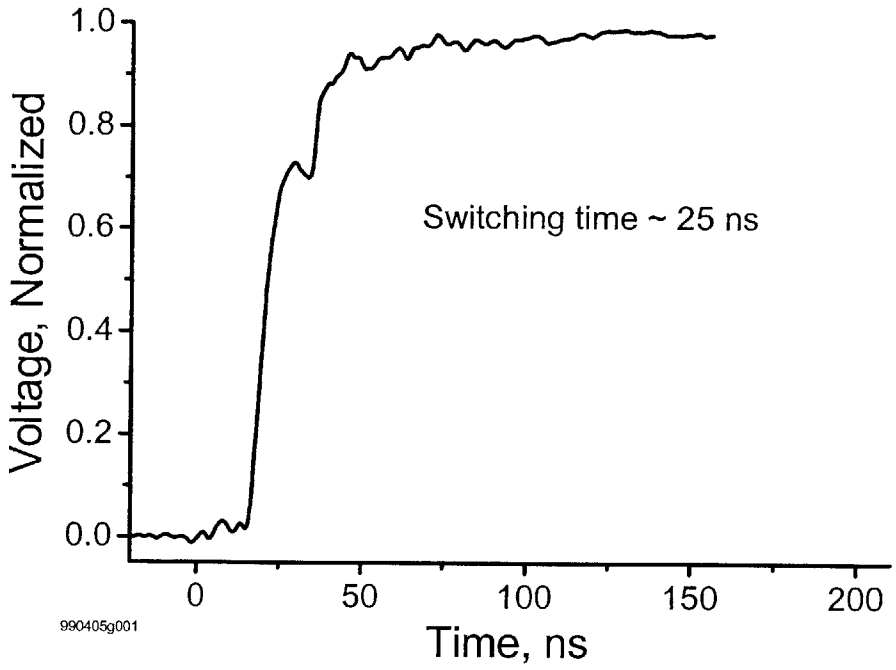

Figure C-4: Switching transient of the microwave switch that occurs when switching an input 10 GHz signal from port A to port B.

Appendix D

Circuits for Phase-Locked-Loop Control

The lead-lag circuits used for PLL control of the laser cavity are shown in Figs. D-1 and D-2.

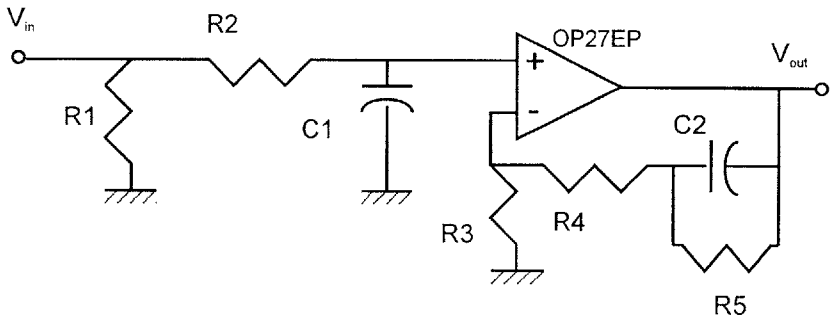

Figure D-1: Noninverting control circuit for laser stabilization. The parametere were $R_1 = 50\Omega$, $R_2 = 2.2M\Omega$, $C_1 = 0.2\mu f$, $R_3 = 10M\Omega$, $C_2 = 1.7\mu f$, $R_4 = 2.2M\Omega$, and $R_5 = 22M\Omega$. $R_5C_2 = 40$s refresh rate, circuit bandwidth < 8 Hz.

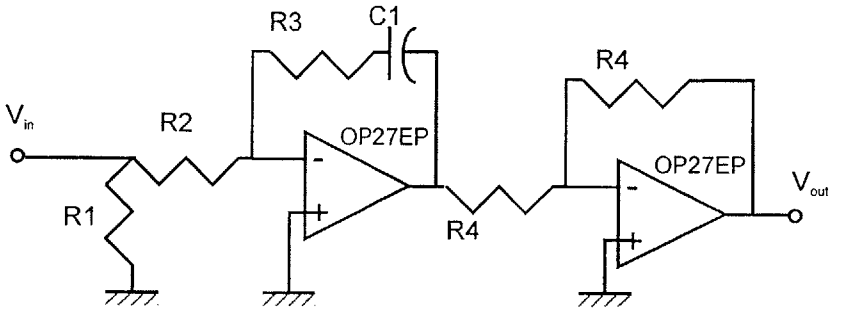

Figure D-2: Inverting control circuit for laser stabilization.

Bibliography

[1] R. H. Walden, "Analog-to-digital converter survey and analysis," *IEEE J. Select. Areas Commun.*, vol. 17, pp. 539–549, 1999.

[2] P. W. Juodawlkis, J. C. Twichell, G. E. Betts, J. J. Hargreaves, R. D. Younger, J. L. Wasserman, F. J. O'Donnell, K. G. Ray, and R. C. Williamson, "Optically sampled analog-to-digital converters," *IEEE Trans. Microwave Theory and Tech.*, vol. 12, pp. 1237–1239, 2000.

[3] J. D. Moores, W. S. Wong, and H. A. Haus, "Stability and timing maintainance in soliton transmission and storage rings," *Opt. Commun.*, vol. 113, pp. 153–175, 1994.

[4] E. R. Thoen, E. M. Koontz, M. Joschko, P. Langlois, T. R. Schibli, F. X. Kärtner, E. P. Ippen, and L. A. Kolodziejski, "Two-photon absorption in semiconductor saturable absorber mirrors," *Appl. Phys. Lett.*, vol. 74, p. 3927, 1999.

[5] J. T. Gopinath, "The effect of proton bombardment on semiconductor saturable absorber structures," Master's thesis, Massachusetts Institute of Technology, 2000.

[6] E. A. Swanson, R. Barry, D. M. Castagnozzi, V. Chan, K. Hall, *et al.*, "All-Optical Network Consortium," tech. rep., AT & T Bell Laboratories, Digital Equipment, Lincoln Laboratories, and Massachusetts Institute of Technology, 1995. ARPA-sponsored consortium.

[7] V. W. S. Chan, K. L. Hall, E. Modiano, and K. A. Rauschenbach, "Architectures and technologies for high-speed optical data networks," *J. Lightwave Technol.*, vol. 16, pp. 2146–2168, 1998.

[8] M. E. Grein, "A regeneratively modelocked fiber ring laser," Master's thesis, Massachusetts Institute of Technology, 1997.

[9] E. Yoshida and M. Nakazawa, "Measurement of the timing jitter and pulse energy fluctuation of a PLL regeneratively modelocked fibre laser," *IEEE Photon. Technol. Lett.*, vol. 11, p. 548, 1999.

[10] M. Nakazawa and K. Suzuki, "Cesium optical clock: an optical pulse that tells the time," *Opt. Lett.*, vol. 26, pp. 635–637, 2001.

[11] A. E. Siegman and D. J. Kuizenga, "Proposed method for measuring picosecond pulse widths and pulse shapes in cw mode-locked lasers," *IEEE J. Quantum. Electron.*, vol. 6, pp. 212–215, 1970.

[12] D. H. Auston, "Picosecond optoelectronic switching and gating in silicon," *Appl. Phys. Lett.*, vol. 26, pp. 101–103, 1975.

[13] H. F. Taylor, "An electrooptic analog-to-digital converter," *Proc. IEEE*, vol. 63, pp. 1524–1525, 1975.

[14] H. F. Taylor, "An electrooptic analog-to-digital converter–design and analysis," *IEEE J. Quantum. Electron.*, vol. 15, pp. 210–216, 1979.

[15] J. A. Bell, M. C. Hamilton, and D. A. Leep, "Optical sampling and demultiplexing applied to A/D conversion," *Devices for Optical Processing*, vol. 1562, pp. 276–280, 1991.

[16] J. A. Bell, M. C. Hamilton, D. A. Leep, H. F. Taylor, and Y. H. Lee, "A/D conversion of microwave signals using a hybrid optical/electronic technique," *Opt. Technol. Microwave Applicat. V*, vol. 1476, pp. 326–329, 1991.

[17] J. C. Twichell and R. Helkey, "Phase-encoded optical sampling for analog-to-digital converters," *IEEE Phot. Technol. Lett.*, vol. 12, pp. 1237–1239, 2000.

[18] P. W. Juodawlkis, J. C. Twichell, J. L. Wasserman, G. E. Betts, and R. C. Williamson, "Measurement of mode-locked laser timing jitter by use of phase-encoded optical sampling," *Opt. Lett.*, vol. 26, pp. 289–291, 2001.

[19] *DARPA/ETO Photonic A/D Converter Technology (PACT) Kick Off Meeting*, April 20-21 1999. MIT-Lincoln Laboratory, Lexington, MA.

[20] D. J. Kuizenga and A. Siegman, "FM and AM mode locking of the homogeneous laser-Pt.I:Theory," *IEEE J. Quantum Electron.*, vol. QE-6, pp. 694–708, 1970.

[21] D. J. Kuizenga and A. Siegman, "FM and AM mode locking of the homogeneous laser-Pt.II: Experimental results in a Nd:YAG laser with FM modulation," *IEEE J. Quantum Electron.*, vol. QE-6, pp. 709–715, 1970.

[22] H. Haken and M. Pauthier, "Nonlinear theory of multimode action in loss modulated lasers," *IEEE J. Quantum Electron.*, vol. QE-4, pp. 454–459, 1968.

[23] A. E. Siegman, *Lasers.* University Science Books, 1986.

[24] J. H. Sanders and E. S. Stenholm, eds., *Progress in Quantum Optics.* Pergamon, 1974.

[25] S. L. Shapiro, ed., *Ultrashort Light Pulses: Picosecond Techniques and Applications.* Springer-Verlag, 1977.

[26] C. V. Shank, E. P. Ippen, and S. L. Shapiro, eds., *Picosecond Phenomena.* Springer-Verlag, 1978.

[27] H. A. Haus, "A theory of forced mode locking," *IEEE J. Quantum Electron.*, vol. QE-11, pp. 323–330, 1975.

[28] A. Siegman and D. J. Kuizenga, "Modulator frequency detuing effects in the FM mode-locked laser," *IEEE J. Quantum Electron.*, vol. QE-6, pp. 803–808, 1970.

[29] A. Hasegawa and F. Tappert, "Transmission of stationary nonlinear optical pulses in dispersive dielectric fibers. I. Anomalous dispersion," *Appl. Phys. Lett.*, vol. 23, pp. 142–144, 1973.

[30] H. A. Haus, "Theory of modelocking with a fast saturable absorber," *J. Appl. Phys.*, vol. 46, p. 3049, 1975.

[31] O. E. Martinez, R. L. Fork, and J. P. Gordon, "Theory of passively mode-locked lasers for the case of a nonlinear complex propagation coefficient," *J. Opt. Soc. Am. B*, vol. 2, p. 753, 1985.

[32] A. Mecozzi, J. D. Moores, H. A. Haus, and Y. Lai, "Soliton transmission control," *Opt. Lett.*, vol. 16, no. 23, pp. 1841–1843, 1991.

[33] H. A. Haus and Y. Silberberg, "Laser mode locking with addition of nonlinear index," *IEEE J. Quantum Electron.*, vol. QE-22, pp. 325–331, 1986.

[34] F. X. Kärtner, D. Kopf, and U. Keller, "Solitary-pulse stabilization and shortening in actively mode-locked lasers," *J. Opt. Soc. Am. B*, vol. 12, pp. 486–496, 1995.

[35] D. J. Jones, H. A. Haus, and E. P. Ippen, "Subpicosecond solitons in an actively mode-locked fiber laser," *Opt. Lett.*, vol. 21, p. 1818, 1996.

[36] M. E. Grein, E. P. Ippen, and H. A. Haus, "The quantum limit of timing jitter in actively modelocked soliton lasers," *to be submitted to IEEE J. Quant. Electron.*, XXXX.

[37] M. E. Grein, H. A. Haus, Y. Chen, and E. P. Ippen, "The quantum limit of timing jitter in actively modelocked lasers," in *Conference on Lasers and Electro-Optics*, OSA Technical Digest Series, (Washington, D.C.), pp. 243–244, Optical Society of America, 2001.

[38] D. R. Hjelme and A. R. Mickelson, "Theory of timing jitter in actively mode-locked lasers," *IEEE J. Quantum Electron.*, vol. 28, pp. 1594–1605, 1992.

[39] H. A. Haus and P. T. Ho, "Effect of noise on active modelocking of a diode laser," *IEEE J. Quantum Electron.*, vol. QE-15, pp. 1258–1265, 1979.

[40] P. T. Ho, "Phase and amplitude fluctuations in a mode-locked laser," *IEEE J. Quantum Electron.*, vol. QE-21, pp. 1806–1813, 1985.

[41] I. Kim and K. Y. Lau, "Frequency and timing stability of mode-locked semiconductor lasers-passive and active mode locking up to millimeter wave frequencies," *IEEE J. Quantum Electron.*, vol. 29, pp. 1081–1090, 1993.

[42] D. Eliyahu, R. A. Salvatore, and A. Yariv, "Noise characterization of a pulse train generated by actively mode-locked lasers," *J. Opt. Soc. Am. B*, vol. 13, pp. 1619–26, 1996.

[43] H. A. Haus and A. Mecozzi, "Noise of mode-locked lasers," *IEEE J. Quantum Electron.*, vol. 29, no. 3, pp. 983–996, 1993.

[44] M. Nakazawa, E. Yoshida, and Y. Kimura, "Ultrastable harmonically and regeneratively modelocked polarization-maintaining erbium fibre ring laser," *Electonics Letters*, vol. 30, pp. 1603–1605, 1994.

[45] T. F. Carruthers and I. N. Duling, III, "10-GHz, 1.3-ps erbium fiber laser employing soliton pulse shortening," *Opt. Lett.*, vol. 21, pp. 1927–29, 1996.

[46] M. E. Grein, L. A. Jiang, Y. Chen, H. A. Haus, and E. P. Ippen, "Retiming dynamics in an actively modelocked fiber ring laser," *Opt. Lett.*, vol. 24, pp. 1687–1689, 1999.

[47] C. R. Doerr, H. A. Haus, E. P. Ippen, M. Shirasaki, and K. Tamura, "Additive-pulse limiting," *Opt. Lett.*, vol. 19, pp. 31–33, 1994.

[48] M. Nakazawa, K. Tamura, and E. Yoshida, "Supermode noise suppression in a harmonically modelocked fibre laser by self phase modulation and spectral filtering," *Electron. Lett.*, vol. 32, p. 461, 1996.

[49] E. R. Thoen, M. E. Grein, E. M. Koontz, E. P. Ippen, L. A. Kolodziejski, and H. A. Haus, "Stabilization of an active harmonically mode-locked fiber laser with two-photon absorption," *Opt. Lett.*, vol. 25, pp. 948–950, 2000.

[50] M. Nakazawa, E. Yoshida, and K. Tamura, "10 GHz, 2ps regeneratively and harmonically FM mode-locked erbium fibre ring laser," *Electonics Letters*, vol. 32, pp. 1285–1287, 1996.

[51] S. Namiki, C. X. Yu, and H. A. Haus, "Observation of nearly quantum-limited timing jitter in an all-fiber ring laser," *J. Opt. Soc. Am. B*, vol. 13, pp. 2817–2823, 1996.

[52] S. Namiki and H. A. Haus, "Noise of the stretched pulse fiber ring laser: Part I–Theory," *IEEE J. Quant. Elec.*, vol. 33, pp. 649–659, 1997.

[53] C. X. Yu, S. Namiki, and H. A. Haus, "Noise of the stretched pulse fiber laser II: Experiment," *IEEE J. Quantum Electron.*, vol. 33, pp. 660–668, 1997.

[54] V. V. Kozlov, "Quantum optics with particles of light," *Optics Express*, vol. 8, pp. 688–693, 2001.

[55] T. R. Clark, T. F. Carruthers, P. J. Matthews, and I. N. Duling, III, "Phase noise measurements of ultrastable 10 GHz harmonically modelocked fibre laser," *Elect. Lett.*, vol. 35, pp. 720–721, 1999.

[56] C. X. Yu, H. A. Haus, M. E. Grein, and E. P. Ippen, "The timing jitter of a regenerative mode-locked fiber ring laser," *Quantum Electronics and Femtosecond Optics*, vol. 102, p. XX, 2000.

[57] W. Ng, R. Stephens, D. Persechini, and K. V. Reddy, "Ultra-low jitter modelocking of er-fibre laser at 10 GHz and its application in photonic sampling for analogue-to-digital conversion," *Electron. Lett.*, vol. 37, pp. 113–115, 2001.

[58] H. A. Haus, *Electromagnetic Noise and Quantum Optical Measurements.* Springer-Verlag, 2000.

[59] M. E. Grein, H. A. Haus, L. A. Jiang, and E. P. Ippen, "Action on pulse position and momentum using dispersion and phase modulation," *Opt. Express*, vol. 8, pp. 664–669, 2001.

[60] H. A. Haus and A. Mecozzi, "Long-term storage of a bit stream of solitons," *Opt. Lett.*, vol. 17, pp. 1500–1502, 1992.

[61] V. E. Zakharov and A. B. Shabat, "Exact theory of two-dimensional self-focusing and one-dimensional self-modulation of waves in nonlinear media," *Zh. Eksp. Teor. Fiz*, vol. 34, pp. 61–68, 1971.

[62] D. Kaup, "Perturbation theory for solitons in optical fibers," *Phys. Rev. A*, vol. 42, no. 9, pp. 5689–5694, 1990.

[63] Y. Lai and H. A. Haus, "Quantum-theory of self-induced transparency solitons-a linearization approach," *Phys. Rev. A*, vol. 42, no. 5, pp. 2925–2934, 1990.

[64] H. A. Haus and Y. Lai, "Quantum theory of soliton squeezing: a linearized approach," *J. Opt. Soc. Amer. B*, vol. 7, p. 386, 1990.

[65] N. J. Smith, N. J. Doran, F. M. Knox, and W. Forysiak, "Energy-scaling characteristics of solitons in strongly dispersion-managed fibers," *Opt. Lett*, vol. 21, pp. 1981–1983, 1996.

[66] J. P. Gordon and H. A. Haus, "Random walk of coherently amplified solitons in optical fiber transmission," *Opt. Lett.*, vol. 11, p. 665, 1986.

[67] H. A. Haus and A. Mecozzi, "Noise of mode-locked lasers," *IEEE J. Quantum Electron.*, vol. 30, no. 8, p. 1966, 1994. Corrections to previous calculations of diffusion constants.

[68] H. A. Haus, K. Tamura, L. E. Nelson, and E. P. Ippen, "Stretched-pulse additive pulse mode-locking in fiber ring lasers: theory and experiment," *IEEE J. Quant. Elec.*, vol. 31, pp. 591–598, 1995.

[69] F. Rana and R. J. Ram, "Noise of actively mode-locked lasers with phase modulation and dispersion," *to be submitted*, 2002.

[70] M. E. Grein, L. A. Jiang, H. A. Haus, and E. P. Ippen, "A study of the dynamics governing timing restoration in the actively modelocked soliton laser," in *Conference on Lasers and Electro-Optics*, OSA Technical Digest, (Washington, D.C.), pp. 36–41, Optical Society of America, 1999.

[71] F. Rana, H. L. T. Lee, M. E. Grein, L. A. Jiang, and R. J. Ram, "Characterization of the noise and correlations in harmonically mode-locked lasers," *submitted to JOSA B*, 2002.

[72] X. Shan, D. Cleland, and A. Ellis, "Stabilising with Er fibre soliton laser with pulse phase locking," *Electron. Lett.*, vol. 28, pp. 182–184, 1992.

[73] L. Goldberg, J. Koplow, D. G. Lancaster, R. F. Curl, and F. K. Tittel, "Mid-infrared difference-frequency generation source pumped by a 1.1-1.5 micron dual-wavelength fiber amplifier for trace-gas detection," *Optics Letters*, vol. 23, p. 1517, 1997.

[74] L. Goldberg, B. Cole, and E. Snitzer, "V-groove side-pumped 1.5 micron fibre amplifier," *Electron. Lett.*, vol. 33, p. 2127, 1997.

[75] D. von der Linde, "Characterization of the noise in continuously operating mode-locked lasers," *Applied Physics B*, vol. 39, pp. 201–217, 1986.

[76] U. Keller, K. D. Li, M. Rodwell, and D. M. Bloom, "Noise characterization of femtosecond fiber raman soliton lasers," *IEEE J. Quant. Electron.*, vol. 25, p. 280, 1989.

[77] L. A. Jiang, M. E. Grein, S. T. Wong, and E. P. Ippen, "Measuring timing jitter using optical cross-correlations," *IEEE J. Quant. Electron.*, p. XXXX, 2002. to be published.

[78] G. Sucha, M. E. Fermann, D. J. Harter, and M. Hofer, "High-accuracy time-domain jitter measurement of ultrafast lasers," in *Ultrafast Electronics and Optoelectronics*, OSA Trends in Optics and Photonics, (Washington, D.C.), pp. 36–41, Optical Society of America, 1999.

[79] G. Sucha, M. E. Fermann, D. J. Harter, and M. Hofer, "A new method for rapid temporal scanning of ultrafast lasers," *IEEE J. on Select. Top. Quantum Electron.*, vol. 2, pp. 605–621, 1996.

[80] D. B. Sullivan, D. W. Allan, D. A. Howe, and F. L. Walls, *Characterization of Clocks and Oscillators: NIST Technical Note 1337*. U.S. GPO, Washington, DC, 1990.

[81] W. P. Robins, *Phase noise in signal sources*. New York: Peter Peregrinus, 1982.

[82] H.-P. Company, *Phase noise characterization of microwave oscillators: Phase detector method*. Palo Alto, CA, 1984. Product Note 11729B-1.

[83] C. M. DePriest, P. J. Delfyett, Jr., J. H. Abeles, and A. Braun, "Ultrahigh stability photonic sampling streams from an actively-modelocked semiconductor diode ring laser," in *Conference on Lasers and Electro-Optics*, OSA Technical Digest Series, (Washington, D.C.), pp. 89–90, Optical Society of America, 2001.

[84] K. Gupta, D. Novak, and H. Liu, "Noise characterization of a regeneratively modelocked fiber ring laser," *IEEE J. Quantum Electron.*, vol. 36, p. 70, 2000.

[85] R. P. Scott, C. Langrock, and B. H. Kolner, "High-dynamic-range laser amplitude and phase noise measurement techniques," *IEEE J. Select. Topics in Quantum Electron.*, vol. 7, pp. 641–655, 2001.

[86] D. Allen, "Standard terminology for fundamental frequency and time metrology," in *Proc. 42nd Ann. Frequency Control Symp.*, (New York), pp. 419–425, IEEE Press, June 1988.

[87] W. F. Walls, "Cross-correlation phase noise measurements," in *Proceedings of the 1992 IEEE Frequency Control Symposium*, (New York, NY, USA), pp. 257–260, 1992.

[88] I. N. Duling, III, R. P. Moeller, and T. R. Clark, "Active filtering of the amplitude noise of a mode-locked fiber laser," in *Conference on Lasers and Electro-Optics*, OSA Technical Digest, (Washington, D.C.), pp. 26–27, Optical Society of America, 2000.

[89] C. W. Gardiner, *Handbook of Stochastic Methods.* Springer Verlag, 1996.

[90] D. A. Leep and D. A. Holm, "Spectral measurement of timing jitter in gain-switched semiconductor lasers," *IEEE J. Quant. Electron.*, vol. 60, pp. 2451–2453, 1989.

[91] A. J. Lowery and I. W. Marshall, "Numerical simulations of 1.5 micron actively mode-locked semiconductor lasers including dispersive elements and chirp," *IEEE J. Quantum Electron.*, vol. 27, pp. 1981–1989, 1991.

[92] J. Wey, J. Goldhar, D. Rush, M. Chbat, G. Carter, and G. Burdge, "Performance characterization of a harmonically mode-locked erbium fiber ring laser," *IEEE Photon. Technol. Lett.*, vol. 7, pp. 152–154, 1995.

[93] G. Harvey and L. Mollenauer, "Harmonically mode-locked fiber ring laser with an internal fabry-perot stabilizer for soliton transmission," *Opt. Lett.*, vol. 18, pp. 107–109, 1993.

[94] N. Onodera, "Supermode beat suppression in harmonically mode-locked erbium-doped fiber lasers with composite cavity structure," *Elec. Lett.*, vol. 33, pp. 962–963, 1997.

[95] O. Pottiez, O. Deparis, R. Kiyan, M. Haelterman, P. Emplit, P. Megret, and M. Blondel, "Supermode noise of harmonically mode-locked erbium fiber lasers with composite cavity," *IEEE J. Quantum Electron.*, vol. 38, pp. 252–259, 2002.

[96] L. S. Brown, *Quantum Field Theory.* Cambridge University Press, 1992.

[97] L. Knoll, W. Vogel, and D. G. Welsch, "Action of passive, lossless optical systems in quantum optics," *Phys. Rev. A*, vol. 36, pp. 3803–3818, 1987.

[98] R. J. Glauber and M. Lewenstein, "Quantum optics of dielectric media," *Phys. Rev. A*, vol. 43, pp. 467–491, 1991.

[99] H. Khosravi and R. Loudon, "Vacuum field fluctuations and spontaneous emission in a dielectric slab," *Proc. R. Soc. London Ser. A*, vol. 436, pp. 373–389, 1992.

[100] P. D. Drummond, "Electromagnetic quantization in dispersive inhomogeneous nonlinear dielectrics," *Phys. Rev. A*, vol. 42, pp. 6845–6857, 1990.

[101] B. Hutter, J. J. Baumberg, and S. M. Barnett, "Canonical quantization of light in a linear dielectric," *Europhys. Lett.*, vol. 16, p. 177, 1991.

[102] P. W. Milonni, "Field quantization and radiative processes in dispersive dielectric media," *J. Mod. Opt.*, vol. 42, p. 1991, 1995.

[103] R. E. Slusher, L. W. Hollberg, B. Yurke, J. C. Mertz, and J. F. Valley, "Observation of squeezed states generated by 4-wave mixing in an optical cavity," *Phys. Rev. Lett.*, vol. 55, pp. 2409–2412, 1985.

[104] M. J. Potasek and B. Yurke, "Dissipative effects on squeezed light generated in systems governed by the nonlinear schrödinger equation," *Phys. Rev. A*, vol. 38, pp. 1335–1348, 1988.

[105] L. Wu, H. J. Kimble, J. L. Hall, and H. Wu, "Generation of squeezed states by parametric down conversion," *Phys. Rev. Lett.*, vol. 57, p. 2520, 1986.

[106] M. Xiao, L. Wu, and H. J. Kimble, "Precision measurement beyond the shot-noise limit," *Phys. Rev. Lett.*, vol. 53, p. 278, 1987.

[107] M. W. Maeda, P. Kumar, and J. H. Shapiro, "Observation of squeezed noise produced by forward four-wave mixing in sodium vapor," *Opt. Lett.*, vol. 12, p. 161, 1987.

[108] R. M. Shelby, M. D. Levenson, S. H. Perlmutter, R. G. DeVoe, and D. F. Walls, "Broad-band parametric deamplification of quantum noise in an optical fiber," *Phys. Rev. B*, vol. 57, p. 691, 1986.

[109] M. Shirasaki and H. A. Haus, "Squeezing of pulses in a nonlinear interferometer," *J. Opt. Soc. Am. B*, vol. 7, p. 30, 1990.

[110] F. Hong-Yi and J. VanderLinde, "Squeezed-state wave functions and their relation to classical phase-space maps," *Phys. Rev. A*, vol. 40, p. 4785, 1989.

[111] D. Rugar and P. Grutter, "Mechanical parametric amplification and thermomechanical noise squeezing," *Phys. Rev. Lett.*, vol. 67, p. 699, 1991.

[112] F. DiFilippo, V. Natarajan, K. R. Boyce, and D. E. Pritchard, "Classical amplitude squeezing for precision measurements," *Phys. Rev. Lett.*, vol. 68, p. 2859, 1992.

[113] H. A. Haus, "Steady-state quantum analysis of linear systems," *Proc. of the IEEE*, vol. 58, pp. 1599–1611, 1970.

[114] H. A. Haus and J. A. Mullen, "Quantum noise in linear amplifiers," *Phys. Rev.*, vol. 128, p. 2407, 1962.

[115] L. A. Jiang, M. E. Grein, B. S. Robinson, E. P. Ippen, and H. A. Haus, "Experimental demonstration of a timing jitter eater," in *Conference on Lasers and Electro-Optics*, OSA Trends in Optics and Photonics, (Washington, D.C.), p. CTuF7, Optical Society of America, 2002.

[116] M. E. Grein, E. R. Thoen, E. M. Koontz, H. A. Haus, L. A. Kolodziejski, and E. P. Ippen, "Stabilization of an active harmonically mode-locked fiber laser using two-photon absorption," in *Conference on Lasers and Electro-Optics*, OSA Technical Digest Series, (Washington, D.C.), pp. 24–25, Optical Society of America, 2000.

[117] J. T. Gopinath, E. R. Thoen, E. M. Koontz, M. E. Grein, L. A. Kolodziejski, and E. P. Ippen, "Recovery dynamics in proton-bombarded semiconductor saturable absorber mirrors," *Appl. Phys. Lett.*, vol. 78, p. 3409, 2001.

[118] T. F. Carruthers, I. N. Duling, III, M. Horowitz, and C. R. Menyuk, "Dispersion management in a harmonically mode-locked fiber soliton laser," *Opt. Lett.*, vol. 25, pp. 153–155, 2000.

[119] A. D. Corno, G. Gabetta, G. C. Reali, V. Kubecek, and J. Marek, "Active-passive mode-locked Nd:YAG laser with passive negative feedback," *Opt. Lett.*, vol. 15, p. 734, 1990.

[120] M. Jiang, G. Sucha, M. E. Fermann, J. Jimenez, D. Harter, M. Dagenais, S. Fax, and Y. Hu, "Nonlinearly limited saturable-absorber modelocking of an erbium fiber laser," *Opt. Lett.*, vol. 24, p. 1074, 1999.

[121] E. R. Thoen, *Development of Ultrashort Pulse Fiber Lasers for Optical Communication Utilizing Semiconductor Devices.* PhD thesis, Massachusetts Institute of Technology, 2000.

[122] E. M. Koontz, *The Development of Components for Ultrafast All-Optical Communication Networks.* PhD thesis, Massachusetts Institute of Technology, 2000.

[123] P. Langlois, M. Joschko, E. R. Thoen, E. M. Koontz, F. X. Kärtner, E. P. Ippen, and L. A. Kolodziejski, "High fluence ultrafast dynamics of semiconductor saturable absorber mirrors," *Appl. Phys. Lett.*, vol. 74, p. 3927, 1999.

[124] S. Gupta, J. F. Whitaker, and G. A. Mourou, "Ultrafast carrier dynamics in III-V semiconductors grown by molecular-beam epitaxy at very low substrate temperatures," *IEEE J. Quantum Electron.*, vol. 28, p. 2464, 1992.

[125] E. L. Delpon, J. L. Oudar, N. Bouché, R. Raj, A. Shen, N. Stelmakh, and J. M. Lourtioz, "Ultrafast excitonic saturable absorption in ion-implanted InGaAs/InAlAs multiple quantum wells," *Appl. Phys. Lett.*, vol. 1998, p. 759, 72.

[126] M. J. Leder, B. Luther-Davies, H. H. Tan, C. Jagadish, M. Haiml, U. Siegner, and U. Keller, "Nonlinear optical absorption and temporal response of arsenic- and oxygen-implanted GaAs," *Appl. Phys. Lett.*, vol. 74, p. 1993, 1999.

[127] U. Siegner, R. Fluck, G. Zhang, and U. Keller, "Ultrafast high-intensity nonlinear absorption dynamics in low-temperature grown gallium arsenide," *Appl. Phys. Lett.*, vol. 69, p. 2566, 1996.

[128] M. D. Dvorak and B. L. Justus, "Z-scan studies of nonlinear absorption and refraction in bulk, undoped InP," *Opt. Commun.*, vol. 114, p. 147, 1995.

[129] M. H. Chou, J. Hauden, M. A. Arbore, and M. M. Fejer, "1.5 micron-band wavelength conversion based on difference-frequency generation in LiNbO3 waveguides with integrated coupling structures," *Opt. Lett.*, vol. 23, pp. 1004–1006, 1998.